



UNIVERSITÄT ZU LÜBECK



MASSACHUSETTS
GENERAL HOSPITAL

Fractional Ablation of Skin using a Carbon Dioxide Laser, a Carbon Monoxide Laser, and a Thulium Fiber Laser: A Comparison Study

Man Linh Ha

Dissertation

Institut für Biomedizinische Optik
der Universität zu Lübeck
Direktor: Prof. Dr. rer. nat. Alfred Vogel

in Zusammenarbeit mit

Cutaneous Biology Research Center, Department of Dermatology
Massachusetts General Hospital, Harvard Medical School, Boston, MA, USA
Direktor: David E. Fisher, M.D., Ph.D.

From the Institute of Biomedical Optics
of the University of Lübeck
Director: Prof. Dr. rer. nat. Alfred Vogel
in collaboration with
Cutaneous Biology Research Center, Department of Dermatology
Massachusetts General Hospital, Harvard Medical School, Boston, MA, USA
Director: David E. Fisher, M.D., Ph.D.

Fractional Ablation of Skin using a Carbon Dioxide Laser, a Carbon Monoxide Laser, and a Thulium Fiber Laser: A Comparison Study

Dissertation

for fulfillment of requirements
for the doctoral degree

of the University of Lübeck
- from the Sektion Medizin -
submitted by

Man Linh Ha
from Braunschweig, Germany

Lübeck 2019

1. Berichterstatter: Prof. Dr. phil. nat. Dr. med. habil. Reginald Birngruber

2. Berichterstatter: Priv.-Doz. Dr. med. Tobias Fischer

Tag der mündlichen Prüfung: 06.03.2020

Zum Druck genehmigt. Lübeck, den 06.03.2020

- Promotionskommission der Sektion Medizin -

Zusammenfassung

Hintergrund: Konventionelle Laserverfahren zur Oberflächenregenerierung der Altershaut (Laser Skin Rejuvenation) durch großflächige Abtragung der gesamten Epidermis und der Anteile der papillären Dermis sind effektiv, aber durch Nebenwirkungen (Infektion, Narbenbildung, lange Heilungsdauer) gekennzeichnet. Die fraktionierte Photothermolyse (Manstein und Laubach 2007) beschreibt das Konzept der Abtragung von Epidermis und Dermis in mikroskopisch kleinen Ablationszonen mittels fokussierter Laserstrahlung. Durch die hohe Absorption von Infrarotstrahlung im Gewebewasser, kürzere Pulsdauer als die thermische Relaxationszeit, kleine Fokusgröße und hohe Bestrahlung resultiert ein Temperaturanstieg in der Haut, der zu Ablation und Koagulation führt. Aufgrund dieser selektiven Photothermolyse bleibt die benachbarte Haut thermisch unbeschädigt (Anderson und Parrish 1983). Dadurch wird bei gleichzeitiger Reduktion der Nebenwirkungen ein starker Reiz zur Wundheilung induziert. Typischerweise zeigt sich in der Histologie ein bis in die Dermis reichender Ablationskanal mit angrenzender Koagulationszone. Diese Koagulationszone dient auch der Hautstraffung. Klinisch konnte der erfolgreiche Einsatz von fraktionierten Laserverfahren z.B. zur Behandlung von tiefen Falten, Aknenarben, aktinischen Keratosen und Pigmentstörungen gezeigt werden.

Der Kohlenstoffdioxidlaser (CO_2 Laser) mit einer Wellenlänge von 10600 nm ist der Goldstandard zur Behandlung der Altershaut. Durch die hohe Absorption in der Haut führt die Applikation von fokussierter CO_2 -Laserstrahlung zu einer sofortigen Verdampfung mit minimaler, thermischer Randzone. Ablationstiefe, Koagulationszone und das Verhältnis zwischen Ablation und Koagulation beeinflusst die Wundheilung und das klinische Ergebnis. Diese Laser-Haut-Effekte sind generell beeinflussbar durch Wellenlänge, Pulszahl, Pulsdauer, Pulsenergie, zeitliches und räumliches Pulsprofil. Eine Änderung der Wellenlänge kann signifikant Parameter wie optische Penetrationstiefe und Fokusgröße beeinflussen.

Als der erste CO_2 Laser erfunden wurde (Patel und Kerl 1964), gab es zudem Berichte über Laseraktivität von Kohlenstoffmonoxidmolekülen im Bereich von 5000-5400 nm Wellenlänge. 1983 wurde bereits ein Kohlenstoffmonoxidlaser (CO Laser) zum Schneiden von Gewebe getestet. Im Gegensatz zum CO_2 Laser gab es jedoch aufgrund der Instabilität, geringen Leistung und limitierten Laufzeit nur wenige Forschungsarbeiten zum CO Laser.

In dieser Vergleichsstudie wurde ein neuartiger CO Laser mit einer Wellenlänge von 5500 nm und ein Thuliumlaser (Tm Laser) mit einer Wellenlänge von 1940 nm mit dem etablierten CO_2 Laser hinsichtlich der Ablations- und Koagulationseigenschaften verglichen. Der wellenlängenabhängige Absorptionskoeffizient ist umgekehrt proportional zur optischen Penetrationstiefe. Der CO Laser besitzt in der Haut eine dreifach geringere Absorption im Vergleich zum CO_2 Laser, so dass beim CO Laser daher eine größere Koagulationszone angenommen wird. Da die Strahltaile proportional zur Wellenlänge ansteigt, ist ein Vorteil einer kürzeren Wellenlänge die bessere Fokussierbarkeit. Die Generierung von kleineren Fokusgrößen führt zu einer höheren Bestrahlungsstärke. Ebenfalls wird auch eine schnellere Heilungsdauer durch kleinere

Wunden angenommen. Darüberhinaus ermöglicht der CO Laser aufgrund seiner kürzeren Wellenlänge auch eine höhere Rayleighlänge, die Defokussierungsprobleme bei inhomogenen Hautoberfläche reduzieren kann. Es besteht zudem die Annahme, dass die Einkopplung von CO Laserstrahlung in flexible Lichtleiter technisch einfacher realisierbar ist. Der CO₂ Laser erfordert dagegen die Verwendung von rigiden Spiegelarmsystemen. Im Gegensatz zum CO₂ Laser handelt es sich bei dem Tm Laser um einen Faserlaser, der eine neunfach geringere Absorption besitzt und bisher als nicht ablativer Laser zur Behandlung der benignen Prostatahyperplasie im Einsatz ist.

Es wurde von einigen Autoren postuliert, dass eine tiefere, dermale Ablation mit größerer Koagulationszone zu besseren klinischen Ergebnissen im Rahmen der fraktionierten Lasertherapie durch dermale Umbauprozesse beitragen kann. Ziel dieser experimentellen Studie ist zunächst der Vergleich der Ablationstiefen von CO₂ Laser, CO Laser und Tm Laser mit der Annahme, dass der CO Laser und der Tm Laser eine Ablation der Haut mit größeren Koagulationszonen als der CO₂ Laser erzeugen können und dass der CO Laser annähernd vergleichbare Ablationstiefen zum CO₂ Laser erreichen kann.

Material und Methoden: Mit Genehmigung vom Massachusetts General Hospital Institutional Review Board in Boston (USA) wurde überschüssige Haut im Rahmen von Abdominoplastiken gesammelt. Diese entnommene Haut enthielt zu keiner Zeit personenbezogene Daten und wird regulär postoperativ entsorgt. Diese Hautproben wurden dem Cutaneous Biology Research Center (CBRC) für die Laserexperimente zur Verfügung gestellt und anschließend richtliniengetreu entsorgt.

Die Laser-Haut-Experimente wurden mit vier verschiedenen Lasersystemen durchgeführt. Ein klinisches 94 W CO₂ Lasersystem und ein modifiziertes, Pulslängen-moduliertes CO₂ Lasersystem mit einer Wellenlänge von 10600 nm wurden eingesetzt. Das klinische CO₂ Lasersystem zeigte eine spezifische Pulsstruktur mit Mikrooszillationen (2 MHz Repetitionsfrequenz) und einer internen Pulslängenvariation. Für den Vergleich der Lasersysteme erfolgte daher eine Modifikation des CO₂ Lasersystems, die eine externe Pulslängenvariation ermöglichte. Die CO₂ Lasersysteme wurden mit einem 100 W CO Laser mit einer Wellenlänge von 5500 nm und einem 120 W Tm Laser mit einer Wellenlänge von 1940 nm verglichen. Bei unterschiedlicher, wellenlängenabhängiger Absorption wurden ähnliche Laserparameter wie Pulsdauer von 2 ms, Fokusgröße von 108-120 µm und Pulsenergie von etwa 10-200 mJ adjustiert. In einem zusätzlichen Experiment wurde der CO Laser auf eine Fokusgröße von 54 µm reduziert. Während der CO Laser eine ähnliche Pulsstruktur mit Mikrooszillationen (6.5 MHz Repetitionsfrequenz) zeigte, wies der Tm Laser einen Rechteckpuls ohne Mikrostruktur auf. Basierend auf der hohen Repetitionsfrequenz, wurde eine Vergleichbarkeit der Makropulse mit dem Tm Laserpuls angenommen.

Die Knife-Edge-Methode wurde zur Vermessung der Strahldurchmesser angewandt. Die Fokusebene wurde jeweils auf die Ebene der Hautoberfläche eingestellt. Die Laser-Haut-Effekte wurden histologisch in Form von Gefrierschnitten mit Vitalitätsnachweis durch Nitro-

blautetrazoliumchlorid-Färbung analysiert. Diese Färbung erlaubte die Differenzierung zwischen thermisch geschädigtes Gewebe und normales Gewebe. Ablationstiefe und Koagulationszonen am den Rändern und am Boden des Ablationskanals wurden bestimmt. Die Ablationskurven wurden mit Hilfe des Hibst-Modells, Blow-off-Modells und Steady-state-Modells gefittet. Das Blow-off-Modell beschreibt den Ablationsprozess für einen Puls, der viel kürzer als die thermische Relaxationszeit im Gewebe ist. Dem gegenübergestellt beschreibt das Steady-state-Modell den Ablationsprozess für einen Puls, der viel länger als die thermische Relaxationszeit ist. Das Hibst-Modell stellt eine Kombination aus dem Blow-off-Modell und dem Steady-state-Modell dar und wurde als Annäherung an diese Modelle im Grenzfall benutzt. Ergänzend zu der histologischen Auswertung wurde die Ablation in einem vereinfachten 3-Schichten-Hautmodell mittels Finite-Elemente-Methode (FEM) numerisch simuliert. Die Methode der finiten Elemente beruht auf der Zerlegung der erzeugten Hautschichten in ein Gitter mit endlichen Elementen und der numerischen Lösung der partiellen Differentialgleichungen. Mit Hilfe von Wärmetransport und Phasenübergang wurde die Ablation simuliert. Dieses dreidimensionale Modell besteht aus zwei Phasen, dem Gewebe vor Ablation in Phase 1 und dem entfernten Gewebe nach Ablation in Phase 2. Phase 1 existiert für Temperaturen unter 300°C und Phase 2 existiert für Temperaturen über 300°C . Zusammen mit der Phase ändern sich Materialeigenschaften des Hautmodells. Hierbei wurde mathematisch in Phase 2 die Absorption auf 0 cm^{-1} und die spezifische Wärmekapazität auf $10^9\text{ J}/(\text{kgK})$ gesetzt, um den Materialabtrag und den Wärmeabtransport nach erfolgter Ablation im Modell zu simulieren. Die Ablation wurde damit absichtlich als einen rein thermisch gesteuerten Prozess betrachtet.

Ergebnisse: Aufgrund der niedrigsten Ablationsschwelle zeigten die CO_2 Lasersysteme die höchste Abtragstiefe bis zu 3 mm mit den geringsten Koagulationszonen bis zu $150\text{ }\mu\text{m}$. Im Vergleich zeigte der Tm Laser mit der höchsten Ablationsschwelle nur oberflächliche Abtragung der papillären Dermis bis zu $380\text{ }\mu\text{m}$ mit den größten Koagulationszonen bis zu $300\text{ }\mu\text{m}$. Bei Betrachtung der auf die Ablationsschwelle normierten Bestrahlung, konnte ein bis zu zweifach höherer Abtrag durch den CO Laser im Vergleich zum CO_2 Laser bei 10- und 40-facher Bestrahlung festgestellt werden. Die Koagulationszone war beim CO Laser etwa doppelt so groß. Mit dem Hibst-Modell konnte mit Hilfe des γ -Fitparameters keine zuverlässige Aussage getroffen werden, ob ein Ablationsprozess dem Blow-off-Modell oder dem Steady-state-Modell folgt. Die Ablationskurve vom Tm Laser konnte mittels Blow-off-Modell gefittet werden, aber die Ablationskurven von CO_2 Laser und CO Laser konnten nicht mittels Steady-state-Modell beschrieben werden.

In der numerischen Simulation der Ablation basierend auf Wärmetransport und Phasenübergang konnten die histologischen Ergebnisse nicht reproduziert werden. Mit Annahme einer Ablation bei Temperaturen über 300°C waren die geschätzten Ablationstiefen um einen Faktor 6-13 kleiner. Bei der Berechnung der Koagulationszonen für Temperaturen zwischen 65°C – 300°C wurde der Arrhenius-Effekt vernachlässigt. Die geschätzten Koagulationszonen waren um einen Faktor 2-3 kleiner als die histologischen Befunde.

Schlussfolgerung: In der aktuellen Einstellung kann der Tm Laser keine ausreichend tiefe Ablation erreichen. Eine Anpassung der Laserparameter wie Verlängerung der Pulsdauer, Erhöhung der Leistung oder Modifikation der zeitlichen Pulsstruktur sind erforderlich, um höhere Abtragstiefen ohne signifikante Erweiterung der Koagulationszonen zu realisieren. Der CO Laser hat in dieser vorläufigen Studie gezeigt, dass dem CO₂ Laser ähnliche Ablationstiefen mit etwas größeren Koagulationszonen erzielt werden können. Ob und in welchem Ausmaß erweiterte Koagulationszonen zu besseren klinischen Ergebnissen im Rahmen der fraktionierten Lasertherapie führen, müssen durch weitere klinische Studien mit Beobachtung der Wundheilung überprüft werden. Ferner besteht die Annahme, dass durch Modulation der Pulsstruktur die Abtragstiefe beeinflusst werden kann. In weiteren experimentellen Studien könnten die Abtragstiefe in Abhängigkeit der Oszillationsfrequenz und weiteren Änderungen der Pulsstruktur analysiert werden. Durch die vereinfachten Modellannahmen konnte in der numerischen Simulation keine realistischen Aussagen über Ablationstiefe und Koagulationszonen erzielt werden. Dies zeigt, dass die Ablation ein komplexes Geschehen mit vielen Interaktionen darstellt. Das Modell erfordert folglich die Berücksichtigung weiterer Mechanismen wie z.B. Arrhenius-Effekt, Materialauswurf, Gasexpansion, Gewebedisruption, Gewebeschrumpfung, Abschirmeffekte und weitere nicht lineare Effekte, um ein realistisches Abbild der Ablation entwickeln zu können.

Abstract

Background: The optimal laser treatment could be offered if the amount of tissue removal and heat delivery is tailored to the patient's skin type and indication. However, the ratio of ablation to thermal damage is principally dictated by the absorption coefficient at a specific wavelength, the exposure time, and the spot size. A recent generation of 5500 nm carbon monoxide laser could be a novel laser tool for applications in medicine and surgery. Based on the water absorption in tissue, the optical penetration depth at this wavelength is about 50 μm , while that of the 10600 nm carbon dioxide laser as the gold standard is limited to 15 μm . We anticipate additional coagulation for the carbon monoxide lasers that could lead to enhanced skin tightening in the fractional laser therapy of aging skin when compared to highly ablative carbon dioxide lasers. In contrast, the 1940 nm thulium fiber laser is known as a non-ablative laser due to the high optical penetration depth of about 125 μm . Thus, it is of interest to evaluate the feasibility of novel laser sources such as the carbon monoxide laser for ablation of skin against the backdrop of extending the current laser treatment options.

Materials and Methods: We used a carbon monoxide laser, a clinical and a modified, pulse-width-modulated carbon dioxide laser, and a thulium fiber laser to irradiate ex vivo human skin obtained from abdominoplasty. We adjusted similar exposure parameters, such as spot size (108-120 μm), pulse duration (2 ms), and pulse energy (about 10-200 mJ) using different lasers. The etch depth and the thermal damage zones were quantified by histology. The ablation-to-coagulation-ratio was determined. We generated a numerical simulation of the laser-tissue ablation based on heat transfer and phase change.

Results: The carbon dioxide lasers exhibit the highest etch depths with the least thermal damage zones in comparison to the carbon monoxide laser and the thulium fiber laser when applying the same pulse energies at 2 ms pulse duration. However, at radiant exposures 40-times higher than the ablation threshold, the etch depth produced by the carbon monoxide laser is 47% higher as compared with the carbon dioxide laser. At 10-times the ablation threshold, the etch depth by the carbon monoxide laser is 2-times higher. As the ablation craters exhibit about 2-times larger coagulation zones, the carbon monoxide laser demonstrates an ablation-to-coagulation-ratio that is half the ratio of the carbon dioxide laser. In contrast, the thulium fiber laser shows superficial tissue removal with pronounced thermal injury and exhibits the smallest ablation-to-coagulation-ratio for all pulse energies. The numerical simulation underestimates the ablation depth and the coagulation zones.

Conclusion: We conclude that the thulium fiber laser used in this configuration is not suitable for deep ablation. The carbon monoxide laser has the potential of generating high etch depths comparable to the carbon dioxide laser with extended thermal damage zones. We anticipate that alterations in temporal pulse profile and smaller spot sizes would additionally influence the ablation outcome that need to be verified in further experiments. The numerical simulation requires the consideration of other mechanisms besides heat transfer and phase change to obtain reliable predictions of the ablation depth and the thermal damage.

Table of Contents

1	Introduction	5
1.1	Motivation	5
1.2	Research Objectives	6
2	Background	8
2.1	Properties of Skin	8
2.1.1	Skin Composition	8
2.1.2	Aging of Human Skin	9
2.2	Basic Principles of Lasers	10
2.2.1	Laser Light	10
2.2.2	Laser Parameters	11
2.3	Interactions of Laser Light with Tissue	13
2.3.1	Optical Properties of Skin	13
2.3.2	Thermal Properties of Skin	16
2.3.3	Thermal Effects in Skin	17
2.3.4	Threshold, Enthalpy, and Efficiency of Ablation	19
2.3.5	Ablation Models	20
2.4	Applications in Dermatology	22
2.4.1	Fractional Laser Resurfacing	22
2.4.2	The Gold Standard CO2 Laser	22
2.4.3	The Potential of CO Laser	23
2.4.4	The Potential of Tm:Fiber Laser	23
3	Materials and Methods	24
3.1	Laser Systems	24
3.1.1	Clinical 10600 nm CO2 Laser System	24
3.1.2	Modified 10600 nm CO2 Laser System	25
3.1.3	5500 nm CO Laser	26
3.1.4	1940 nm Tm:Fiber Laser	27
3.2	Beam Parameter Measurements	28
3.2.1	Temporal Pulse Profile	28
3.2.2	Spatial Beam Profile	30
3.3	Experimental Setup	33
3.4	Laser-Tissue Exposures	34
3.5	Histological Evaluation of Etch Depth and Thermal Damage	36
3.6	Numerical Simulation of Heat Transfer and Tissue Ablation in Skin	38
3.6.1	Skin Geometry	39
3.6.2	Heat Source	39
3.6.3	Laser Pulse	40
3.6.4	Bioheat Transfer with Phase Change	40

3.6.5	Simulation of Tissue Ablation	41
4	Results	43
4.1	Etch Depth	43
4.2	Basic Ablation Models	46
4.3	Thermal Damage Zones	48
4.4	Ablation-to-Coagulation-Ratio (ACR)	49
4.5	Small Spot CO Laser Ablation	50
4.6	Numerical Study of Heat Transfer and Phase Change in Skin	51
4.6.1	Laser-Tissue Ablation Model	51
4.6.2	Temperature and Phase Change	51
4.6.3	Simulation of Ablation and Coagulation Zones	53
5	Discussion	55
5.1	Laser-Tissue Ablation Experiments	55
5.1.1	Exposure Parameters	55
5.1.2	Ablation Depth	57
5.1.3	Residual Thermal Damage	58
5.1.4	Basic Ablation Models	59
5.1.5	ACR	59
5.1.6	The Effect of Spot Size	60
5.2	Numerical Simulation of Laser-Tissue Ablation	60
5.2.1	Two-Phase Model	61
5.2.2	Ablation Depth and Thermal Damage	61
6	Conclusion	63
6.1	Tm:Fiber Laser Ablation	63
6.2	CO Laser Ablation	63
6.3	Simulation Study	64
7	Appendix	65
8	References	77
9	Acknowledgements	82
10	Curriculum Vitae	83
11	Published Work	85

List of Abbreviations

Abbreviation	Meaning
ACR	ablation-to-coagulation-ratio
CO ₂	carbon dioxide
CO	carbon monoxide
cw	continuous wave
FWHM	full width at half maximum
LASER	light amplification by the stimulated emission of radiation
MMP	matrix metalloproteinase
MASER	microwave amplification for stimulated emission of radiation
NBTC	nitro blue tetrazolium chloride
OCT	optimal cutting temperature compound
PBS	phosphate-buffered saline
RF	radio frequency
ROS	reactive oxygen species
Tm	thulium
UV	ultraviolet radiation

List of Symbols

Symbol	Units	Description
η_{abl}	kg/J	ablation efficiency
h_{abl}	J/kg	ablation enthalpy of tissue
H_{th}	J/cm ²	ablation threshold
μ_a	cm ⁻¹	absorption coefficient
z	mm	beam propagation distance
M^2	no unit	beam quality factor
w_0	μm	beam waist at focal plane
w	μm	beam width
\tilde{H}_{th}	J/cm ²	blow-off or steady-state fitted ablation threshold
$\tilde{\mu}_a$	cm ⁻¹	blow-off or steady-state fitted absorption coefficient
ϱ	kg/m ³	density
$\delta_{blow-off}$	μm	etch depth according to blow-off model
δ_{hibst}	μm	etch depth according to Hibst modification
$\delta_{steady-state}$	μm	etch depth according to steady-state model
f	mm	focal length

z_0	mm	focal plane
\tilde{H}_{th}	J/cm ²	Hibst fitted ablation threshold
$\tilde{\mu}_a$	cm ⁻¹	Hibst fitted absorption coefficient
γ	no unit	indicator for plume absorption
I_0	W/cm ²	irradiance
L_v	J/kg	vaporization enthalpy of water
\bar{x}_e	μm	mean lateral thermal damage zone at the edges
\bar{x}_b	μm	mean residual thermal damage zone at the bottom
δ	μm	optical penetration depth
P	W	power
τ_p	ms	pulse duration
E_p	mJ	pulse energy
H_0	J/cm ²	radiant exposure
z_R	μm	Rayleigh range
n	no unit	refractive index
f_{rep}	Hz	repetition rate
μ_s	cm ⁻¹	scattering coefficient
c_v	J/(kgK)	specific heat capacity
c	m/s	speed of sound
τ_s	ns	stress confinement time
T	°C	temperature
ΔT	no unit	temperature rise
k	W/(mK)	thermal conductivity
τ_{tc}	ms	thermal confinement time
κ	mm ² /s	thermal diffusivity
μ_t	cm ⁻¹	total attenuation coefficient
W_{abl}	J/cm ³	volumetric energy density, total heat of ablation
λ	nm	wavelength

1 Introduction

1.1 Motivation

The production of small and confined tissue effects using focused laser beams, known as "fractional photothermolysis", leads to a dermal tissue remodeling response that enhances the appearance of the skin [32]. The fractional ablation of skin involves microscopic zones of locally removed epidermis and dermis. Ablative fractional lasers have been clinically demonstrated to successfully treat aesthetic and dermatological indications, such as deep wrinkles, acne scars, actinic keratosis, and pigmentation disorders [38]. Another application of ablative lasers is the "fractional laser-assisted drug delivery" that has been established to enhance topical treatments. The skin barrier is temporarily disrupted by channels of ablated tissue, which can serve as a pathway for drug deposition in deeper skin areas [9].

The carbon dioxide (CO_2) laser has become one of the most widely used lasers for fractional laser skin rejuvenation in the field of dermatology [34]. The application of focused CO_2 laser beams causes immediate evaporation with minimal thermal damage due to the strong absorption in tissue water. Etch depth, width of ablation, degree of thermal injury, and ratio of ablation zone to thermal damage zone principally define the remodeling effects and the recovery time [42]. For "fractional laser-assisted drug delivery", the geometry of the ablation crater can regulate the drug uptake and the coagulation zone can serve as a drug reservoir [9, 50]. Thus, laser and laser-assisted applications are highly customizable by the laser-tissue effects that are influenced by wavelength, pulse number, pulse duration, pulse energy, temporal and spatial pulse profile. A change of wavelength can significantly change parameters, such as optical penetration depth and focused spot size.

In 1964, at around the same time as inventing the first 10600 nm CO_2 laser, Patel and Kerl reported on laser action of carbon monoxide (CO) molecules in the 5000-5400 nm spectral range [36]. Aleinikov et al. already conducted potential medical applications using 15 W CO laser beams for tissue cutting in 1983. They observed that CO laser radiation has higher efficiency in terms of electrical energy conversion to light, superior cutting and coagulating properties than the CO_2 laser radiation due to the higher optical penetration of CO laser light [2]. The optical penetration depth of 5500 nm CO laser light is about 50 μm in water, while that of CO_2 laser light is limited to about 15 μm in water [24]. We anticipated that the higher optical penetration depth at the wavelength of 5500 nm could provide a beneficial ablation to coagulation profile compared to the traditional laser sources. As it is believed that controlled heating and ablation in the deep dermis can contribute to enhanced tissue tightening in the fractional laser treatment of deep wrinkles [35]. Referring to "fractional laser-assisted drug delivery", a thicker zone of coagulation could lead to a longer depot effect of the topical treatment due to slower drug diffusion [9].

Compared to the reports on CO_2 lasers, there has been less research work on the CO laser for decades. In the past, the CO laser emission was low in output power or required cryogenic

cooling for a high output power operation. Also, the operating time of the active molecules in early CO lasers was limited to just hours. Altogether, these drawbacks made the CO laser technology impractical and not reliable enough for clinical use. But recently, a new generation of fully sealed 100 W CO laser generating 95% of the laser emission at 5500 ± 275 nm wavelength has become available. The lifetime of the novel CO lasers was enhanced and the operating characteristics have become more similar to the well-known CO₂ laser technology [22].

Advantages of a shorter wavelength could be seen in the tighter focusing, as the beam waist is proportional to the wavelength. This would enable the generation of smaller spot sizes than currently provided by the CO₂ lasers. A reduction of the spot size will lead to an increase in irradiance. Also, smaller ablation diameters in skin could potentially contribute to faster wound healing. For the same spot size, the CO laser beam could provide a higher Rayleigh range due to the shorter wavelength. The longer depth of focus might reduce defocusing problems in the irradiation of the physiologically inhomogeneous skin surface. Furthermore, the rigidity of the articulated mirror arm that has to be integrated into medical CO₂ laser systems is a substantial disadvantage for surgical use. Flexible optical waveguides would facilitate the convenient handling of a medical laser and would allow the delivery of laser light into cavities. In 1986, Abakumov et al. have reported the first results on the use of an optical fiber for the delivery of the CO laser radiation to the area of operation [1]. In brief, smaller spot sizes, longer depth of focus, and more convenient implementation of fiber delivery are anticipated in contrast to CO₂ lasers.

Non-ablative fractional lasers that leave the epidermis intact while promoting the dermal collagen formation evolved to reduce potential side effects. In 2005, when non-ablative fractional lasers became available, 1927 nm thulium fiber (Tm:fiber) laser was qualified for the treatment of actinic keratosis and mild to moderate photodamage. The Tm:fiber laser is primarily intended for superficial epidermal indications, as the optical penetration depth in water is about 125 μ m. Fairly moderate results have been typically observed with the use of non-ablative fractional lasers [38]. Therefore, a non-ablative fractional Tm:fiber laser is less efficient when compared with the ablative lasers. Up to now, the Tm:fiber laser has not been used for ablative fractional procedures. Since the Tm:fiber laser has demonstrated its ability to produce sufficient coagulation during the resection, it was introduced for the treatment of benign prostatic hyperplasia [33].

1.2 Research Objectives

In this thesis, we aimed to demonstrate the ablation and coagulation capabilities of a 5500 nm CO laser and a 1940 nm Tm:fiber laser in comparison with the routine use of short pulsed CO₂ lasers. For this study, there were two working hypotheses: 1. The CO laser and the Tm:fiber laser can generate fractional lesions with larger zones of thermal damage than the CO₂ laser and 2. the CO laser can achieve deep ablation channels that are comparable

to the CO₂ laser. In pursuit of this goal, we aimed to operate these three lasers at similar exposure parameters and to compare the laser-tissue effects in ex vivo human skin with regard to the different wavelength-dependent water absorption. The wound healing processes and the tissue tightening effects will be investigated in an intended in vivo study and were not part of this ex vivo study. The experiments in this thesis were performed with clinical and experimental lasers. The experimental lasers involved a 1940 nm Tm:fiber laser and a 5500 nm CO laser. The clinical laser used as the gold standard system was a 10600 nm CO₂ laser. We also used this CO₂ laser in a modified version that allowed external pulse modulation. In contrast to the early studies about the effects of CO laser beams on biological tissues by Aleinikov et al. in 1983 [2], we irradiated ex vivo human skin using single and tightly focused laser pulses in the range of milliseconds. Laser-induced thermal damage and ablation depth were quantified by histology sections. In addition, we aimed to develop a 3D simulation of the laser-tissue ablation using finite element method to predict ablation depth and thermal damage zones.

2 Background

This chapter covers the basic knowledge of human skin structure and laser beam properties. The laser-tissue interaction is described as how the propagation and deposition of laser light is affected by the skin components and, vice versa, how the skin tissue is altered by the heat effect of laser light. This chapter concludes with a dermatological application of lasers, the laser skin resurfacing that makes use of laser-induced thermal effects to treat photodamaged skin.

2.1 Properties of Skin

2.1.1 Skin Composition

Skin is a tissue composition of heterogeneous cell types, extracellular matrix, and appendages. Three layers of the skin can be distinguished: epidermis, dermis, and subcutis (**Figure 1**) [20]. Each skin layer exhibits its characteristic optical, thermal, and mechanical properties, which are relevant for the interaction with laser light [55].

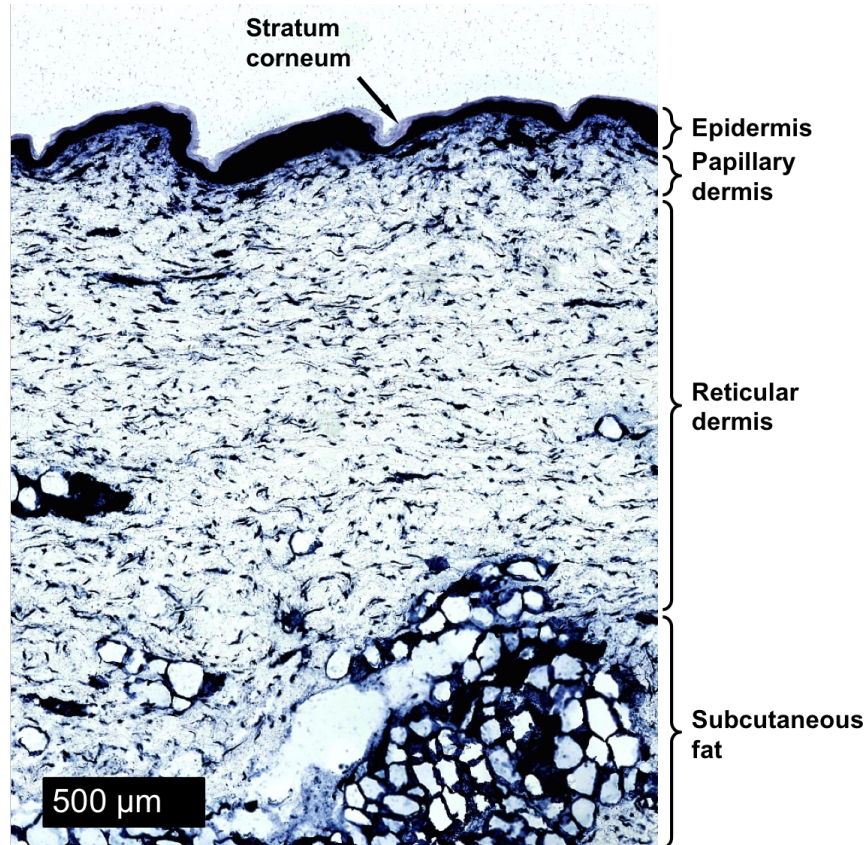


Figure 1. Ex vivo human skin stained with nitro blue tetrazolium chloride (NBTC). Skin consists of epidermis, dermis, and subcutis. The epidermal layer is formed by stratum corneum, stratum granulosum, stratum spinosum, and stratum basale. The dermal layer consists of a superficial papillary dermis and a lower reticular dermis. Subcutaneous fat is located just beneath the dermis.

The epidermis is a stratified squamous epithelium that contains 90-95% keratinocytes, melanocytes, Langerhans cells, and Merkel cells. Starting from the surface, the epidermal layer is formed by stratum corneum, stratum granulosum, stratum spinosum, and stratum basale [6]. The water content is about 20% in the upper epidermis and increases linearly with depth [5]. Keratinocytes are formed in the stratum basale and require about 28 days to migrate upward to the stratum corneum for differentiation (keratinization). The proliferation rate of keratinocytes is dramatically increased by injury or inflammation. The stratum corneum serves as a physiological barrier to protect the skin from the environment. Melanocytes produce the pigment melanin, which absorbs ultraviolet radiation (UV) for skin protection. Langerhans cells can process antigenic materials for antigen presentation to lymphocytes. The boundary between epidermis and dermis is known as the basement membrane [6, 20]. The major components of the basement membrane are non-fibrillar type IV collagen, laminin, entactin/nidogen, and sulfated proteoglycans [62].

The dermis is the connective tissue component that provides elasticity and tensile strength to the skin. The dermal connective tissue matrix is mainly composed of collagen, elastic fibers, and ground substance. The water content is approximately 60-70%. The non-fibrous ground substance is contained of glycoproteins, proteoglycans, and glycosaminoglycans [6, 20]. The main cell type of the dermal layer is the fibroblast that synthesizes matrix proteins, such as collagen and elastin. The collagen accounts for 75% of the skin's dry weight. 80-90% of the dermal collagen is type I collagen and 8-12% is type III collagen. Two distinct layers within the dermis can be identified: superficial papillary dermis and lower reticular dermis. Close to the epidermal-dermal junction, the collagen is tightly packed in the papillary dermis. More loosely packed collagen is seen in the reticular dermis [20].

2.1.2 Aging of Human Skin

Human skin ages through chronological aging and photoaging. While chronological aging primarily depends on the passage of time, photoaging is skin damage by UV irradiation from the sun and from artificial UV sources. Photoaging is a cumulative process with sun exposure, where lightly pigmented skin is affected with the greatest degree of sun damage [12]. UV-B (290-320 nm) is mostly absorbed within the epidermis, while UV-A (320-400 nm) penetrates deeper into the dermis and is directly involved in the process of photoaging. Melanin absorbs UV radiation and protects the skin from photodamage. Photodamage in the epidermis is characterized by skin areas of atrophy, hyperplasia, nuclear atypia in keratinocytes, and dyspigmentation. The major alterations of photodamage are seen in the upper and mid-dermis, where accumulation of elastotic material (solar elastosis), degeneration of collagen network, and increase of glycosaminoglycans and proteoglycan complexes in the ground substance take place. These pathological alterations in photodamaged skin might be regulated by cytokines. UV radiation stimulates the production and the release of cytokines. Cytokines stimulate fibroblasts to upregulate the synthesis of extracellular matrix proteins and matrix

metalloproteinases (MMPs). The elevation of MMPs observed in UV-exposed skin leads to the degradation of dermal collagen. Reactive oxygen species (ROS) are also generated by UV radiation that enhances the oxidative damage in photodamaged skin. Interestingly, also cytokines regulate the induction of free radical scavengers for ROS in the protection against photoaging. Thus, photodamage of skin is the result of a dysbalance between the harmful effects and the protective effects of cytokines. Clinically, photoaged skin is seen as wrinkles, laxity, coarseness, teleangiectasia, purpura, and ultimately premalignant or malignant skin lesions [27].

2.2 Basic Principles of Lasers

2.2.1 Laser Light

The term "light" is used to describe UV radiation (180 nm to 400 nm), visible light (400 nm to 700 nm), and infrared radiation (700 nm to 15000 nm) [54]. Electromagnetic radiation is optical energy that can be described as a wave (Maxwell 1864) or a particle (Planck 1905). These quanta of energy suggested by Planck are also known as photons [18]. The wave and particle theory of light leads to the observation that an increase in wavelength of the associated wave will cause a decrease in photon energy. This can be explained by the Planck-Einstein equation:

$$E = h\nu, \tag{1}$$

where E is the energy of a photon, $h = 6.62 \cdot 10^{-34}$ Js is Planck's constant, and ν is the frequency of the electromagnetic wave. Here, the frequency is inversely proportional to the wavelength λ , as the speed of light is $c = \nu\lambda$ [56]. Bohr proposed the theory of electrons that surround a nucleus of an atom in 1913. These electrons can make spontaneous transitions between defined orbits resulting in spontaneous emissions of photons. In 1916, Einstein postulated the theory of stimulated emissions of photons [18]. This idea was initially used by Townes and Gordon for the design of a "microwave amplification by stimulated emission of radiation" (acronym: MASER) in 1955 [44]. Later in 1960, Maiman firstly demonstrated the production of "light amplification by stimulated emission of radiation" (acronym: LASER) by the use of a ruby crystal as the gain medium [31].

When light energy is added, an atom becomes excited by the absorption of this light, as the orbital electrons are shifted from a lower energy level to a higher energy level. The relaxation of an electron to its ground state is accompanied by the emission of a photon with a characteristic wavelength and energy. This characteristic energy is equivalent to the energy difference ΔE between the excited and ground state of the excited electron. If an already excited atom is perturbed by a photon with the same characteristic wavelength and energy, the incident and the resultant photon will be released with the same energy and also

synchronized in phase and direction. This process is called "stimulated emission" (Einstein 1916). When there are more atoms in the higher level than in the lower level, this (artificial) non-equilibrated state is called "population inversion" and leads to the occurrence of coherent light amplification, the leading process of laser light generation [18].

A laser hosts three essential components, which are the external energy or pump source, the gain or lasing medium, and the optical resonator (**Figure 2**). The energy source may be electrical discharge, radio frequency (RF), electrical criers, or a chemical reaction. The laser medium can be either solid, gaseous, or liquid. It principally determines the output wavelength. In its simplest form, the resonator is a tube with two parallel mirrors at the ends for amplification and release of the laser light. Photons produced by spontaneous emission are reflected by the mirrors back into the gain medium, where population inversion and amplification by stimulated emission can be achieved. The key properties of a laser beam are monochromaticity, coherence, and collimation. Lasers can be operated in continuous wave (cw) or pulsed mode [18].

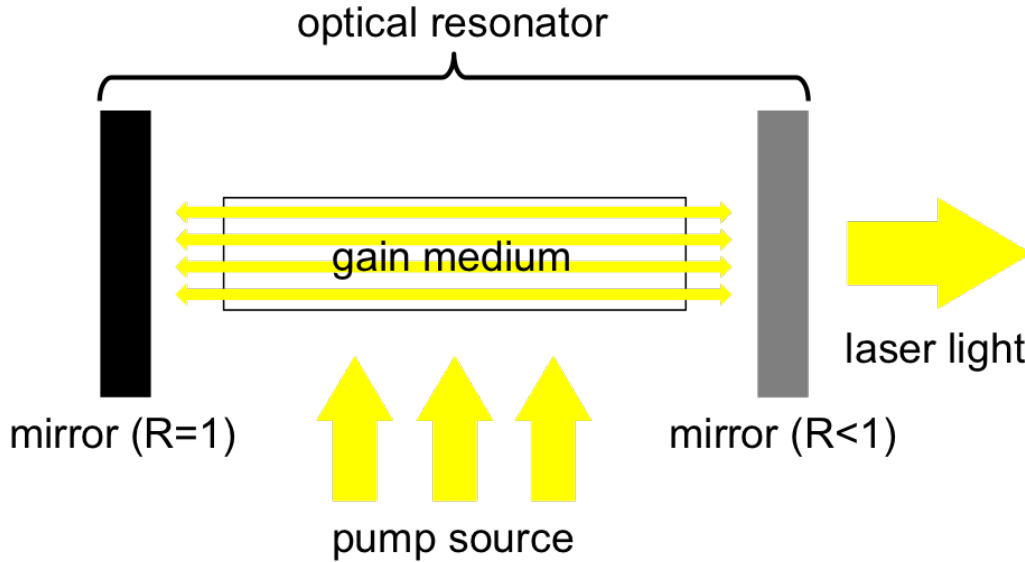


Figure 2. A laser consists of a pump source, a gain medium, and an optical resonator. The resonator is a tube formed by a highly reflective mirror ($R=1$) and a partially reflective mirror ($R<1$) at the ends for amplification and release of the laser light.

2.2.2 Laser Parameters

The interactions of laser light with tissue are highly dependent upon the properties of the incident laser beam. Thus, we will mention and define the major optical parameters that have a great influence on the tissue response [56]:

- wavelength λ [nm]
- power P [W]

- pulse energy E_p [mJ]
- beam diameter $2w_0$ [μm] (for a Gaussian beam, it is the full width of the beam at $1/e^2$) or often called as "spot size"
- irradiance I_0 [W/cm^2] or intensity is the power per unit area
- radiant exposure H_0 [J/cm^2] is the energy per unit area
- pulse duration τ_p [ms] or pulse width is the time of irradiation
- number of pulses in a train of pulses
- repetition rate f_{rep} [Hz] is the number of pulses emitted per second
- spectral profile is related to the wavelength, as it describes the power as a function of wavelength
- spatial profile is related to the spot size, as it describes the irradiance along the cross section of the beam
- temporal profile is related to the pulse duration, as it describes the power as a function of time during the pulse

The amount of ablated tissue is mostly dependent upon the pulse energy E_p , peak power P , the duration τ_p of a temporally-uniform pulse [58]

$$E_p = \tau_p P, \quad (2)$$

and the beam diameter $2w_0$. The beam width w at a position z along the beam propagation axis is defined as [23]

$$w(z) = w_0 \sqrt{1 + \left(\frac{z}{z_R} \right)^2}, \quad (3)$$

where w_0 is the beam waist at focal plane and $z_R = (\pi w_0^2)/\lambda$ is the Rayleigh range. In consideration of the beam quality factor M^2 , the Rayleigh range is altered to

$$z_R = \frac{\pi w_0^2}{M^2 \lambda}. \quad (4)$$

The Rayleigh range is the distance from the beam waist to the plane, in which the beam width $w(z)$ is by a factor of $\sqrt{2}$ greater than the beam waist (**Figure 3.A**). The ejected hot material can thermally damage the walls of the ablation channel. For very large spot sizes, the radiant exposure could be insufficient for ablation [58].

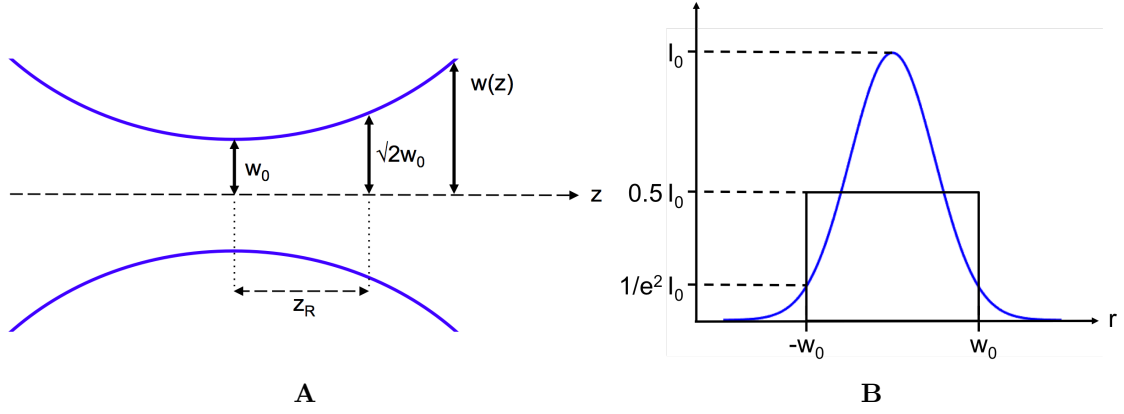


Figure 3. A: A focused Gaussian laser beam is schematically shown. The beam width $w(z)$ is defined at a position z along the beam propagation axis. The beam waist w_0 is located at the focal plane. The Rayleigh range z_R is the distance from the focal plane to the plane, in which the beam width increases to $\sqrt{2}w_0$. **B:** The peak intensity I_0 of a Gaussian laser beam profile (blue curve) has twice the maximum intensity of a uniform beam profile (black curve). The beam diameter $2w_0$ of a Gaussian beam is the full width of the beam (FWHM), where the intensity has decreased to $1/e^2$.

Typically, a laser beam has a Gaussian spatial profile with peripheral regions of subablative energy. A Gaussian laser beam usually creates an ablation crater that has the shape of an inverted cone. In contrast, a flat-top laser beam ablates tissue creating an ablation channel with flat bottom and cleaner boundaries. When applied for a Gaussian spatial profile, the calculation of the resulting intensity by dividing the total power by the spot size area yields the average intensity over the irradiated spot, where $2w_0$ is the full width at half maximum (FWHM). Thus, in the center of the laser beam, the actual intensity is twice as high as the average intensity for a Gaussian laser beam (**Figure 3.B**) [58].

2.3 Interactions of Laser Light with Tissue

The outcome of a light-tissue interaction can involve the absorption of laser light in tissue that causes the generation of heat, which again can thermally damage (coagulate) and ablate the absorbing material. In this section, we will briefly discuss the optical and thermal properties of skin tissue that influence the laser absorption and the resulting temperature rise and tissue ablation.

2.3.1 Optical Properties of Skin

The irradiance plays a decisive part in the tissue response to laser radiation, as it describes the laser power density delivered to a surface area on the skin. Diagnostic applications use low irradiances that do not lead to a significant temperature rise, whereas many therapeutic and surgical applications use high irradiances that can induce thermal and mechanical alterations in tissue [59]. Aside from the various optical parameters of the incident laser beam as discussed in **Section 2.2.2**, the interaction of laser light with any medium is also dependent

on the optical properties of the material itself [56, 60]:

- absorption coefficient μ_a [cm^{-1}] is used to define the probability for absorption $\mu_a dz$ of a photon over an infinitesimal distance dz
- scattering coefficient μ_s [cm^{-1}] is used to define the probability for scattering $\mu_s dz$ of a photon over an infinitesimal distance dz
- total attenuation coefficient μ_t [cm^{-1}] is the sum of μ_a and μ_s
- optical penetration depth δ [μm] is the path for an event of absorption or scattering, the depth where transmitted light is attenuated to $1/e \approx 37\%$, and it is defined as the reciprocal of μ_t
- index of refraction n

In general, optical properties of materials are dependent on e.g. wavelength, temperature, irradiance, pressure, and polarization state of light [56]. On the one hand, we can selectively target a chromophore within its surrounding tissue dependent upon the choice of wavelength. This wavelength-dependent absorption by a chromophore is also known as "selective photothermolysis" if the exposure time is shorter than the thermal relaxation time (**Section 2.3.2**) [4]. On the other hand, the absorption is often temperature-dependent and will change during irradiation of the target material. The tissue response to laser irradiation involves a complex interaction of numerous factors and their interdependencies, which makes a fully-developed dynamic model for laser-tissue interaction still very challenging.

In brief, when light strikes a material, there are four events that could occur. These are transmission, reflection, scattering, and absorption of light. Reflection and transmission take place at an interface separating two materials of refractive indices. A part of the incident light is reflected from the surface interface toward the light source, while the remainder is refracted and transmitted into the material. However, tissue surface is not optically flat. There is variation in angle of incidence across the tissue surface and the light is reflected in various directions, which is called diffuse reflection. Further, the index of refraction n within skin tissue is not constant. Reflections and refractions occur multiple times at cell boundaries. As a result, the direction of light propagation changes while light interacts with tissue [56].

The optical window in biological tissues is defined as the range from 650 nm to 1350 nm, where laser light has its maximum of optical penetration depth δ and its minimum of absorption coefficient μ_a in tissue. Within this wavelength window, scattering is the most dominant interaction of laser light with tissue [48]. Scattering by small particles is called Rayleigh scattering, where the particle size r is much smaller than the wavelength of light ($r \ll \lambda$). Scattering is referred to as Mie scattering if the particle size r is much larger than the wavelength of light ($r \gg \lambda$) [56].

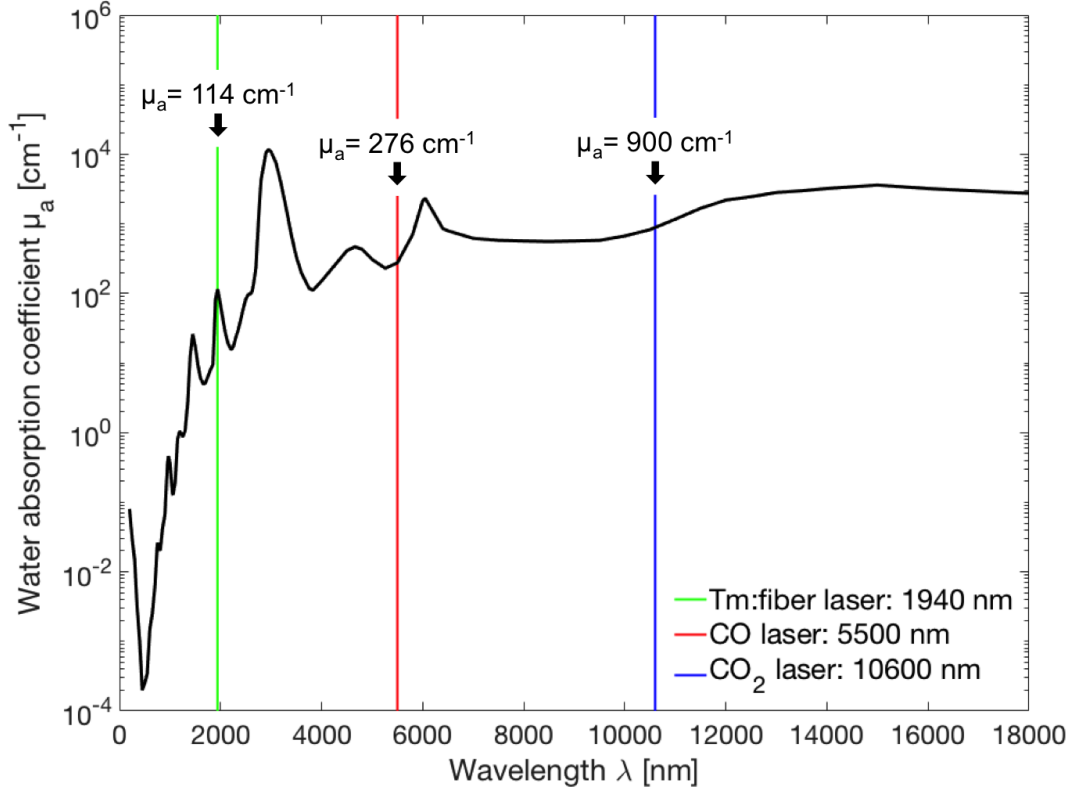


Figure 4. The absorption coefficient μ_a of water is shown for the range of infrared light λ [24]. Tissue water in skin is the target absorber for lasers that emit in the infrared spectral region. The water content of skin is about 70%. The absorption coefficients were modified to 630 cm^{-1} at 10600 nm, 193.2 cm^{-1} at 5500 nm, and 79.8 cm^{-1} at 1940 nm wavelength.

As only a small portion of light (about 4%) is reflected at the tissue surface [11], the propagation of collimated laser light through tissue is mainly attenuated by absorption and scattering with depth z according to Beer-Lambert's law [60]

$$\frac{I(z)}{I_0} = e^{-(\mu_a + \mu_s)z}, \quad (5)$$

where I_0 is the intensity of the incident laser beam, $I(z)$ is the attenuated intensity with depth, μ_a is the absorption coefficient, and μ_s is the scattering coefficient of the tissue. There is a wide spectrum of available laser sources for diagnostic and therapeutic applications ranging from 193 nm to 10600 nm wavelength. Laser light at 193 nm and 10600 nm is totally absorbed within a few micrometer of tissue depth based on strong absorption by amino acids in the UV and by water in the infrared range [59]. The absorption coefficient of water as a function of wavelength is depicted in **Figure 4** for infrared light. Above 1400 nm wavelength, scattering becomes negligible compared to absorption in tissue ($\mu_a \gg \mu_s$) so that Beer-Lambert's law is simplified to [60]

$$I(z) = I_0 e^{-\mu_a z}. \quad (6)$$

Typically, tissue ablation is performed, where water absorption is dominant over scattering and when the absorbed radiant exposure is several times the ablation threshold. If scattering is negligible, the optical penetration depth δ is defined as the reciprocal of the absorption coefficient μ_a

$$\delta = \frac{1}{\mu_a}, \quad (7)$$

which is equivalent to the characteristic depth of laser energy deposition [55].

Laser sources that target water absorption in the infrared spectrum have become the main focus of interest for medical applications owing to the high mutagenic potential of UV light (**Section 2.1.2**). The maximum of water absorption in the infrared region is found at 2940 nm wavelength [54, 56]. Ablative lasers such as 193 nm argon fluoride (ArF) excimer laser, 2940 nm erbium:yttrium aluminum garnet (Er:YAG) laser, and 10600 nm carbon dioxide (CO₂) laser performing precise ablation at tissue surfaces in air cannot be delivered well through optical fibers. For the performance of tissue ablation in human cavities using quartz fibers, 308 nm xenon monochloride (XeCl) excimer laser, 2000 nm thulium fiber (Tm:fiber) laser, and 2100 nm holmium:yttrium aluminum garnet (Ho:YAG) laser are typically employed [55].

2.3.2 Thermal Properties of Skin

Heating of the absorbing material is a common result of laser absorption. In particular, the selective heating of a target absorber within the tissue requires a wavelength that is predominantly absorbed by the target, a small focused beam, a short pulse to confine the absorbed energy, and a high radiant exposure to achieve a sufficient temperature rise [56, 51]. Ultimately, the resulting temperature rise will determine the degree of ablation and thermal damage in tissue. The temperature increase is associated with a higher rotational or vibrational state of the absorbing molecule. The absorbed energy by the tissue is directly proportional to the temperature rise ΔT as follows [56]

$$\Delta T = \frac{\mu_a H}{\rho c_v}, \quad (8)$$

if no heat diffusion during the laser pulse takes place. Here, H is the radiant exposure, ρ is the tissue density, and c_v is the specific heat capacity of the absorbing material. The thermal confinement requires a pulse duration τ_p shorter than the thermal diffusion time τ_{tc} estimated by the absorber size [56]

$$\tau_{tc} \approx \frac{r^2}{4\kappa}, \quad (9)$$

where r is the radius, $\kappa = k/(\rho c_v)$ is the thermal diffusivity, and k is the thermal conductivity of the target absorber. Therefore, a small target absorber will cool more quickly and requires a shorter pulse duration to avoid heat conduction. Consequently, an extension of the pulse duration can decrease the ablation efficiency and increase the residual thermal damage zone [58].

The temperature distribution within the tissue resulting from the laser-tissue irradiation will also be influenced by the thermal properties of the different skin layers as summarized in **Table 1** [59, 53]:

- thermal conductivity k [W/(mK)] is the property of a material to conduct heat when subject to a temperature gradient
- specific heat capacity c_v [J/(kgK)] or specific heat describes the amount of thermal energy that can be stored per unit mass of a material at a specific temperature
- thermal diffusivity κ [mm²/s] measures the rate of heat transfer of a material, where high thermal diffusivity leads to rapid heat conduction across the material relative to its heat capacity

The thermal properties of the tissue are also dependent upon the temperature of the tissue. Thermal properties of most tissues increase with temperature [53].

Table 1. Thermal Properties of Skin Tissue.

material	ρ [kg/m ³]	k [W/(mK)]	c_v [J/(kgK)]	κ [mm ² /s]
water	1000	0.6 [64]	4181.9 (293.15 K)	0.1435
stratum corneum	1500 [63]	0.235 [63]	3600 [63]	0.0435
epidermis	1190 [63]	0.235 [63]	3600 [63]	0.0549
dermis	1116 [63]	0.445 [63]	3300 [63]	0.1208
subcutaneous fat	971 [63]	0.185 [63]	2700 [63]	0.0706

ρ : density, k : thermal conductivity, c_v : specific heat capacity, κ : thermal diffusivity

2.3.3 Thermal Effects in Skin

The laser-induced temperature gradient will cause a transport of heat from the heat source within the irradiated tissue volume into the cooler periphery over time. Thus, zones of thermal injury along the temperature gradients can be found, where thermal effects are more severe when located closer to the heat source volume. A rise in temperature could change tissue composition and structure, such as water loss or protein denaturation, that results in

alteration of optical and thermal properties [51, 53]. A thermal lesion in skin tissue exposed to laser irradiation could exhibit a center of ablated tissue, which is surrounded by a thin inner layer of dark carbonized tissue and an outer layer of desiccated and thermally denatured tissue (**Figure 5**). The thermal denaturation of collagen fibers (coagulation) begins when the native triple-helical structure is transformed into a random coil structure, which is accompanied by shrinkage of the collagen fibers in length. Further heating leads to a progressive disintegration and finally results in a total mechanical failure of the tissue structure [34, 55, 51].

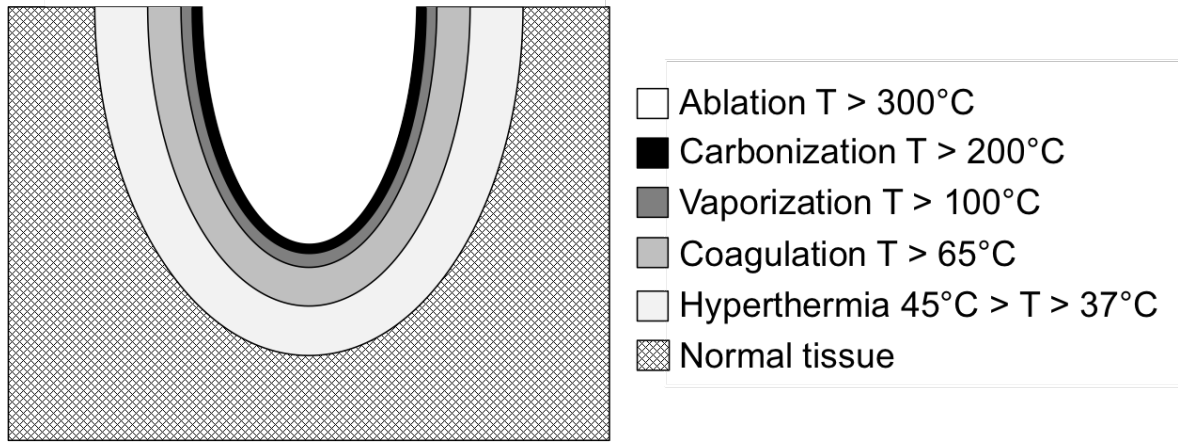


Figure 5. Direct thermal effects in tissue form concentric zones of thermal damage surrounding the hot center of laser irradiation, where tissue is ablated [51, 43].

The following list begins with laser-mediated thermal effects that occur with lower temperatures and longer exposure times, such as hyperthermia and coagulation, and ends with ablation that occurs with high temperatures requiring high radiant exposures delivered in short exposure times. The extent of the thermal effect is principally defined by the energy density, which depends on temperature T and exposure time τ_p according to the Arrhenius formalism [7]. Thus, the ablation threshold can also be reached with lower radiant exposures when the exposure time is lengthened, resulting in a lower temperature. The temperatures and exposure times required for thermal effects to occur are also dependent upon the type of tissue. A simplified relation between temperature and thermal effects in skin is listed here as [51, 43]:

- hyperthermia ($45^{\circ}\text{C} > T > 37^{\circ}\text{C}$) is a transient and reversible thermal effect
- coagulation ($T > 65^{\circ}\text{C}$) is referred to the thermal denaturation of proteins with highly organized molecular structures due to broken hydrogen, ionic, sulfide or other covalent bonds, which causes structural and functional change or even loss of biological function
- vaporization ($T > 100^{\circ}\text{C}$) of water generates water steam that can be trapped within tissue resulting in explosive fragmentation of the tissue, when vapor diffusion out of the tissue is slower than the formation and expansion of steam vacuoles

- carbonization ($T > 200^\circ\text{C}$) is the reduction of organic material to elemental carbon that forms a thin black inner layer on the walls of the ablation crater
- ablation ($T > 300^\circ\text{C}$) is defined as the removal of tissue volume leaving behind a crater in the tissue as a result of tissue vaporization (phase change), plasma formation (ionization of molecules), explosive fragmentation (rapid expansion of water steam), or combustion (rapid oxidation of organic material)

Tissue ablation occurs when the vapor pressure increases during laser heating and finally exceeds the ultimate tensile strength of the tissue. This process is termed "confined boiling". Due to the stiffness of the extracellular matrix, an explosive material removal takes place, where fragmented tissue is ejected by the vaporization of tissue water. For photothermal disruption of skin tissue, temperatures of $400\text{--}700^\circ\text{C}$ are required to generate vapor pressure that exceeds the ultimate tensile strength. Thus, the ablation enthalpy of tissue can be higher than the vaporization enthalpy of water as described in **Section 2.3.4** [55].

2.3.4 Threshold, Enthalpy, and Efficiency of Ablation

For instantaneous heating without heat diffusion, the ablation threshold H_{th} is defined as the minimum radiant exposure required for ablation or material ejection to occur

$$H_{th} = \frac{W_{abl}}{\mu_a}, \quad (10)$$

where W_{abl} (for water: 2594 J/cm^3) is the local volumetric energy density or the total heat of ablation and μ_a is the absorption coefficient for a specific wavelength [55, 25]. In principle, the ablation process is initiated when the energy density required to rise the temperature of water from its initial temperature $T_0 = 20^\circ\text{C}$ to boiling temperature $T_v = 100^\circ\text{C}$ and to induce the phase transition of water from liquid to gas phase. The total heat of ablation is then given by

$$W_{abl} = \varrho(c_v\Delta T + L_v), \quad (11)$$

where ϱ is the density of the material, c_v is the specific heat capacity of the material, ΔT is the absolute temperature rise, and L_v is the vaporization enthalpy (for water: 2257 J/g). However, vaporization of water is not the leading mechanism that drives the ablation of tissue for short-term ablation. Phase transition and rapid volume expansion of water do not occur at 100°C . Rather the energy is deposited rapidly leading to temperature rise and high pressures within the tissue. As a result, the enthalpy required to ablate tissue will be higher than the enthalpy of water vaporization and explosive ablation of the tissue occurs due to volume expansion of tissue [55, 58, 25].

The ablation efficiency $\eta_{abl} = (\rho\delta)/H_0$ describes the total laser energy required to remove a certain tissue mass. The ablation efficiency increases with incident radiant exposure, but decreases with higher ultimate tensile strength. For skin, the maximum ablation efficiency is achieved at radiant exposures that are several times higher than the ablation threshold [55, 25].

2.3.5 Ablation Models

The ablation event is a complex and dynamic process that involves numerous optical, thermal, and mechanical tissue parameters and their interdependencies. Thus, a fully-developed dynamic model for the prediction of the ablation event is more sophisticated than it appears at first glance. Two ablation models describing the ablation behavior for extreme time regimes are the steady-state model for pulse durations much longer than the thermal relaxation time ($\tau_p \gg \tau_{tc}$) and the blow-off model for pulse durations much shorter than the thermal relaxation time ($\tau_p \ll \tau_{tc}$). The thermal relaxation time τ_{tc} is defined as [55]

$$\tau_{tc} = \frac{1}{\kappa\mu_a^2}, \quad (12)$$

where κ is the thermal diffusivity and μ_a is the absorption coefficient. For pulses much shorter than the thermal relaxation time, the absorbed energy is confined within the heated tissue volume with a thickness of the optical penetration depth $\delta = 1/\mu_a$ (thermal confinement).

The blow-off model for prediction of the ablation depth is based on Beer's law according to **Equation 6**. Here, the condition of thermal confinement must be satisfied meaning the laser pulses must be shorter than the thermal diffusion time defined in **Equation 12**. The blow-off model assumes that incident radiant exposures H_0 above the threshold radiant exposure H_{th} will initiate ablation at the end of the laser pulse if no heat diffusion happens during the short exposure time τ_p . For incident radiant exposures below ablation threshold, only heating of the tissue will occur. The etch depth $\delta_{blow-off}$ (**Figure 6.A**) is then predicted by

$$\delta_{blow-off} = \frac{1}{\mu_a} \ln \left(\frac{H_0}{H_{th}} \right) = \frac{1}{\mu_a} \ln \left(\frac{I_0 \tau_p}{H_{th}} \right). \quad (13)$$

The steady-state model assumes that tissue removal begins right after the onset of the laser irradiation and that it continues during the whole laser pulse. The steady-state model can be applied for longer laser pulses that exceed the thermal diffusion time defined in **Equation 12**. Different from the blow-off model, the etch depth does not explicitly dependent on the absorption coefficient, as $H_{th} = \rho h_{abl}/\mu_a$. Here, the ablation enthalpy h_{abl} is a constant and proportional to the threshold radiant exposure H_{th} . For incident radiant exposures above the ablation threshold, the etch depth $\delta_{steady-state}$ (**Figure 6.B**) will increase linearly with

radiant exposure H_0 meaning with exposure time τ_p

$$\delta_{steady-state} = \frac{H_0 - H_{th}}{\rho h_{abl}} = \frac{I_0 \tau_p - H_{th}}{\rho h_{abl}}. \quad (14)$$

Since the blow-off and the steady-state models are limited to extreme time regimes, where the exposure time is either in the range of nanoseconds or in cw, ablation using laser pulses close to the thermal relaxation time are not accurately described.

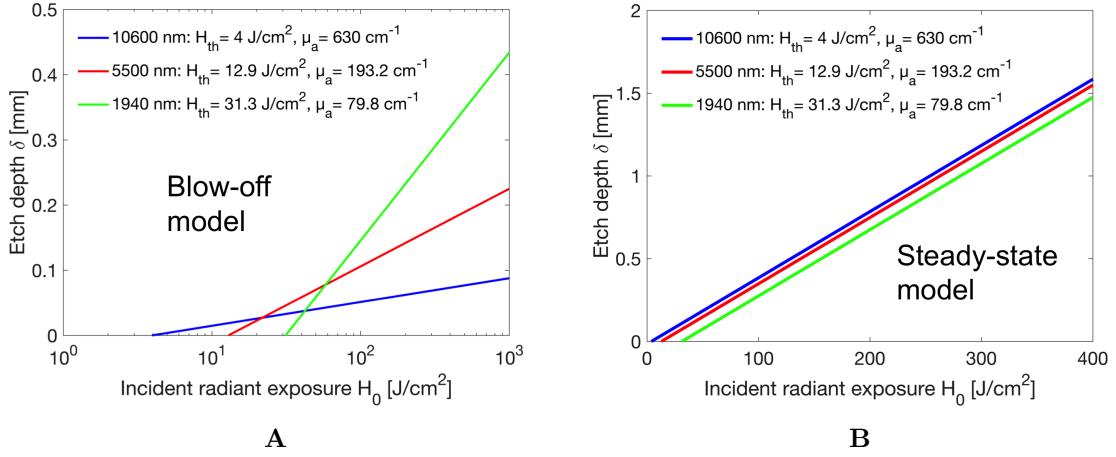


Figure 6. Comparison of blow-off and steady-state ablation models showing the predicted etch depth δ for different absorption coefficients μ_a (compare with **Figure 4**). **A:** Blow-off model predicts the etch depth as a function of radiant exposure H_0 in a logarithmic scale (**Equation 13**) if no heat diffusion occurs during the laser pulse for exposure times much shorter than the thermal relaxation time. **B:** Steady-state model predicts the etch depth as a function of radiant exposure H_0 in a linear scale (**Equation 14**) if heat diffusion occurs for exposure times much longer than the thermal relaxation time.

The Hibst modification is an approach to connect the blow-off and the steady-state ablation models. The predicted etch depth is anticipated to be effected by the plume absorption, where $\gamma = \mu_{plume}/\mu_a$ is described as an indicator of the plume absorption μ_{plume} relative to the absorption coefficient of tissue μ_a . The etch depth δ_{hibst} is then given by

$$\delta_{hibst} = \frac{1}{\mu_a \gamma} \ln \left(\gamma \frac{H_0}{H_{th}} - \gamma + 1 \right). \quad (15)$$

Further, this suggested modification is supposed to be equivalent to the blow-off model, when the ablation plume has an identical absorption coefficient as the target tissue ($\gamma \rightarrow 1$). It can be reduced to the steady-state model, when the ablation plume is transparent to the incident laser radiation ($\gamma \rightarrow 0$) [55].

However, this interpretation based on plume absorption according to Hibst is very questionable. The indicator γ could be regarded as a correction factor (fit parameter) for experimental results, where the applied exposure time is too close to the thermal relaxation time ($\tau_p \approx \tau_{tc}$).

As a correction factor, γ could roughly indicate whether an ablation process has a trend towards the blow-off model ($\gamma \rightarrow 1$) or towards the steady-state model ($\gamma \rightarrow 0$).

2.4 Applications in Dermatology

2.4.1 Fractional Laser Resurfacing

”Fractional photothermolysis” suggests the production of small and thermally confined tissue effects using focused laser beams [32]. Laser fractionation of the skin has been clinically proven to successfully treat deep wrinkles, acne scars, actinic keratosis, and pigmentation disorders. These microscopic treatment zones are surrounded by undamaged tissue that reduces side effects and may contribute to faster wound healing in contrast to traditional full-face laser resurfacing [38]. The thermal injury with intact connective tissue scaffolding induces a wound healing process that involves inflammation, tissue regeneration, tissue repair, and scar tissue formation. Macrophages as inflammatory cells phagocytose the necrotic debris of the thermally injured tissue and are integrated into the healing tissue. The epidermis of the skin tissue has the ability to regenerate after necrosis. Precursor cells in the residual, viable tissue are stimulated by growth factors to undergo proliferation, migration, and differentiation into mature cells. The proliferating cells are guided into the connective tissue scaffolding in order to form new organized and functional tissue. The tissue defect can be filled with regenerating tissue or granulation tissue or a combination of both [51].

The wound healing response is still provided even if the microscopic treatment zones are extended down to the reticular dermis [38]. However, uncontrolled thermal damage can result in severe pain and prolonged wound healing. The ideal laser system for fractional laser resurfacing should offer an adjustable ratio of ablation to coagulation (ACR). The ablation depth and the thermal damage zone are principally dictated by the laser wavelength, as the absorption of laser light in tissue water is wavelength-dependent. Additionally, exposure parameters such as pulse energy, pulse length, and spot size will also influence the outcome.

2.4.2 The Gold Standard CO₂ Laser

The CO₂ laser has become one of the most widely used lasers for resurfacing of the facial skin [34]. The CO₂ laser operates at 10600 nm wavelength, where laser energy is strongly absorbed within a short distance of about 15 μm in tissue. The production of high-energy, short-pulsed CO₂ lasers with smart scanning technologies have been accomplished [18]. However, the CO₂ laser has several limitations. The strong absorption at this operation wavelength produces bleeding during the laser treatment. The short optical penetration depth results in a minimal thermal damage zone, which could limit the effect of tissue tightening. The CO₂ laser has a large beam diameter of 120 μm due to longer wavelength. Smaller spot sizes are difficult to

achieve. Further, the delivery of CO₂ laser light requires an articulated mirror arm, which impedes its surgical application in cavities.

2.4.3 The Potential of CO Laser

Tissue cutting and coagulation using a 15 W CO laser was firstly reported in 1983. It was observed that the CO laser generates a larger coagulation zone at a lower power level than the CO₂ laser as a result of the higher optical penetration depth of 50 μm in the wavelength range of 5000-5400 nm [2]. The early CO laser in vitro experiments achieved tissue removal with a depth of 2 mm and a coagulation zone of 1.5 mm in muscle tissue using a beam diameter of 700 μm , irradiance of 25 kW/cm², and long pulses of 5 s [1]. With the recent availability of a 100 W CO laser, ablation using high-energy pulses can be performed. A shorter wavelength allows tighter focusing, as the beam diameter scales with wavelength. A smaller spot size will increase the irradiance. Potentially, smaller ablation holes could decrease the social downtime after laser skin resurfacing due to reduced area of injury. The shorter wavelength will provide a higher Rayleigh range if the same spot size is generated. In contrast to the CO₂ laser, flexible optical fibers with lower optical losses are expected in the CO laser operation range [2, 1].

2.4.4 The Potential of Tm:Fiber Laser

Primarily, the Tm: fiber laser is known as a non-ablative fractional laser device that induces coagulation of epidermis and superficial dermis [28]. In urology, the Tm: fiber laser has demonstrated its potential to vaporize prostate tissue in the treatment of benign prostatic hyperplasia and to cut urinary tissue in the treatment of urethral strictures. A 40 W Tm: fiber laser has been used with a 300 μm beam diameter. The laser incision has shown a depth of 500 μm and a coagulation zone of 500 μm for the use of a 10 ms pulse duration and a 200 mJ pulse energy. The massive thermal damage zone was a result of the long exposure time [15]. The availability of 120 W Tm: fiber lasers allows the generation of high-energy pulses with shorter pulse durations sufficient to ablate skin tissue and to reduce the thermal damage zone observed in previous reports. Based on the high optical penetration depth of 125 μm at 1940 nm wavelength, larger thermal damage zones are expected in comparison to the CO laser and the CO₂ laser. Also, there is a flexible optical fiber delivery available for applications with the Tm: fiber laser producing a single-mode spatial beam profile.

3 Materials and Methods

The laser exposures on ex vivo human abdominal skin were performed using a clinical CO₂ laser system, a custom-built, pulse-width-modulated CO₂ laser system, a novel CO laser, and a Tm:fiber laser. We compared the different lasers at constant or similarly adjusted exposure parameters. The pulse energy was adjusted by variation of laser power. We used a pulse length of 2 ms and a focal beam diameter of 108-120 μm maintained for all lasers. In particular, there were differences in the temporal pulse structure, which will be described in **Section 3.2.1**.

3.1 Laser Systems

3.1.1 Clinical 10600 nm CO₂ Laser System

We used a 95 W average power, ablative fractional CO₂ laser system (UltraPulse[®], Lumenis Ltd., Yokneam, Israel) that is clinically applied for laser skin resurfacing (**Figure 7**). The CO₂ laser is a sealed gas laser that operates from radio frequency (RF) electrical power to excite the CO₂ gas mixture with laser emission at 10600 nm wavelength. The clinical CO₂ laser system does not allow a user-controlled variation of the pulse width. The pulse energy is implemented by internal modulation of the pulse length ranging from 90 μs to 2 ms. We measured a pulse duration of 2 ms at the highest pulse energy of about 190 mJ. Each macroscopic laser pulse is composed of a train of microoscillations at a 2 MHz frequency, which have the effect of generating 220 ns FWHM-micropulses (**Figure 12**).

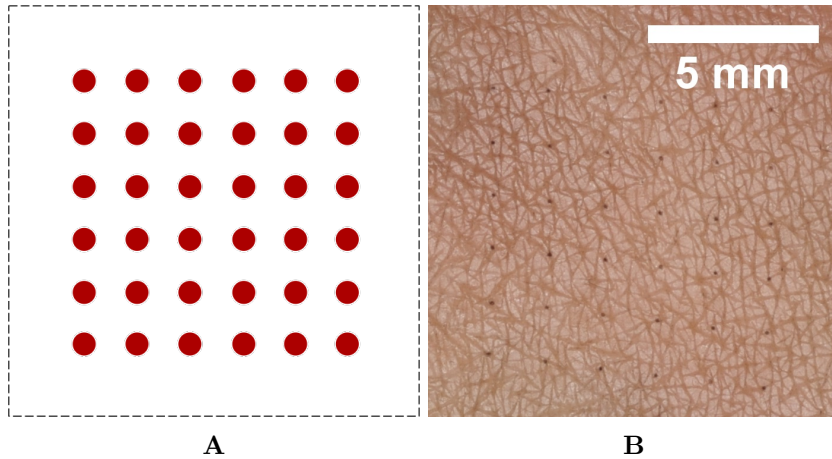


Figure 7. **A:** Laser generated pattern of microscopic treatment zones (red dots) is schematically shown. **B:** The fractional holes in ex vivo human skin are generated by the clinical CO₂ laser system using the scanning handpiece. The skin that is adjacent to the fractional holes stays intact. The holes were filled with black ink for visualization.

The laser beam is delivered through an articulated arm that consists of a system of mirrors

and lenses (**Figure 8**). The beam delivery system is mounted with a spherical shoulder joint enabled for 360° rotation. The machine is equipped with a self-contained and a closed cycle cooling system. Different scanning optics are available, such as DeepFX™ (0.12 mm spot size), ActiveFX™ (1.3 mm spot size), and TotalFX™ (0.12 mm/1.3 mm spot sizes). The 120 μ m DeepFX™ handpiece consists of a planoconvex ZnSe lens ($f = 50$ mm). The pattern of microscopic treatment zones (fractional holes) is generated within a laser scanned area of 10 mm×10 mm, where the coverage range describes the ablated area versus thermally undamaged area (**Figure 7**).

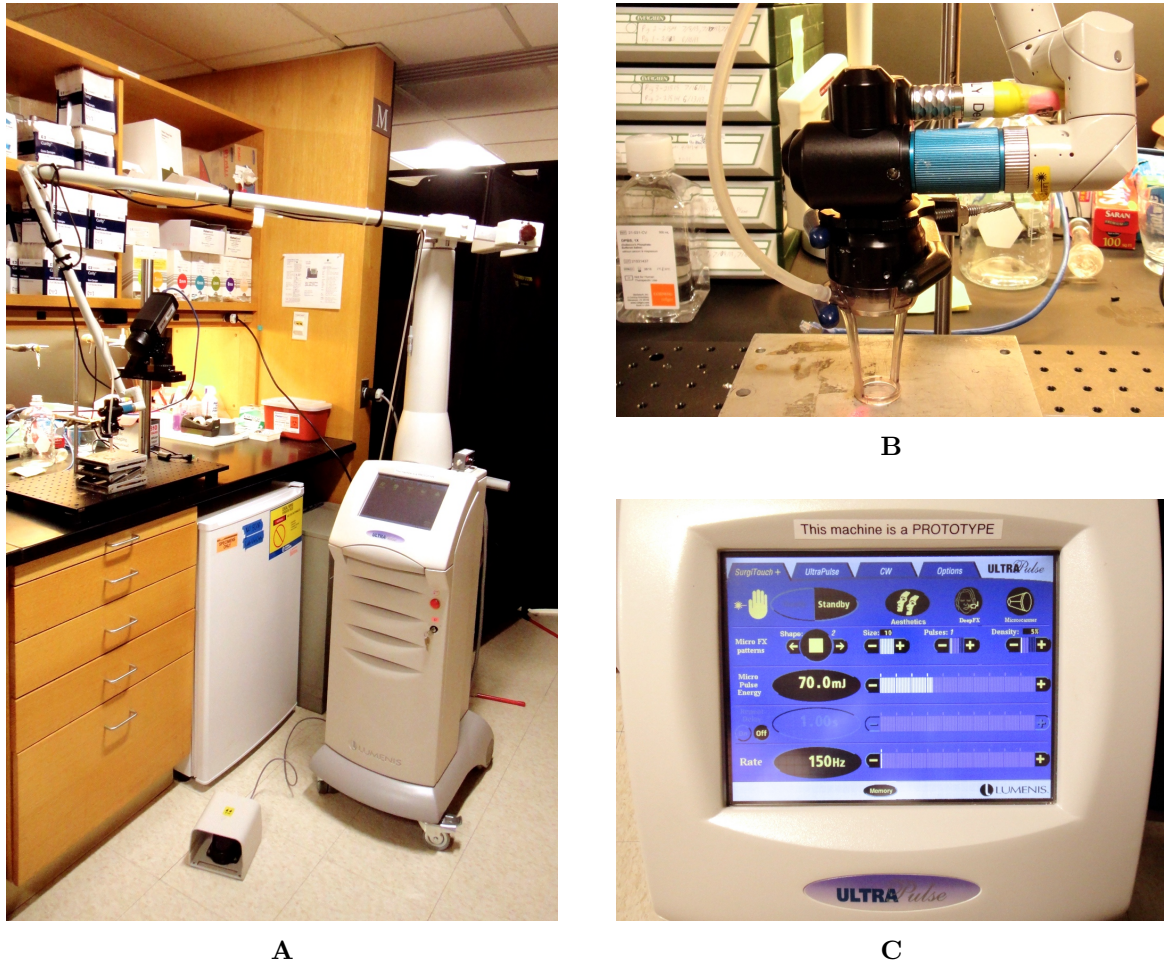


Figure 8. CO₂ laser setup in the clinical version (no control of pulse shape and pulse duration) or the modified version (external programming of the temporal pulse profile) [61]. **A:** CO₂ laser system (UltraPulse®, Lumenis Ltd., Yokneam, Israel) with articulated mirror arm and footswitch. **B:** DeepFX™ scanning handpiece delivers 0.12 mm spot sizes. **C:** User control panel allows setting of pulse energy (10-190 mJ), scan area, coverage range, and scan rate.

3.1.2 Modified 10600 nm CO₂ Laser System

A modified version of the UltraPulse® CO₂ laser system was used that allows external control of the pulse duration and the temporal pulse profile. The modification enables the external

access to the main RF amplifier cable connection on the main driver circuit board, which is used for modulation of the RF power supply to the laser tube. The pulse width modulation was achieved by turning the voltage source on and off at a repetition frequency of 50 kHz. The very fast switching generates a pulsing structure with a more constant power level over the pulse width but still exhibits the same microoscillation behavior as the clinical CO₂ laser system. Here, the power output measured behind the lens of the 120 μm DeepFX™ handpiece was limited to 70 W. We used a fixed pulse duration of 2 ms delivered over a range of pulse energies from 20-132 mJ [61].

3.1.3 5500 nm CO Laser

A new generation of liquid cooled 100 W average power CO laser (GEM-100™, Coherent Inc., Santa Clara, CA, USA) was tested (**Figure 9**). This laser is a sealed-off, cw RF-excited waveguide device that we gated to generate comparable energy, 2 ms duration macroscopic laser pulses to those generated by the CO₂ lasers.

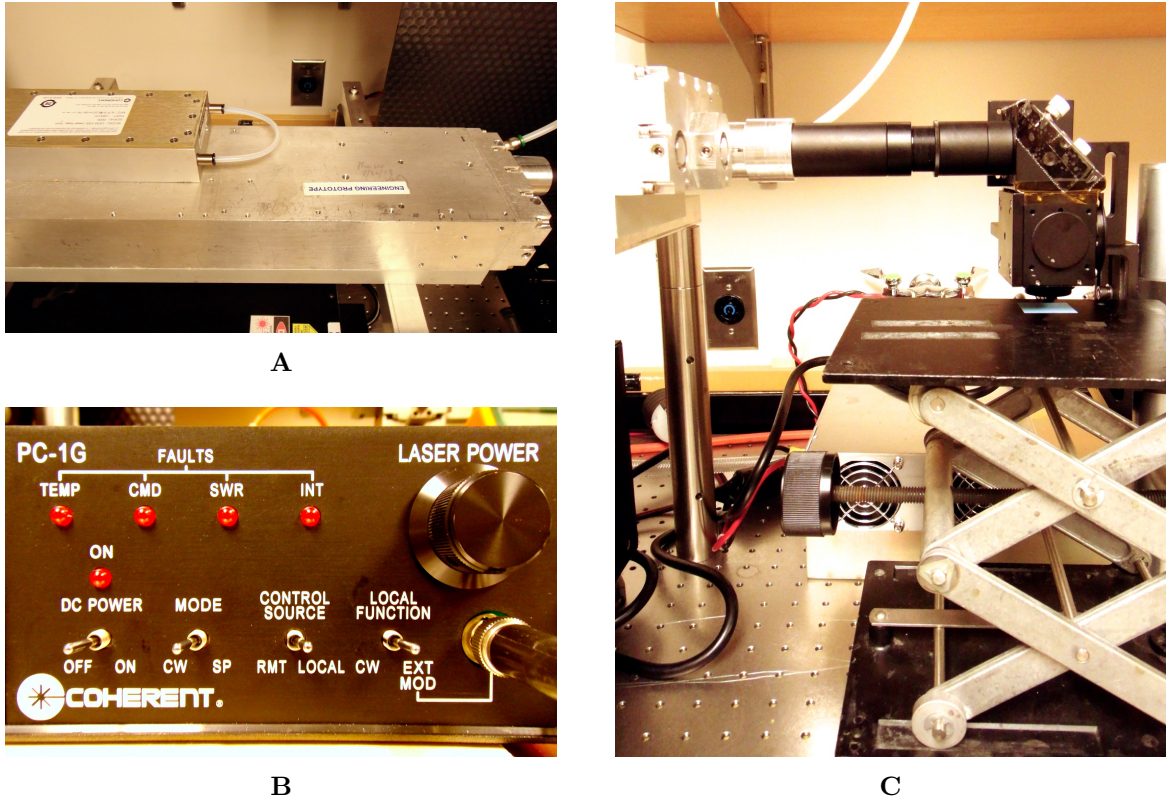


Figure 9. CO laser setup. **A:** The RF electric field is used to excite the gas mixture in the liquid cooled CO laser head assembly (GEM-100™, Coherent Inc., Santa Clara, CA, USA). **B:** The electronic interface allows setting of laser power and enables the external pulse modulation. It is connected to the RF power supply. **C:** The CO laser beam is delivered in a nitrogen purged tube (gas purge pressure of about 10 psi) to avoid atmospheric water absorption. The laser beam is folded by a 90° angle coated mirror, focused by a lens, and delivered perpendicular to the skin surface.

The RF power supply is connected to the laser head assembly via coaxial cable. The RF power supply converts standard DC 50/60 Hz power to RF power. The RF electric field is used to excite the CO gas mixture in the laser head. The laser head contains a folded optical waveguide resonator and converts RF input power to laser radiation. The CO laser emits 95% of the laser power at a wavelength range of 5500 ± 275 nm. Waste heat from the laser head and the RF power supply is exhausted through coolant (mixture of 70% water and 30% propylene glycol with corrosion inhibitors) flow from a refrigerated recirculator (**Figure 10**).

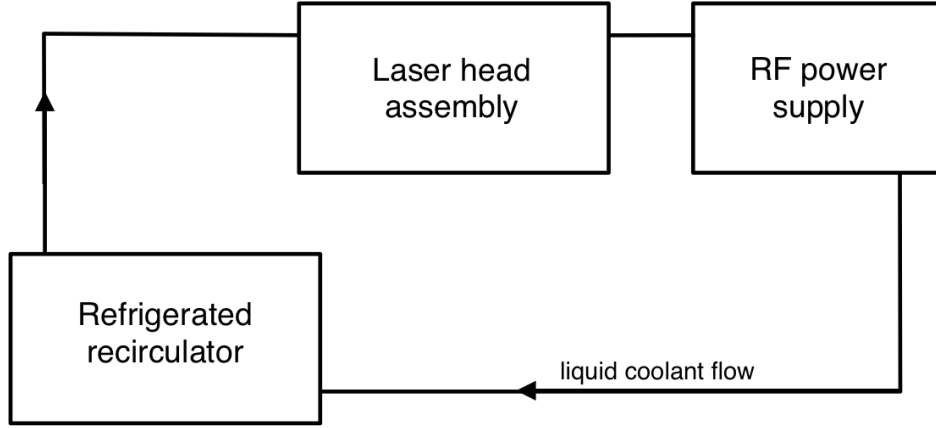


Figure 10. Cooling system functional block diagram for the CO laser. The laser head and the RF power supply are connected in series. The laser head receives the lowest coolant temperature ($15\text{-}30^{\circ}\text{C}$) as it is the first element of the cooling system.

We measured a RF excitation frequency of 45 MHz and microoscillations of 6.5 MHz frequency within the ms-pulses that were not deeply modulated enough to provide distinct 90 ns FWHM-micropulses as shown in **Figure 12**. A laser beam transport system purged with nitrogen gas was built to avoid absorption of CO laser light in atmospheric air. We used a biconvex CaF_2 lens (LB5774, $f = 25.4$ mm, Thorlabs Inc., Newton, NJ, USA) for focusing of the CO laser beam.

3.1.4 1940 nm Tm:Fiber Laser

A 120 W average power cw 1940 nm wavelength Tm: fiber laser (TLR-120-1940, IPG Photonics Corporation, Birmingham, AL, USA) was gated to generate 2 ms duration macroscopic laser pulses (**Figure 11**). Waste heat is removed through distilled water as the coolant ($21\text{-}23^{\circ}\text{C}$) from a refrigerated recirculator. In contrast to the CO_2 laser systems and the CO laser, the Tm: fiber laser has a rectangular-shaped temporal pulse structure with no microstructure (**Figure 12**). The Tm: fiber laser beam was focused using a planoconvex ZnSe lens (88-007, $f = 254$ mm, Edmund Optics Inc., Barrington, NJ, USA).

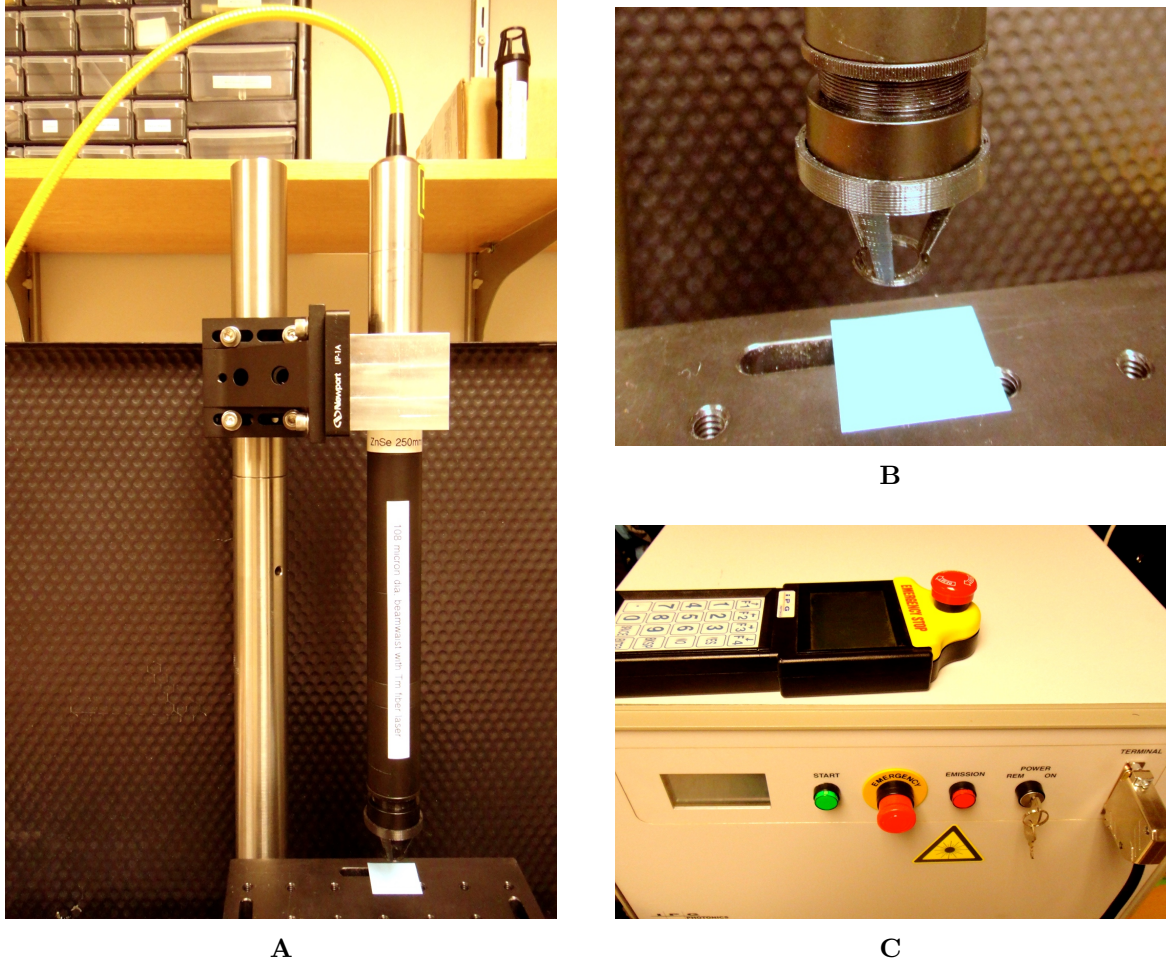


Figure 11. Tm:fiber laser setup. **A:** Single mode optical fiber output port terminates in a fixed collimator. The output collimator is mounted in a metal block, which is attached to an extension tube. **B:** The extension tube is connected to a custom-built distance holder and contains a focusing lens. **C:** Tm:fiber laser module (TLR-120-1940, IPG Photonics Corporation, Birmingham, AL, USA) has a front panel and is connected to a remote hand-held interface with keypad for power level setting and external pulse modulation.

3.2 Beam Parameter Measurements

3.2.1 Temporal Pulse Profile

We adjusted a pulse length of 2 ms for all laser systems, as the highest pulse energy of about 190 mJ was found at this pulse duration for the clinical CO₂ laser system. Further, we compared all lasers at radiant exposures $H_0 = n \times H_{th}$ higher than the ablation threshold H_{th} by a factor n . As the ablation threshold of the Tm:fiber laser is higher than those of the CO₂ lasers and the CO laser, higher radiant exposures are required for ablation (**Equation 10**). This could be better achieved with ms-pulses at maximum laser power. However, no heat diffusion during the laser pulse requires a pulse duration τ_p much shorter than the thermal diffusion time τ_{tc} according to **Equation 12**. To calculate the thermal relaxation time, we assumed a water content of 70% in skin and the thermal properties of water [64], such as thermal conductivity $k = 0.6 \text{ W/(mK)}$, density $\rho = 1000 \text{ kg/m}^3$, and specific heat capacity

$c_v = 4181.9 \text{ J/(kgK)}$. Thus, the 2 ms pulses of the CO laser ($\tau_{tc} = 18.7 \text{ ms}$) and the Tm:fiber laser ($\tau_{tc} = 109.4 \text{ ms}$) were thermally confined. But the 2 ms pulses of the CO₂ laser ($\tau_{tc} = 1.8 \text{ ms}$) were longer than the thermal diffusion time.

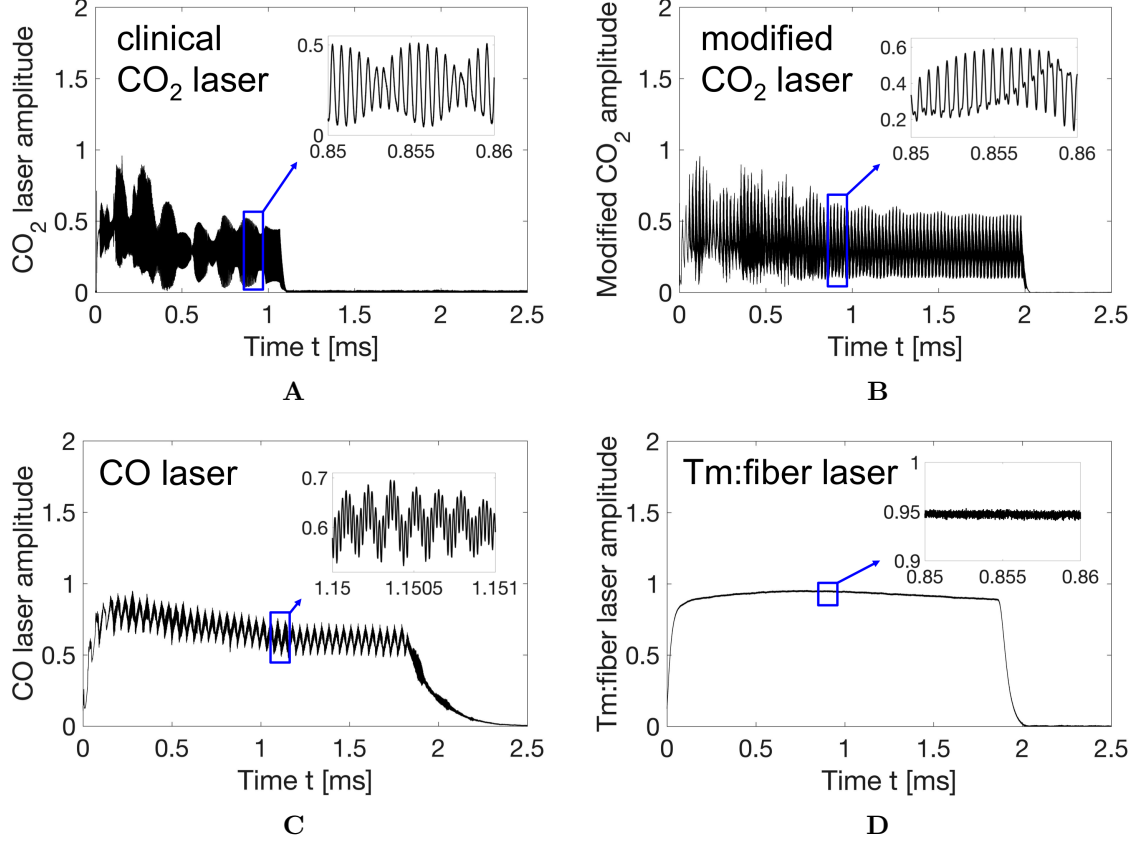


Figure 12. Laser pulse temporal profiles recorded at 115 mJ pulse energy using a photoelectric infrared detector (PEM-10.6, Vigo System S.A., Ozarow Mazowiecki, Poland). The maximum amplitude is normalized to 1. The zoom in shows microoscillations of the CO₂ lasers (2 MHz repetition frequency and 220 ns FWHM-micropulses) and the CO laser (6.5 MHz repetition frequency and 90 ns FWHM-micropulses). The Tm:fiber laser has no microstructure. **A:** Clinical CO₂ laser system. **B:** Modified CO₂ laser system with pulse width modulation. **C:** CO laser. **D:** Tm:fiber laser.

The laser pulses reaching the skin surface were monitored by repetitive measurements of pulse energy and temporal profile using a thermal sensor head (10A, Ophir Optonics Ltd., Jerusalem, Israel) and a photoelectric infrared detector (PEM-10.6, Vigo System S.A., Ozarow Mazowiecki, Poland). The rise and fall time (response time) of the photoelectric sensor is $\leq 0.5 \text{ ns}$. The temporal pulse structures of the different lasers were measured by the photoelectric sensor with high temporal resolution as shown in **Figure 12** and as described in **Section 3.1**. Based on the high repetition rates of the micropulses of the CO₂ lasers and the CO laser, 2 ms macropulses comparable to the Tm:fiber laser pulses were anticipated. The laser parameters of the different laser systems are summarized in **Table 2**.

Table 2. System Specifications of CO₂ Lasers, CO Laser, and Tm:Fiber Laser

Laser parameter	CO ₂	CO	Tm:fiber
wavelength λ [nm]	10600	5500 \pm 275	1940
absorption coefficient μ_a [cm ⁻¹]	630	193.2	79.8
optical penetration depth δ [μ m]	15.9	51.8	125.3
output power P [W]	70 (95)	100	120
beam diameter $2w_0$ [μ m]	120	113 ((54))	108
pulse width τ_p [ms]	2 (0.09-2)	2	2
pulse energy E_p [mJ]	20-132 (7-184)	11-200	80-212
radiant exposure H_0 [J/cm ²]	177-1168 (62-1628)	110-1995	874-2315
Rayleigh range z_R [mm]	0.82	1.34 ((0.19))	3.37
beam quality factor M^2	≤ 1.3	≤ 1.35 ((2.2))	≤ 1.4

() refers to the clinical CO₂ laser system

(()) refers to the small spot CO laser beam described in **Section 3.2.2**

Absorption coefficients and optical penetration depths are modified assuming 70% water content in skin

A relaxation oscillation occurs during the transient period when a cw laser is turning on. The laser intensity oscillates, typically in a damped harmonic manner, and rapidly reaches a steady-state intensity. When a laser is repetitively pumped or pumped with a modulated excitation source these relaxation oscillations are repeatedly excited and can be observed as microoscillations in the laser intensity. Both CO₂ lasers and the CO laser are RF-excited waveguide gas devices that clearly show relaxation oscillation in their macropulses, at 2 MHz and 6.5 MHz frequency, respectively. The CO laser intensity is also modulated at a RF excitation frequency of 45 MHz.

The diode-laser-pumped Tm:fiber laser has no evidence of relaxation oscillations because the diode laser pumping is turned on slowly as evidenced by the 100 μ s turn-on time. Also, this laser turns off just as quickly and smoothly. The CO₂ laser systems have a turn-off time of approximately 100 μ s, while the CO laser even takes 500 μ s. The relaxation time in the energy transfer processes between the gas molecules (laser and buffer molecules) that pump the excited state of the lasing molecules is primarily responsible for the different turn-off times of the CO₂ and CO lasers.

3.2.2 Spatial Beam Profile

The output power of the CO laser will decrease by about 10% caused by absorption of CO laser light in atmospheric air if the beam transport system is not purged with nitrogen gas. The laser power measurements were performed using a thermal sensor head (10A, Ophir Optonics Ltd., Jerusalem, Israel). Further, the CO laser beam spatial profile will be slightly distorted without gas purging as detected by thermal camera imaging (**Figure 13**) [45].

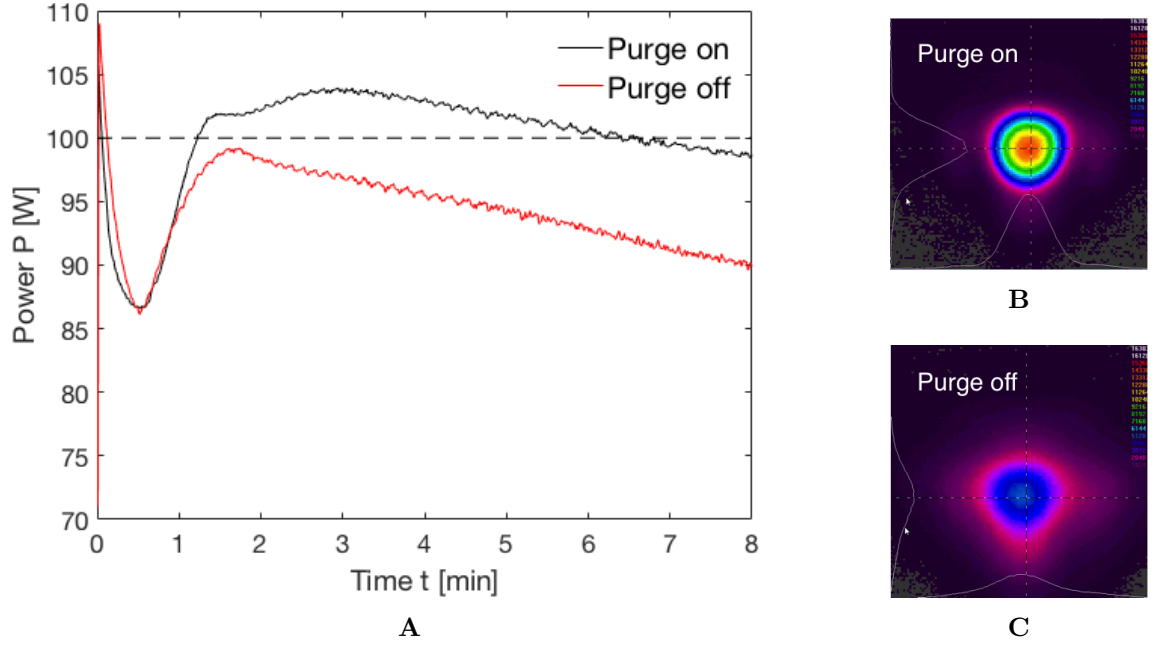


Figure 13. Nitrogen gas purging of the CO laser beam delivery to reduce atmospheric water absorption. **A:** The CO laser emission was enabled at $t = 0$. Laser power measurements using a thermal sensor head (10A, Ophir Optonics Ltd., Jerusalem, Israel) were performed with gas purge switched on and off. **B:** Beam spatial profile with purge switched on [45]. **C:** Beam spatial profile with purge switched off [45].

We measured the focused beam radii of the different lasers using scanned knife-edge technique at multiple distances along the beam propagation path z as shown for the CO laser beam in **Figure 14** [49]. The transmitted power of the beam was assumed to be an error function of the knife-edge position, as the knife-edge was translated in a cross-section through the laser beam perpendicular to the beam propagation path. The derivative of the transmitted power measurements results in a radial beam profile of a Gaussian function. We made multiple $1/e^2$ beam radius measurements along the beam propagation path to determine the beam waist w_0 at the focal plane z_0 and the beam quality factor M^2 . The measured beam radii were fitted to **Equation 3**. The focused Gaussian laser beams of the different lasers have a calculated M^2 that ranges from 1.3 to 1.4. We built customized distance holders for each laser system to immobilize the tissue sample in the focal plane during the laser-tissue exposures.

In an additional experiment, we produced a $54 \mu\text{m}$ focal spot size with the CO laser. We used a compound lens that contains of a meniscus CaF_2 lens (LE5838, $f = 20 \text{ mm}$, Thorlabs Inc., Newton, NJ, USA) and a planoconvex CaF_2 lens (LA5315, $f = 20 \text{ mm}$, Thorlabs Inc., Newton, NJ, USA) separated by locking nuts to avoid lens surfaces to touch one another. The Rayleigh length z_R is determined by the beam waist radius w_0 , the wavelength λ , and the beam quality factor M^2 (**Equation 4**). Thus, the Rayleigh range decreases from 1.34 mm to $190 \mu\text{m}$ if the focal spot size $2w_0$ of the CO laser is reduced from $113 \mu\text{m}$ to $54 \mu\text{m}$, as the M^2 also increases from 1.35 to 2.2 (**Figure 14.D**).

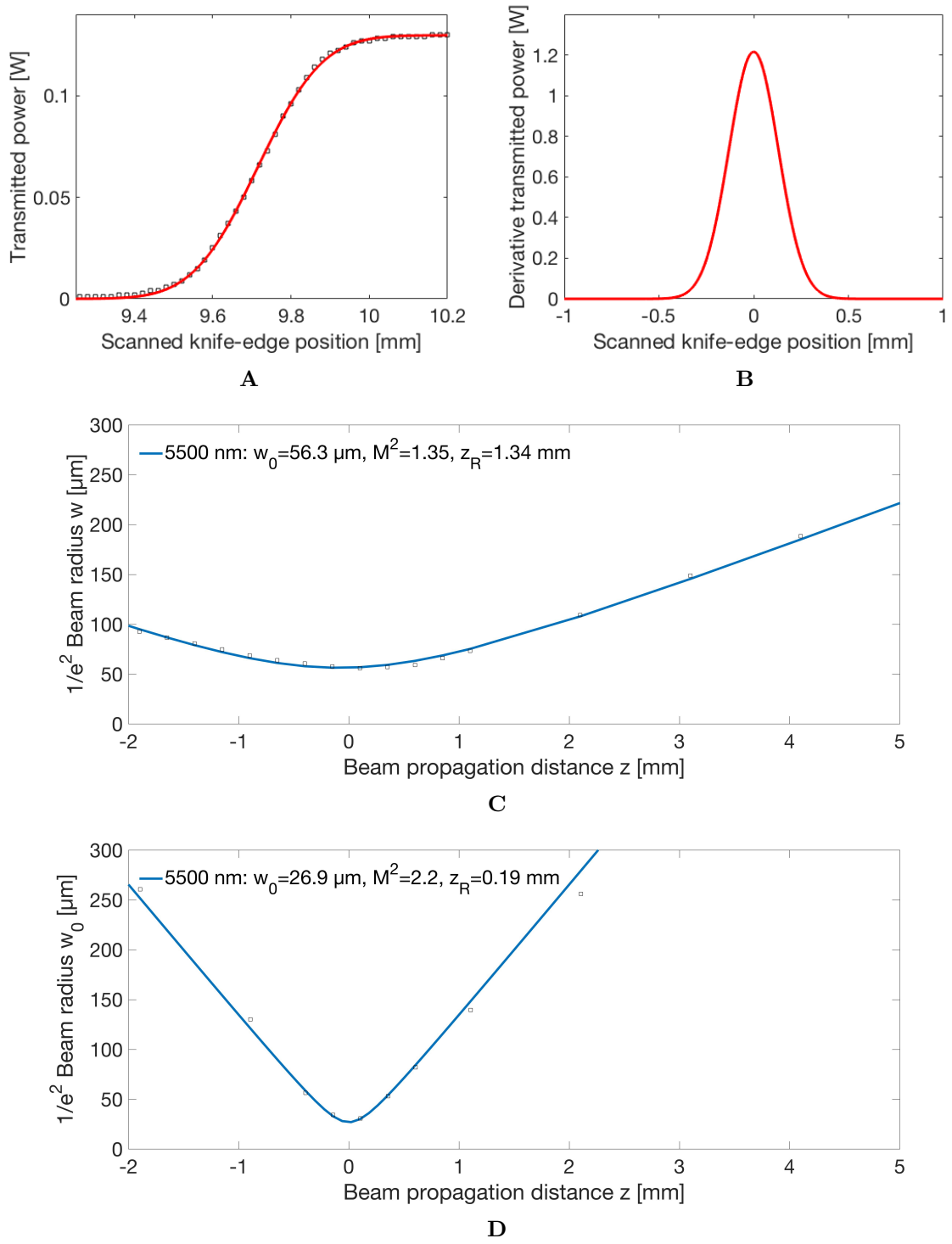


Figure 14. The spatial distribution of the 113 and 54 μm spot size CO laser beam was sampled in a plane perpendicular to the beam propagation path z using the knife-edge technique [49]. **A:** The transmitted power was measured as an error function behind the knife-edge, as the knife-edge is scanned through the beam. **B:** The Gaussian beam profile is plotted as the derivative of the transmitted power measurements. The spatial beam profile gives a $1/e^2$ focused beam diameter. Multiple beam-size measurements were made along the beam propagation path to determine the beam waist $2w_0$, the focal plane, the beam propagation parameter M^2 , and the Rayleigh range z_R . **C:** The CO laser beam was focused to a 113 μm spot size and **D:** to a 54 μm spot size.

A 190 μm Rayleigh range is very short, however, a comparable spot size with a CO_2 laser will even produce half of the Rayleigh range as the wavelength is two times longer. The beam characteristics of the different lasers are also summarized in **Table 2**.

3.3 Experimental Setup

The clinical and the modified CO_2 laser systems shared the same hardware (**Figure 8**). Single laser pulses were delivered through the scanning handpiece. Treatment parameters such as pulse energy, scan area, coverage, and scan rate were adjusted via user control panel.

The RF power supply of the CO laser was controlled with an electronic interface for setting of laser power and external pulse modulation. The CO laser beam was delivered in a nitrogen purged tube to avoid atmospheric water absorption (**Figure 9 and 15**).

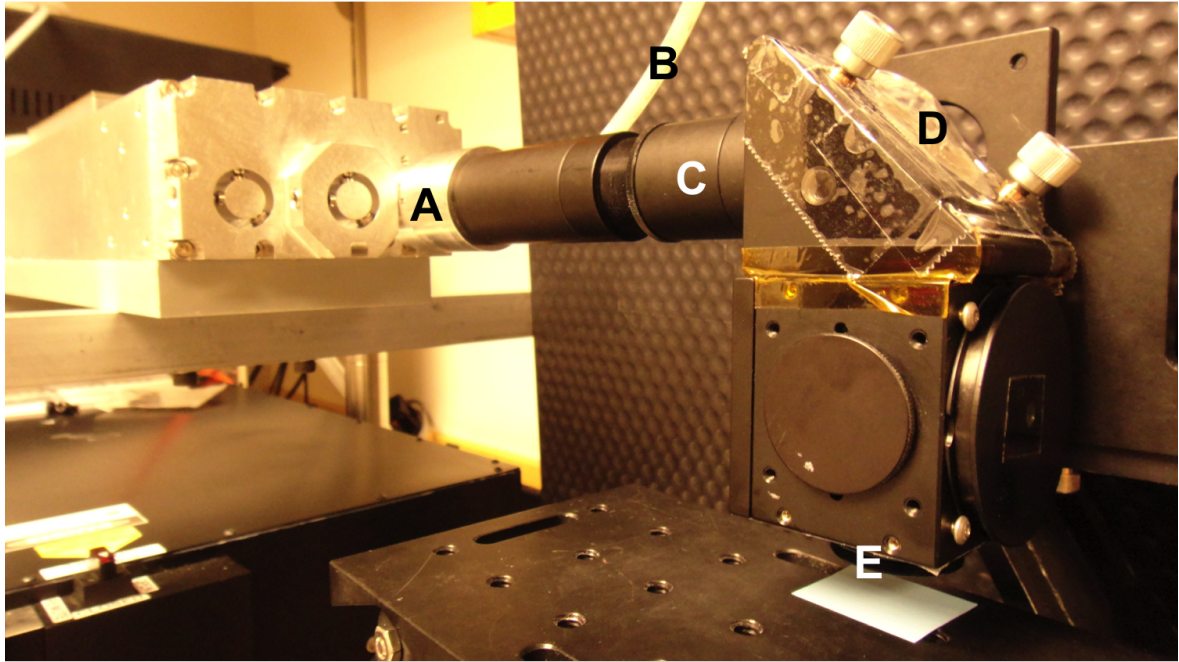


Figure 15. 5500 nm CO laser (GEM-100™, Coherent Inc., Santa Clara, CA, USA). **A:** CO laser output. **B:** Inlet for the nitrogen gas hose. **C:** Nitrogen purged tube for beam delivery. **D:** Reflecting mirror. **E:** Biconvex 25.4 mm focal length CaF_2 lens.

The Tm:fiber laser has an optical fiber output connected to a fixed collimator and an extension tube (**Figure 11 and 16**). We used a remote hand-held interface to set the power level and to enable external pulse modulation. Exposure parameters such as focal beam diameter, pulse energy, and pulse duration were checked prior to irradiation. The laser systems along with the exposure parameters are listed in **Table 2**.

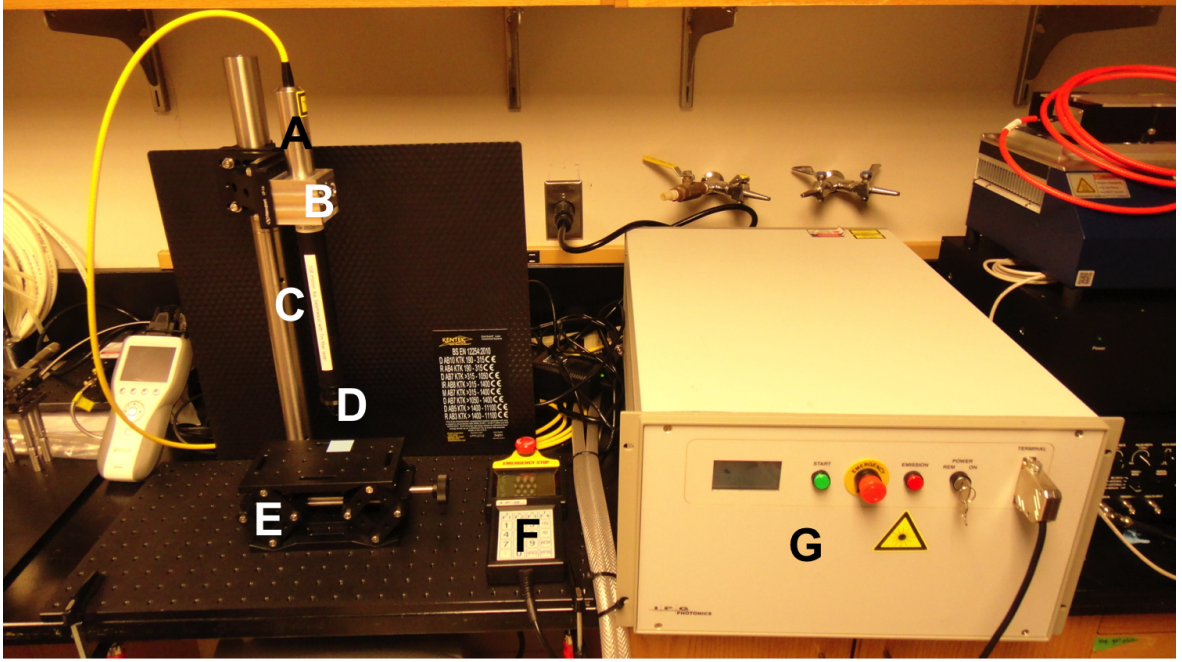


Figure 16. 1940 nm Tm:fiber laser (TLR-120-1940, IPG Photonics Corporation, Birmingham, AL, USA). **A:** Tm:fiber laser output. **B:** Metal block. **C:** Extension tube. **D:** Planoconvex 254 mm focal length ZnSe lens. **E:** Translation stage. **F:** Remote hand-held interface. **G:** Laser module with front panel for power level setting and external pulse modulation.

3.4 Laser-Tissue Exposures

Full-thickness human skin was collected from abdominoplasty as a waste product with approval by the Massachusetts General Hospital Institutional Review Board. The tissue used in these experiments were excess tissue with no related patient information. The fresh skin samples were cleaned of subcutaneous fat and hair and stored at -80°C . 1.5-2.0 hours prior to the laser irradiation, the skin samples were defrosted. The optical and thermal properties of skin can dynamically change depending on the condition of the tissue [59]. Thus, the skin samples were covered under gauze bandages soaked with phosphate-buffered saline (PBS) in order to avoid dehydration, as tissue water is the target absorber for ablation.

The initial temperature of the skin surface was measured using an infrared camera A655sc (FLIR Systems, Inc., Wilsonville, OR, USA) that produced thermal images of 640×480 pixels resolution. The skin surface had an initial temperature of $20\text{-}21^{\circ}\text{C}$. The skin samples were immobilized on a flat ground to avoid any wrinkling of the skin surface. We carefully adjusted the tissue in focal plane by the use of a three-dimensional translation stage and custom-built distance holders to maintain the same beam diameters. We delivered single pulses with varying energies from about 10 mJ to 200 mJ and 2 ms pulse length to compare the energy-dependent ablation depths and the thermal damage zones of the different lasers. A total of 6 single exposures were conducted on different skin areas for each set of laser parameters. Each skin sample contained 3 linearly aligned exposures. The exposure was repeated under the same laser setting after translation of the skin sample by 2-3 mm in distance. The laser

exposed tissue was processed according to the flowchart in **Figure 17**.

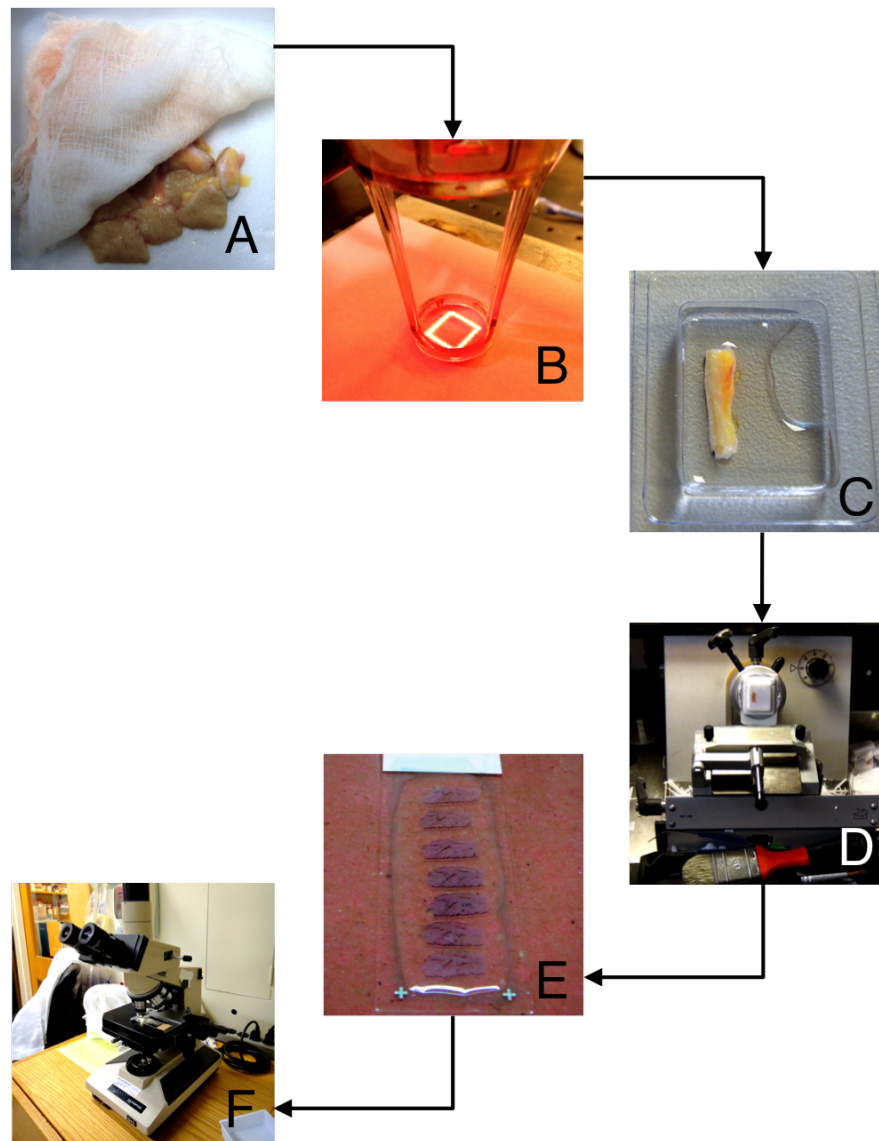


Figure 17. Histological processing routine. **A:** Preparation of human skin samples. **B:** Laser irradiation of skin samples. **C:** Embedding in optimal cutting temperature compound (OCT). **D:** Cryostat sectioning. **E:** Staining with nitro blue tetrazolium chloride (NBTC). **F:** Assessment of the laser-tissue effects using light microscopy.

The freshly dissected tissue lesions were embedded in frozen optimal cutting temperature compound (OCT). After embedding, 20 μm thick vertical cryosections of the laser-tissue effects were obtained. The cryosections were mounted on glass slides and were stained with nitro blue tetrazolium chloride (NBTC). The NBTC stain enables the differentiation between blue-stained viable cells and unstained thermally damaged cells. After 24 hours the stained slides were rinsed with distilled water, dipped in 70% ethanol, 12 times in 95% ethanol, 12 times in 100% ethanol, in xylene, and were then fixed with histological mounting medium under a glass coverslip.

3.5 Histological Evaluation of Etch Depth and Thermal Damage

The sections obtained from histology were imaged using Nanozoomer RS Digital Pathology System (Olympus America Inc., Melville, NY, USA) that has a scanning resolution of 0.23 $\mu\text{m}/\text{pixel}$. We used the NPD.view software (Hamamatsu Photonics, Hamamatsu City, Japan) to measure the dimensions of the ablation craters and the thermal damage zones (**Figure 18**). In a few cases, the boundary of the thermal damage zones was extrapolated, as the crater walls were folded or ripped due to the histological processing. If necessary, the unstained thermally damaged tissue zones were encircled with black lines using ImageJ (1.49 v, National Institutes of Health, Bethesda, MD, USA).

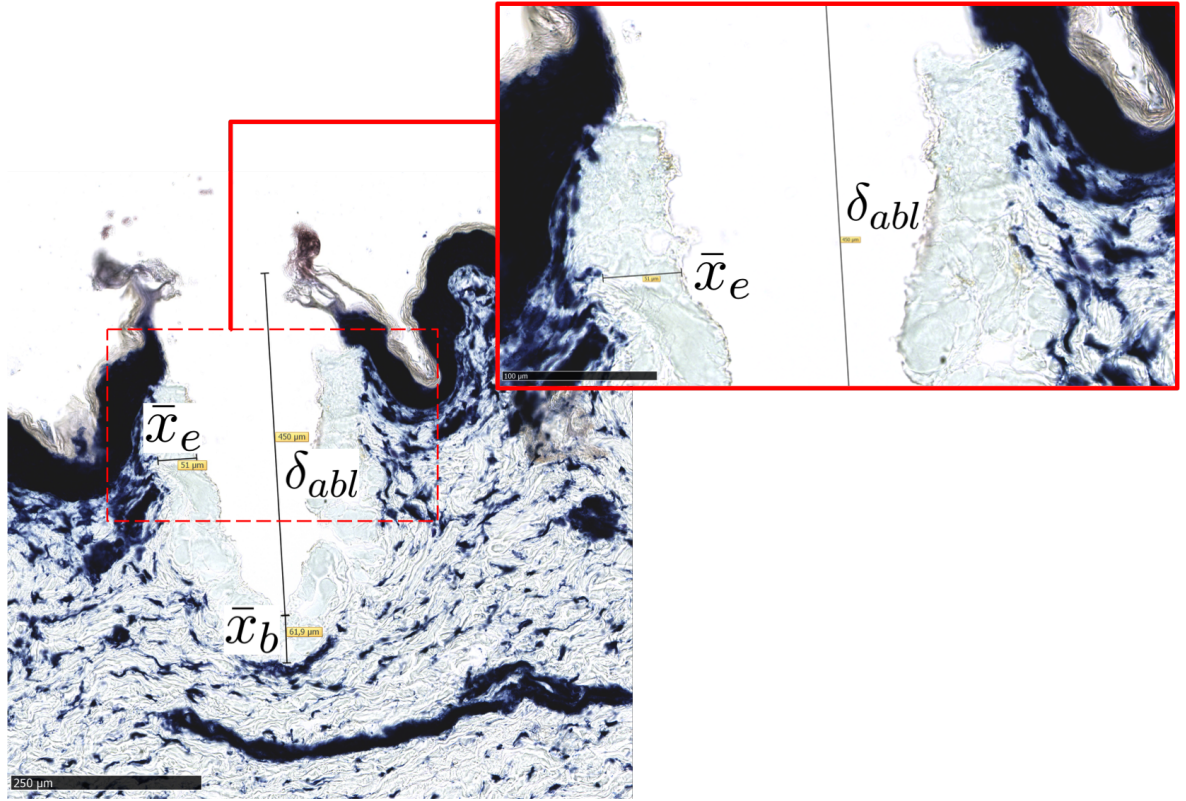


Figure 18. The etch depth δ_{abl} and the thermal damage zones \bar{x}_b , \bar{x}_e of the ablation craters were measured using the NPD.view software (Hamamatsu Photonics, Hamamatsu City, Japan).

The etch depth δ_{abl} of the ablation crater was defined as the maximum measured depth of all vertical sections acquired from the ablation crater. The mean lateral thermal injury \bar{x}_e was defined as the thickness of unstained, thermally damaged tissue at the ablation crater edges located at 50% of the etch depth. The mean residual thermal injury \bar{x}_b was defined as the thickness of unstained, thermally damaged tissue at the bottom layer of the ablation crater. The thermal damage zone is anticipated to follow the Beer's law according to **Equation 6**. Sometimes the embedded tissue sample can be squeezed or tilted during the histological processing routine (**Figure 19**).

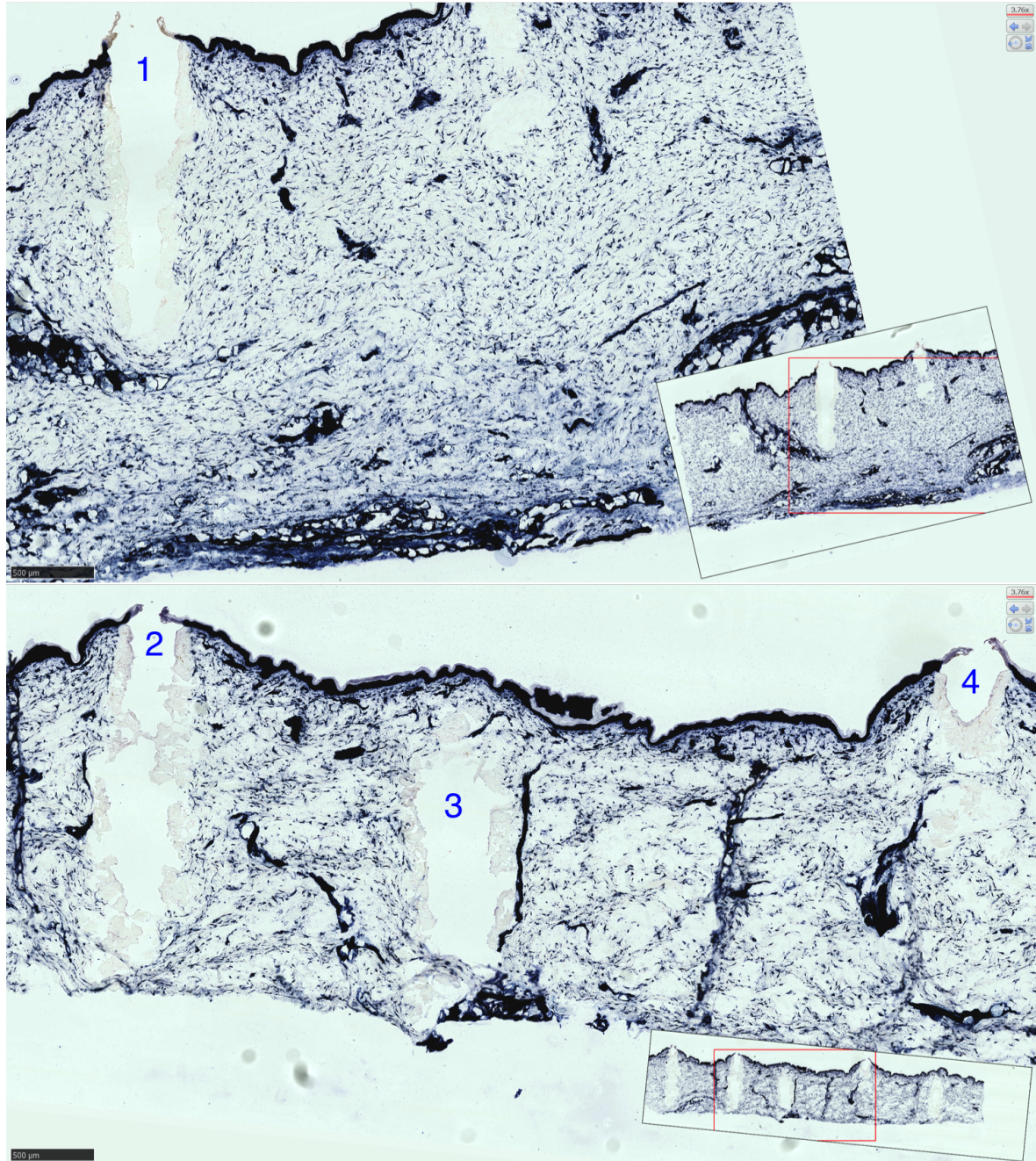


Figure 19. The NPD.view software (Hamamatsu Photonics, Hamamatsu City, Japan) was used for histological analysis of the laser-tissue effects imaged with Nanozoomer RS Digital Pathology System (Olympus America Inc., Melville, NY, USA). (1) Good tissue slice with minimal folding inwards of the ablation crater walls, (2) squeezed ablation crater, upper part (3) and bottom part (4) of the ablation crater were not in the cutting plane.

So that the sectioning of the tissue might not cover the ablation channel in its full depth. The tissue slices that were obviously tilted were excluded from the measurements. Irregularities in the thickness of the thermal damage zones caused by the ablation process, the collagen shrinkage, and artifacts from the histological processing made the measurements more difficult. The thermal damage zones were averaged over 10 sections. We anticipated that the

maximum measured etch depth and the mean values of the thermal damage zones are an acceptable approximation.

The data from the etch depth measurements was subjected to curve fitting in Matlab (R2016b, The MathWorks, Natick, MA, USA). The ablation-to-coagulation-ratio (ACR) was then calculated by dividing the etch depth δ_{abl} by the mean residual thermal injury \bar{x}_b at the bottom of the ablation crater as follows [3]

$$ACR = \delta_{abl} / \bar{x}_b. \quad (16)$$

3.6 Numerical Simulation of Heat Transfer and Tissue Ablation in Skin

We aimed to develop a simple laser-tissue ablation model by using COMSOL Multiphysics 5.3 (COMSOL Multiphysics, Stockholm, Sweden) to predict the ablation depth and the thermal damage zone based on the laser-induced temperature distribution. The finite element method (FEM) is a numerical approach that can be used to analyze the bioheat transfer in tissue [16, 37]. The heat transfer module considers four mechanisms, which are conduction, convection, radiation, and sublimation. We generated a three-layered model to represent the skin tissue geometry. The graphical user interface in COMSOL is shown in **Figure 20**.

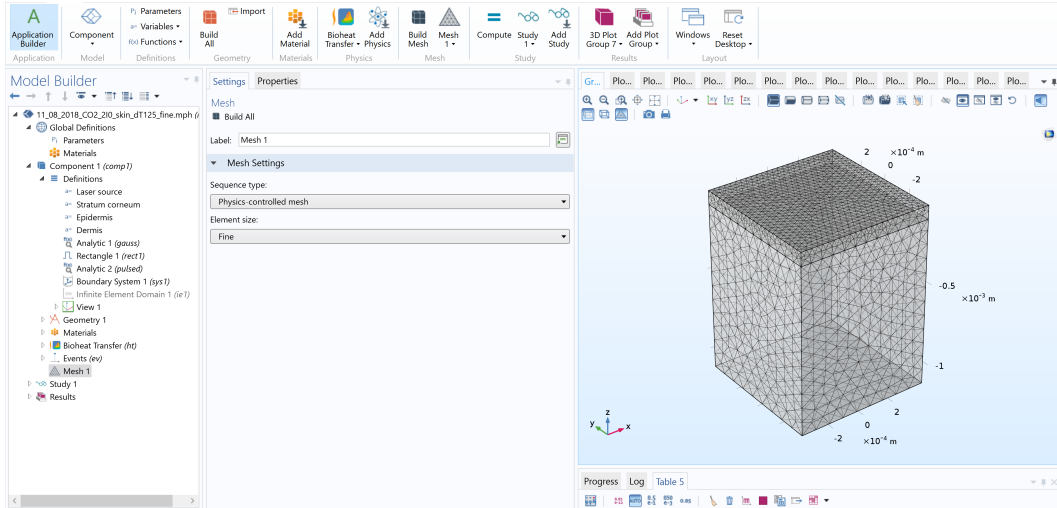


Figure 20. Graphical user interface in COMSOL Multiphysics 5.3 (COMSOL Multiphysics, Stockholm, Sweden).

Here, we used flat and homogeneous skin layers. Each layer is divided into a finite element mesh so that partial differential equations can be numerically solved. The solution is approximated in each element. In this model the skin was treated as a solid material with no blood flow and was studied using the FEM solver. The numerical solutions obtained by FEM after a single 2 ms laser pulse was compared with the experimentally acquired data from histology.

We used the same exposure parameters, such as wavelength, spot size, radiant exposure, and pulse length, to define the global parameters of the laser heat source.

3.6.1 Skin Geometry

A three-dimensional skin model (x, y, z) anticipating three layers, namely stratum corneum, epidermis, and dermis, was built using fine meshed domains. The depth in tissue is denoted by the spatial variable z . The surface area (x, y) of the meshed tissue geometry is $0.8 \text{ mm} \times 0.8 \text{ mm}$. The total thickness of the geometry mesh is $1.1\text{-}1.7 \text{ mm}$. The meshed skin model is shown in **Figure 20**. In this study, we assumed an isotropic material, which has the same material properties in all directions within a domain.

3.6.2 Heat Source

The heat source Q_{laser} was described as a spatial Gaussian laser beam profile

$$Q_{laser} = I_0 a \exp(a z - 2(x^2 + y^2)/\sigma^2), \quad (17)$$

where I_0 is the peak irradiance. The width of irradiated region σ was adjusted to 0.06 mm , which is equal to a spot size of $120 \text{ }\mu\text{m}$ as used in the experiments. The laser absorption in tissue was modeled as an exponential decay using Beer's law (**Equation 6**), where a is the absorption coefficient of each skin layer based on its anticipated water content (10% in stratum corneum, 20% in epidermis, 70% in dermis) (**Table 3**).

Table 3. Material Properties of the Skin Domains.

Phase 1	λ [nm]	a [cm^{-1}]	ϱ [kg/m^3]	k [$\text{W}/(\text{mK})$]	c_v [$\text{J}/(\text{kgK})$]
stratum corneum	10600	90	1500	0.235	3600
	5500	27.6	1500	0.235	3600
	1940	11.4	1500	0.235	3600
epidermis	10600	180	1190	0.235	3600
	5500	55.2	1190	0.235	3600
	1940	22.8	1190	0.235	3600
dermis	10600	630	1116	0.445	3300
	5500	193.2	1116	0.445	3300
	1940	79.8	1116	0.445	3300
Phase 2	λ [nm]	a [cm^{-1}]	ϱ [kg/m^3]	k [$\text{W}/(\text{mK})$]	c_v [$\text{J}/(\text{kgK})$]
ablated material	all	0	10^{-9}	0.1	10^9

λ : wavelength, a : modified water absorption coefficient, ϱ : density, k : thermal conductivity, c_v : specific heat capacity

The absorption coefficient is 0 once the tissue is entirely vaporized, as ablated tissue does not absorb any laser light. We defined the material properties (absorption coefficient a , density ρ , thermal conductivity k , specific heat capacity c_v) of each skin layer as phase 1 and ablated material as phase 2 (with values from **Table 1** and **Figure 4**). Furthermore, we simulated ablated material in phase 2 by defining a large heat capacity and a small density and small thermal conductivity.

3.6.3 Laser Pulse

Temporal shape and length of the laser pulse were expressed in the function $pulsed(t)$. It is a rectangle function with a transition zone of 10^{-4} ms and a pulse duration of 2 ms. In this model, we did not simulate any microstructures or oscillations. The $pulsed(t)$ -function is shown in **Figure 21**. The pulsed laser irradiation was simulated with $Q_{laser} * pulsed(t)$.

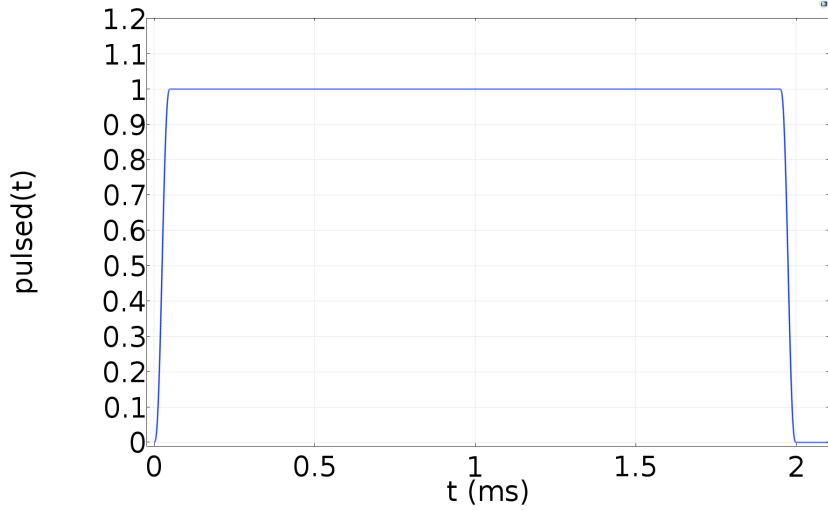


Figure 21. The temporal pulse shape was generated by $pulsed(t)$, which is a rectangle function implemented in COMSOL Multiphysics 5.3 (COMSOL Multiphysics, Stockholm, Sweden).

3.6.4 Bioheat Transfer with Phase Change

In this section, the equations implemented for the bioheat transfer module (ht) in COMSOL Multiphysics will be described [21]. The resulting temperature distribution T of the entire domain is obtained by time-dependent solving the bioheat transfer equation with phase change expressed as follows

$$\rho c_v \frac{\partial T}{\partial t} + \rho c_v u \cdot \nabla T + \nabla \cdot q = Q, \quad (18)$$

where Q contains the heat source, ρ is the density, c_v is the specific heat capacity, u is the velocity vector, and the heat flux by conduction is $q = -k \nabla T$. The conductive heat flux is proportional to the temperature gradient, where k is the thermal conductivity

$$k = \theta k_{phase1} + (1 - \theta) k_{phase2} \quad (19)$$

and θ is the phase that will be described in the next section.

3.6.5 Simulation of Tissue Ablation

A phase transition will simulate the ablation of tissue. The phase change between skin as phase 1 and ablated material as phase 2 will occur at an ablation temperature T_{ablate} of 300°C (573.15 K). It is assumed that the phase transformation takes place in a temperature interval of $T_{ablate} - dT/2$ and $T_{ablate} + dT/2$, where the transition interval is dT . This means, the material properties in **Table 3** defined for phase 1 are valid for $T < T_{ablate}$ and material properties defined for phase 2 are applied for $T > T_{ablate}$. Here, θ represents the phase and is initialized to 1 before $T < T_{ablate}$ and to 0 after $T > T_{ablate}$.

The incident laser light is only absorbed by the skin tissue during phase 1 according to a_{phase1} , as the absorption coefficient a_{phase2} of phase 2 is set to 0 cm^{-1}

$$a = \theta a_{phase1} + (1 - \theta) a_{phase2}. \quad (20)$$

We have simulated material removal by changing the material properties dependent on temperature and phase. Thus, the density ϱ is defined by ϱ_{phase1} and ϱ_{phase2}

$$\varrho = \theta \varrho_{phase1} + (1 - \theta) \varrho_{phase2}. \quad (21)$$

If the local material properties have adopted the density of phase 2 ϱ_{phase2} , the phase change has been completed. The specific heat capacity at constant pressure is denoted by c_v and is based on $c_{v,phase1}$ and $c_{v,phase2}$

$$c_v = \frac{1}{\varrho} (\theta \varrho_{phase1} c_{v,phase1} + (1 - \theta) \varrho_{phase2} c_{v,phase2}) + L \frac{\partial \alpha_m}{\partial T}. \quad (22)$$

In order to model the removal of heated material, Radice et al. have used a variable specific heat capacity that becomes significantly larger after phase transition [39]. We have similarly set the specific heat capacity of phase 2 $c_{v,phase2}$ to 10^9 J/(kgK) . The specific heat capacity describes the amount of heat required to raise the temperature of one unit mass of a substance by one degree. We simulated the removal of hot vaporized tissue from the ablation site by artificially increasing the value of $c_{v,phase2}$.

As dermal skin contains 70% tissue water, 70% of the latent heat of water vaporization $L_v = 2257 \text{ J/kg}$ was used as the required energy to vaporize tissue. The distribution of latent heat is expressed by $L \partial \alpha_m / \partial T$ in **Equation 22**, where the fraction of mass α_m

$$\alpha_m = 0.5 \frac{(1 - \theta)\rho_{phase2} - \theta\rho_{phase1}}{\rho} \quad (23)$$

is equal to -0.5 before $T < T_{ablate}$ and to 0.5 after $T > T_{ablate}$.

The initial temperature T_0 of skin is assumed to be equal to the external room temperature $T_{ext} = 21^\circ\text{C}$ (294.15 K). The surface layer of the skin model is subjected to convective heat flux q_0

$$q_0 = h_{conv}(T_{ext} - T), \quad (24)$$

where the heat transfer coefficient h_{conv} is adjusted to 10 W/(m²K) in phase 2. There will be no heat flux during phase 1. The remaining external boundaries of the tissue geometry are set to T_{ext} (**Table 4**).

Table 4. Global Parameters Used for Model Geometry and Heat Transfer Simulation.

Parameter	Value	Description
x_{probe}	0.8 mm	size of probe
z_{sc}	0.02 mm	thickness of stratum corneum
$z_{epidermis}$	0.08 mm	thickness of epidermis
z_{dermis}	1 mm - 1.6 mm	thickness of dermis
σ	0.06 mm	width of irradiated region
T_0	21°C (294.15 K)	initial temperature of probe
T_{ext}	21°C (294.15 K)	external temperature
T_{ablate}	300°C (573.15 K)	ablation temperature
L_v	$0.7 \times 2257 \text{ J/g}$	70% of latent heat of water vaporization

4 Results

The measurements of the maximum etch depths, the mean thermal damage zones, and the calculation of the ablation-to-coagulation-ratio (ACR) obtained from histology will be presented. Typical examples of the laser-tissue effects will be shown as histology sections. Basic ablation models, such as Hibst model, blow-off model, and steady-state model, were applied to the histology data. In addition, results from a numerical simulation of the laser-tissue ablation will be compared to the histology results.

4.1 Etch Depth

The effect of pulse energy and absorption coefficient on the ablation depth was analyzed. In the following experiments, a comparable spot size of 108-120 μm and a pulse duration of 2 ms were used. The ablation channels generated by the CO laser and the Tm:fiber laser were compared to those of the modified CO₂ laser system at 109-126 mJ pulse energy (**Figure 22.A**) and to the clinical CO₂ laser system 184-195 mJ pulse energy (**Figure 22.B**).

Remarkably, there was no tissue ablation after 2 ms Tm:fiber laser irradiation for pulse energies below 80 mJ with a spot size of 108 μm . Even at higher pulse energies, the ablation craters remained very superficial in contrast to the laser-tissue effects produced by the CO₂ laser systems and the CO laser. The thermal relaxation time is 109.4 ms so that the exposure time of the Tm:fiber laser could be increased to obtain higher etch depths.

Up to a pulse energy of 50 mJ, the ablation channels of the CO laser and the modified CO₂ laser system were comparable in depth. At pulse energies above 50 mJ, the CO₂ laser system increasingly exhibited higher ablation depths. The thermal relaxation time is limited to 1.8 ms for CO₂ laser applications, whereas it is 18.7 ms for the CO laser also allowing longer exposure times.

As expected, the ablation depth increases with higher radiant exposure and with higher absorption coefficient if one compares the ablation results at the same radiant exposures. Thus, the CO₂ lasers exhibited the highest ablation depths with a spot size of 120 μm . But it is a better approach to compare the ablation results at radiant exposures normalized to the ablation threshold, which will be shown in **Section 4.2**. The histology results are summarized in **Table 5**. The results from the clinical CO₂ laser system, where the pulse duration automatically changes with pulse energy are separately shown in **Table 6**.

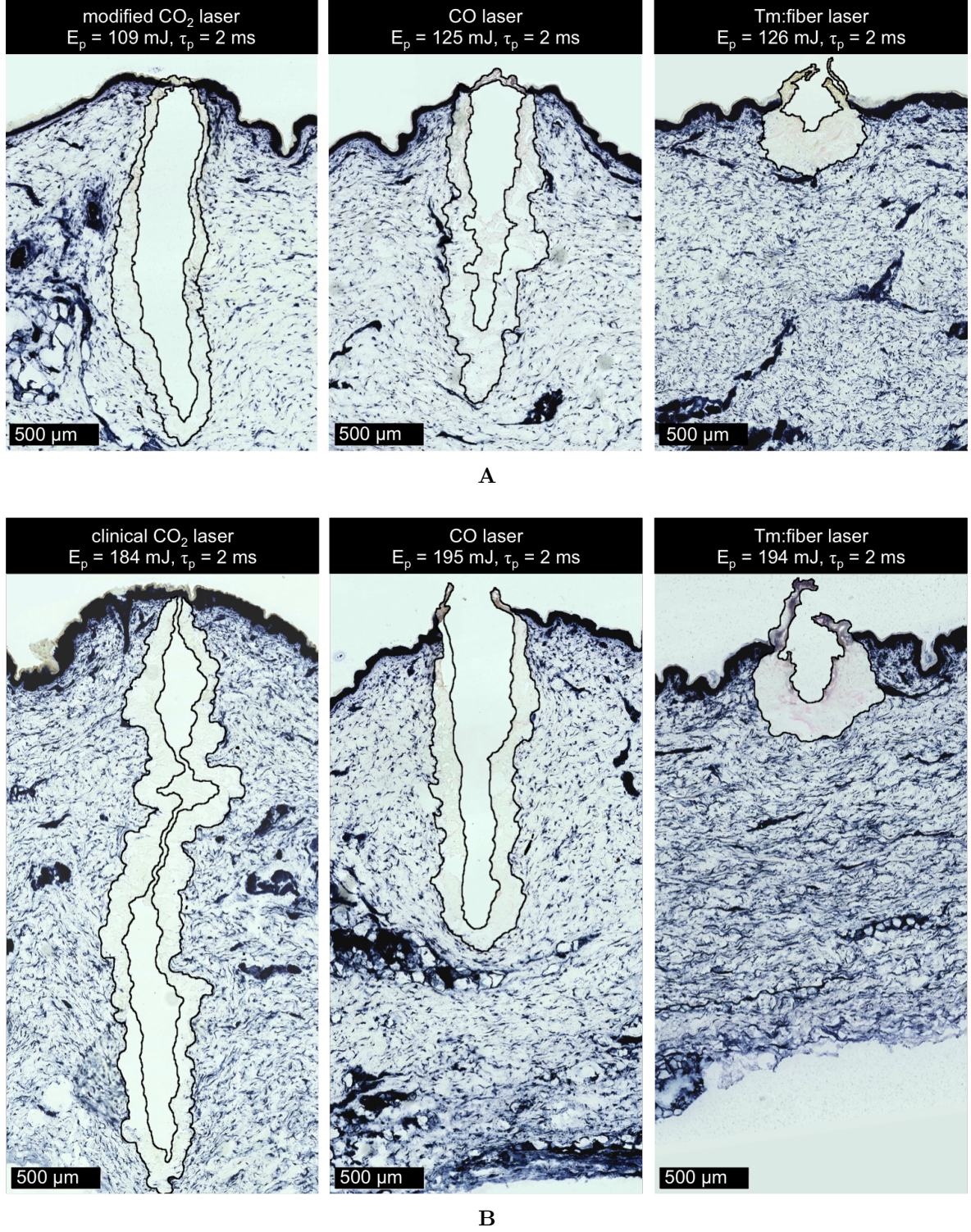


Figure 22. Laser-tissue effects produced by 2 ms pulses, 108-120 μm spot sizes, and energies of 109-126 mJ and 184-195 mJ. Thermal damage zones are not NBTC-stained and marked with black lines. Etch depth δ_{abl} , thermal damage at the bottom \bar{x}_b and at the edges \bar{x}_e of the ablation crater were measured. **A:** Modified CO₂ laser at 109 mJ ($\delta_{abl} = 1.8 \text{ mm}$, $\bar{x}_b = 0.10 \text{ mm}$, $\bar{x}_e = 0.08 \text{ mm}$) was compared to CO laser at 125 mJ ($\delta_{abl} = 1.38 \text{ mm}$, $\bar{x}_b = 0.17 \text{ mm}$, $\bar{x}_e = 0.12 \text{ mm}$) and Tm:fiber laser at 126 mJ ($\delta_{abl} = 0.25 \text{ mm}$, $\bar{x}_b = 0.23 \text{ mm}$, $\bar{x}_e = 0.34 \text{ mm}$). **B:** Clinical CO₂ laser at 184 mJ ($\delta_{abl} = 3 \text{ mm}$, $\bar{x}_b = 0.12 \text{ mm}$, $\bar{x}_e = 0.10 \text{ mm}$) was compared to CO laser at 195 mJ ($\delta_{abl} = 1.98 \text{ mm}$, $\bar{x}_b = 0.16 \text{ mm}$, $\bar{x}_e = 0.16 \text{ mm}$) and Tm:fiber laser at 194 mJ ($\delta_{abl} = 0.35 \text{ mm}$, $\bar{x}_b = 0.23 \text{ mm}$, $\bar{x}_e = 0.24 \text{ mm}$).

Table 5. Ablation Depth δ_{abl} and Thermal Damage Zones \bar{x}_e and \bar{x}_b of the Laser-Tissue Effects in the Histology: A Comparison of Modified CO₂ Laser System, CO Laser, and Tm:Fiber Laser.

λ [nm]	Exposure Parameters			Tissue Parameters		Histology Results		
	E_p [mJ]	H_0 [J/cm ²]	τ_p [ms]	τ_{tc} [ms]	μ_a [cm ⁻¹]	δ_{abl} [mm]	\bar{x}_e [mm]	\bar{x}_b [mm]
10600 (mod.)	20	177				0.45	0.04	0.05
	43	380				1.00	0.04	0.05
	70	619				1.35	0.06	0.06
	85	752	2*	1.8	630	1.63	0.08	0.08
	109	964				1.80	0.08	0.10
	117	1035				1.93	0.12	0.14
	132	1168				2.10	0.11	0.12
5500	11	110				0.18	0.06	0.06
	19	190				0.33	0.06	0.11
	30	299				0.48	0.07	0.10
	40	399				0.75	0.08	0.09
	50	499				0.88	0.10	0.12
	80	798	2	18.7	193.2	1.25	0.12	0.12
	125	1247				1.38	0.12	0.17
	164	1636				1.75	0.12	0.14
	185	1846				1.85	0.14	0.15
	195	1945				1.98	0.16	0.16
1940	200	1995				2.00	0.15	0.21
	80	874				0.13	0.20	0.21
	101	1103				0.20	0.24	0.23
	126	1376				0.25	0.34	0.23
	157	1715	2	109.4	79.8	0.30	0.19	0.25
	185	2021				0.33	0.27	0.24
	194	2119				0.35	0.24	0.23
	212	2315				0.38	0.29	0.30

Exposure parameters: λ : wavelength, E_p : pulse energy, H_0 : radiant exposure, τ_p : pulse width

Tissue parameters: τ_{tc} : thermal diffusion time, μ_a : 70% water absorption coefficient

Histology results: δ_{abl} : etch depth, \bar{x}_e : mean thermal damage at crater edges, \bar{x}_b : at crater bottom

*thermal confinement condition $\tau_p < \tau_{tc}$ is not fulfilled

Table 6. Ablation Depth δ_{abl} and Thermal Damage Zones \bar{x}_e and \bar{x}_b of the Laser-Tissue Effects in the Histology: Clinical CO₂ Laser System With Different Pulse Duration τ_p .

λ [nm]	Exposure Parameters			Tissue Parameters		Histology Results		
	E_p [mJ]	H_0 [J/cm ²]	τ_p [ms]	τ_{tc} [ms]	μ_a [cm ⁻¹]	δ_{abl} [mm]	\bar{x}_e [mm]	\bar{x}_b [mm]
10600 (clin.)	7	62	0.09			0.45	0.04	0.06
	17	150	0.12			0.75	0.05	0.08
	25	221	0.16			1.00	0.04	0.08
	34	301	0.22			1.30	0.07	0.08
	43	380	0.29	1.8	630	1.40	0.06	0.06
	70	619	0.54			2.00	0.08	0.09
	109	964	0.96			2.40	0.09	0.09
	153	1354	1.48			2.75	0.09	0.15
	184	1628	2*			3.00	0.10	0.12

Exposure parameters: λ : wavelength, E_p : pulse energy, H_0 : radiant exposure, τ_p : pulse width

Tissue parameters: τ_{tc} : thermal diffusion time, μ_a : 70% water absorption coefficient

Histology results: δ_{abl} : etch depth, \bar{x}_e : mean thermal damage at crater edges, \bar{x}_b : at crater bottom

*thermal confinement condition $\tau_p < \tau_{tc}$ is not fulfilled

4.2 Basic Ablation Models

The etch depths δ_{abl} listed in **Table 5** are plotted against the incident radiant exposure H_0 in **Figure 23**. Further, it is interesting to analyze the etch depths in relation to the radiant exposure normalized to the ablation thresholds H_{th} because of the different absorption coefficients of the lasers in tissue. The ablation threshold is the interception of the extrapolated graph with the x-axis. The ablation threshold increases with higher optical penetration depth, which is defined as the reciprocal of the absorption coefficient. Interestingly, the CO laser produced higher etch depths than the modified CO₂ laser system at radiant exposures n -times higher than the ablation threshold. Due to the higher threshold of Tm:fiber laser ablation, there is no data available for $n \times H_{th}$ with $n > 5$.

We used Matlab to fit the etch depths determined from histology based on least squares algorithm. The fits in **Figure 23** were performed using the Hibst equation in **Equation 15**, where γ and μ_a are pure fit parameters. The plots are generated for the modified CO₂ laser ($R^2 = 0.9974$), the CO laser ($R^2 = 0.9878$), and the Tm:fiber laser ($R^2 = 0.9861$). It is clearly evident that the fitted absorption coefficients using the Hibst equation are much smaller compared to the water absorption coefficients expected in **Table 7**. This means that the Hibst model as a mathematical approach cannot realistically describe the ablation mechanisms for $\gamma \neq 0$ and $\gamma \neq 1$.

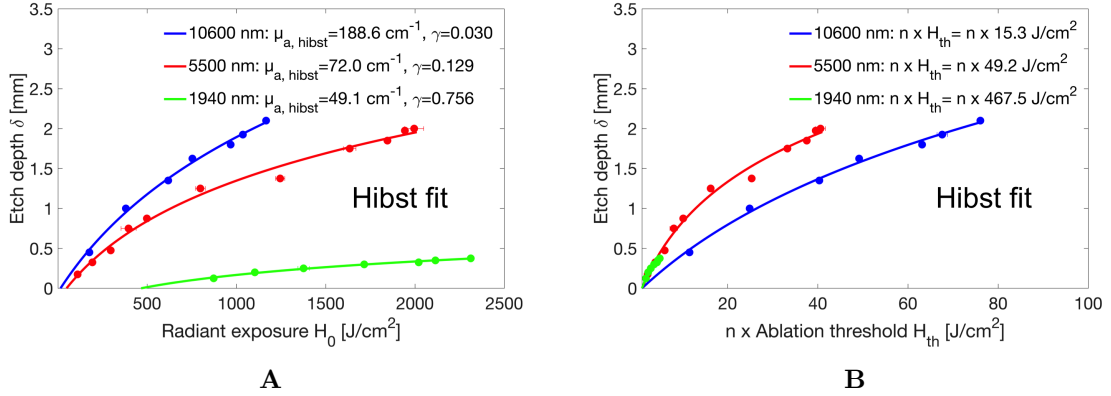


Figure 23. Hibst fit of the etch depth δ_{abl} vs. radiant exposure H_0 according to **Equation 15**. The fit parameters in the Hibst equation are the absorption coefficient μ_a and the parameter γ , which suggests steady-state ($\gamma \rightarrow 0$) or blow-off ($\gamma \rightarrow 1$) ablation behavior. The fitted absorption coefficients using the Hibst equation are much smaller compared to the water absorption coefficients stated in **Table 7**. The Hibst fits are plotted against **A**: the radiant exposure and **B**: the radiant exposure normalized to the ablation thresholds H_{th} .

Based on the fit parameter γ of the Hibst fits, we used the blow-off model in **Equation 13** and the steady-state model in **Equation 14** to fit the same experimental data in **Figure 24**. The blow-off model fits the data for the Tm:fiber laser ($R^2 = 0.992$) well, but the steady-state model fits the data poorly for the CO₂ laser ($R^2 = 0.1947$) and the CO laser ($R^2 = 0.6006$). This shows that γ cannot serve as a predictor of the ablation behavior, as γ is 0.756 for the

Tm:fiber ablation curve, whereas γ is 0.03 and 0.129 for the CO₂ laser and the CO laser ablation curve, respectively. According to the steady-state model, the etch depth increases linearly with radiant exposure. In our experimental data, a linear fit of the etch depth can only be obtained for lower energies, as non-linear effects (e.g. plume shielding, limitation by Rayleigh range, tissue shrinkage) at higher energies might occur leading to a loss in etch depth. This means that the CO₂ laser and the CO laser ablation curve cannot be described by the steady-state model.

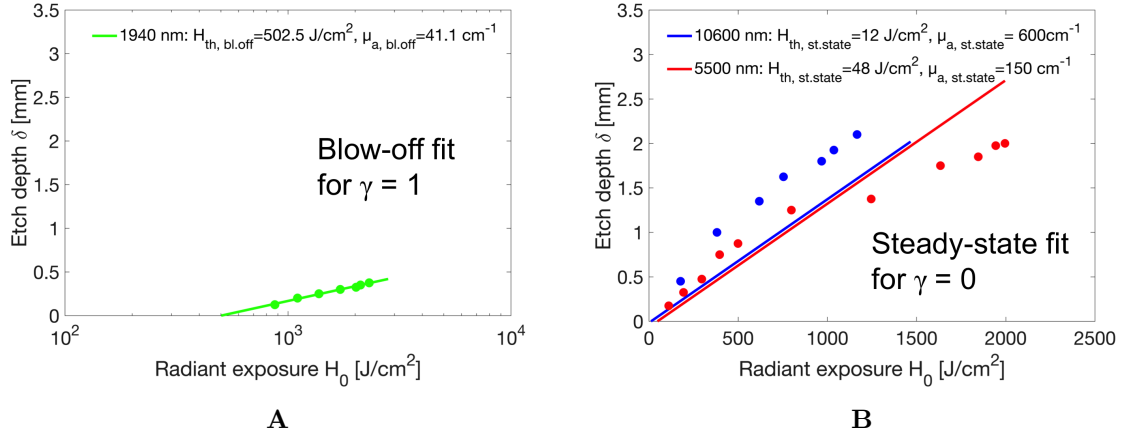


Figure 24. Based on the Hibst fit parameter γ from **Figure 23**, blow-off and steady-state fits of the etch depth δ_{abl} vs. radiant exposure H_0 were applied. The ablation threshold H_{th} and the absorption coefficient μ_a were determined. **A:** The blow-off model using **Equation 13** was fitted to the Tm:fiber laser data. **B:** The steady-state model using **Equation 14** cannot be fitted to the CO₂ laser and CO laser data.

Table 7. Absorption Coefficient μ_a and Ablation Threshold H_{th} in Different Ablation Models.

λ [nm]	Water Model		Hibst Model Fit		
	$70\% \times \mu_a$ [cm ⁻¹]	H_{th} [J/cm ²]	μ_a [cm ⁻¹]	H_{th} [J/cm ²]	$\gamma \in [0; 1]$
10600	630	4	188.6	15.3	0.030
5500	193.2	12.9	72	49.2	0.129
1940	79.8	31.3	49.1	467.5	0.756
λ [nm]	Steady-State Model Fit ($\gamma \rightarrow 0$)		Blow-Off Model Fit ($\gamma \rightarrow 1$)		
	μ_a [cm ⁻¹]	H_{th} [J/cm ²]	μ_a [cm ⁻¹]	H_{th} [J/cm ²]	
10600	600	12	—	—	
5500	150	48	—	—	
1940	—	—	41.1	502.5	

λ : wavelength, μ_a : absorption coefficient, H_{th} : ablation threshold
Hibst fit: $\gamma \rightarrow 0$ indicates steady-state, $\gamma \rightarrow 1$ indicates blow-off

The absorption coefficients and ablation thresholds calculated from the Hibst fits, steady-

state fits, and blow-off fit are compared to the water absorption coefficients in **Table 7**. It is noticeable the absorption coefficients are smaller and the ablation thresholds are higher than expected in the water ablation model. The higher ablation threshold can be a result of the higher tensile strength of skin.

4.3 Thermal Damage Zones

We quantified the lateral thermal damage \bar{x}_e at the ablation crater edges located at 50% etch depth and the residual thermal damage \bar{x}_b at the bottom layer of the ablation crater dependent on pulse energy and absorption coefficient. Inversely related to the etch depth, the thermal damage zone decreases with higher absorption coefficients. It is noticeable that the thermal damage zone at the bottom and at the edges of the ablation crater is similar in thickness. The results are also listed in **Table 5 and 6**.

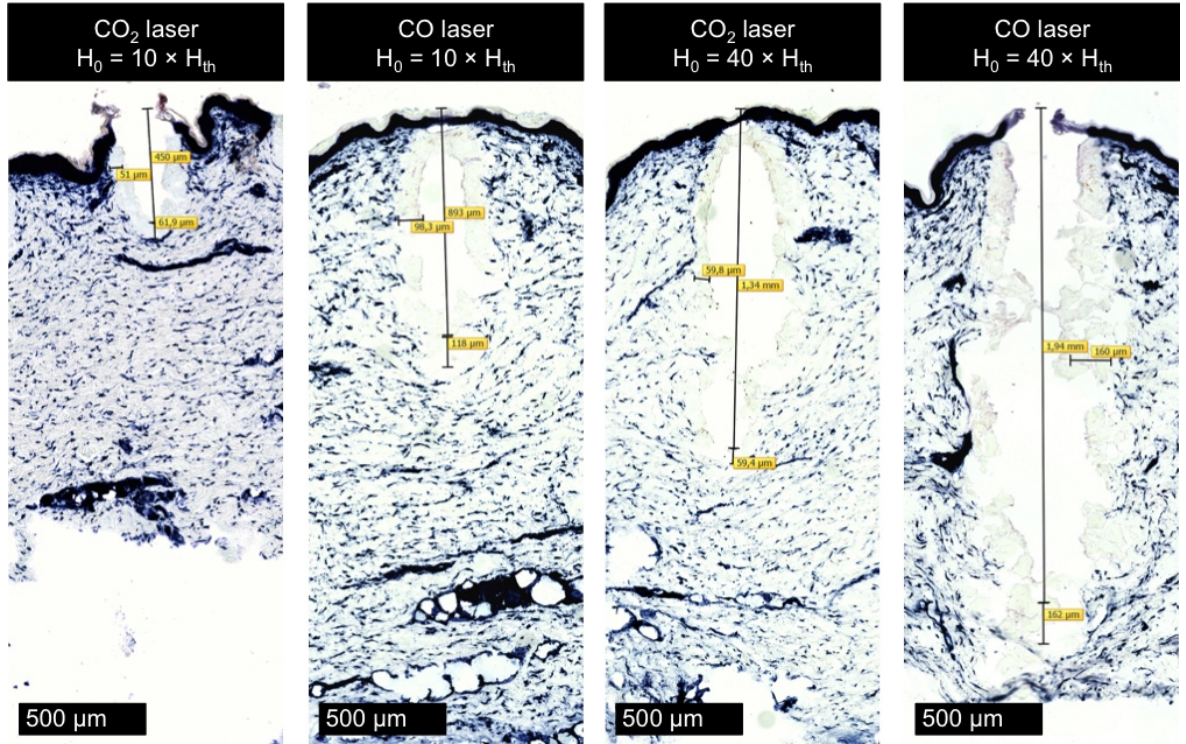


Figure 25. Laser-tissue effects produced by 2 ms pulses, 113-120 μm spot sizes, and at n -fold of the ablation threshold. The etch depth δ_{abl} and the thermal damage zones of the ablation crater bottom \bar{x}_b and edges \bar{x}_e were measured. At $10 \times H_{th}$, the modified CO₂ laser was adjusted at a radiant exposure of 177 J/cm² ($\delta_{abl} = 0.45$ mm, $\bar{x}_b = 0.05$ mm, $\bar{x}_e = 0.04$ mm) and compared to the CO laser at 499 J/cm² ($\delta_{abl} = 0.88$ mm, $\bar{x}_b = 0.12$ mm, $\bar{x}_e = 0.10$ mm). At $40 \times H_{th}$, the modified CO₂ laser was adjusted at 619 J/cm² ($\delta_{abl} = 1.35$ mm, $\bar{x}_b = 0.06$ mm, $\bar{x}_e = 0.06$ mm) and compared to the CO laser at 1945 J/cm² ($\delta_{abl} = 1.98$ mm, $\bar{x}_b = 0.16$ mm, $\bar{x}_e = 0.16$ mm).

The increase of radiant exposure to a factor 10 or 40 of the ablation threshold is exemplarily shown in **Figure 25** for the modified CO₂ laser system and the CO laser. In this comparison,

the CO laser generated higher ablation depths with larger coagulation zones than the modified CO₂ laser system. The thermal damage zones as a function of radiant exposure normalized to the ablation thresholds H_{th} are plotted in **Figure 26.A-B**.

4.4 Ablation-to-Coagulation-Ratio (ACR)

The ACR was calculated according to **Equation 16** that represents the amount of ablation in relation to the thermal damage zone at the bottom layer of the ablation crater. The ACR is maximized for the deepest ablation channel with the least degree of thermal damage as shown for the modified CO₂ laser system. **Figure 26.C** exhibits that the ACR increases with higher absorption coefficients. But the ACR decreases with very high radiant exposures, as a further increase of radiant exposure results in extended thermal damage zones without significantly changing the ablation crater in depth.

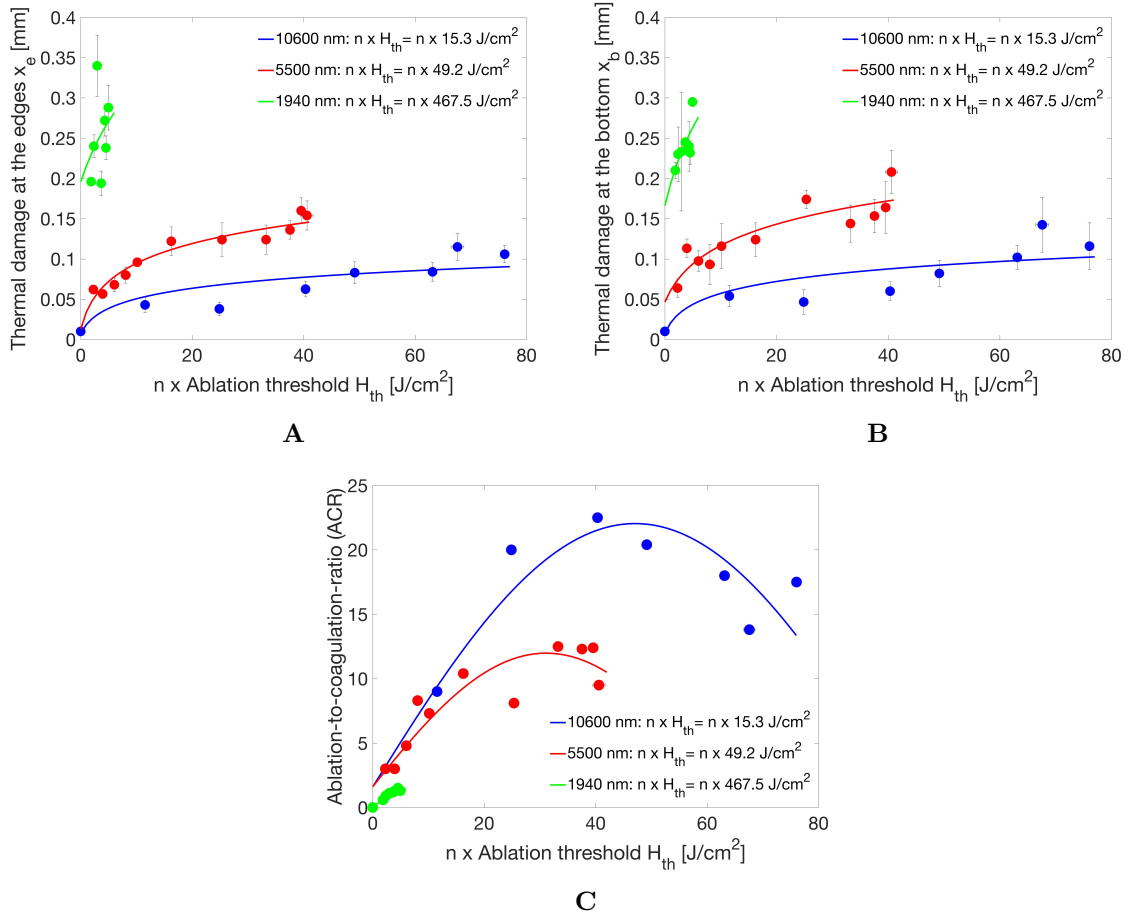


Figure 26. Thermal damage of the ablation craters plotted against the multiple n of the ablation threshold H_{th} for the modified CO₂ laser system, the CO laser, and the Tm:fiber laser. **A:** Thermal damage at the crater edges \bar{x}_e at 50% of the etch depth δ_{abl} . **B:** Thermal damage at the bottom of the crater \bar{x}_b . **C:** Ablation-to-coagulation-ratio ($\text{ACR} = \delta_{abl}/\bar{x}_b$). Higher radiant exposures will not significantly change the ablation depth, but instead the thermal injury will increase.

4.5 Small Spot CO Laser Ablation

In the last experiment, the crater dimensions of a 54 μm spot size was compared to a 113 μm spot size CO laser beam using a pulse energy of 80 mJ and a pulse length of 2. Halving the spot size would increase the radiant exposure by a factor of 4. Thus, reducing the spot size has increased the radiant exposure from 798 J/cm^2 to 3495 J/cm^2 .

The histology in **Figure 27** shows that the ablation crater width will be smaller when using the reduced spot size. As the ablation channel can be squeezed during the histological processing, the crater width is not accurately measured in vertical sections. Interestingly, the thermal damage zones that surround the ablation crater are comparable for both spot sizes.

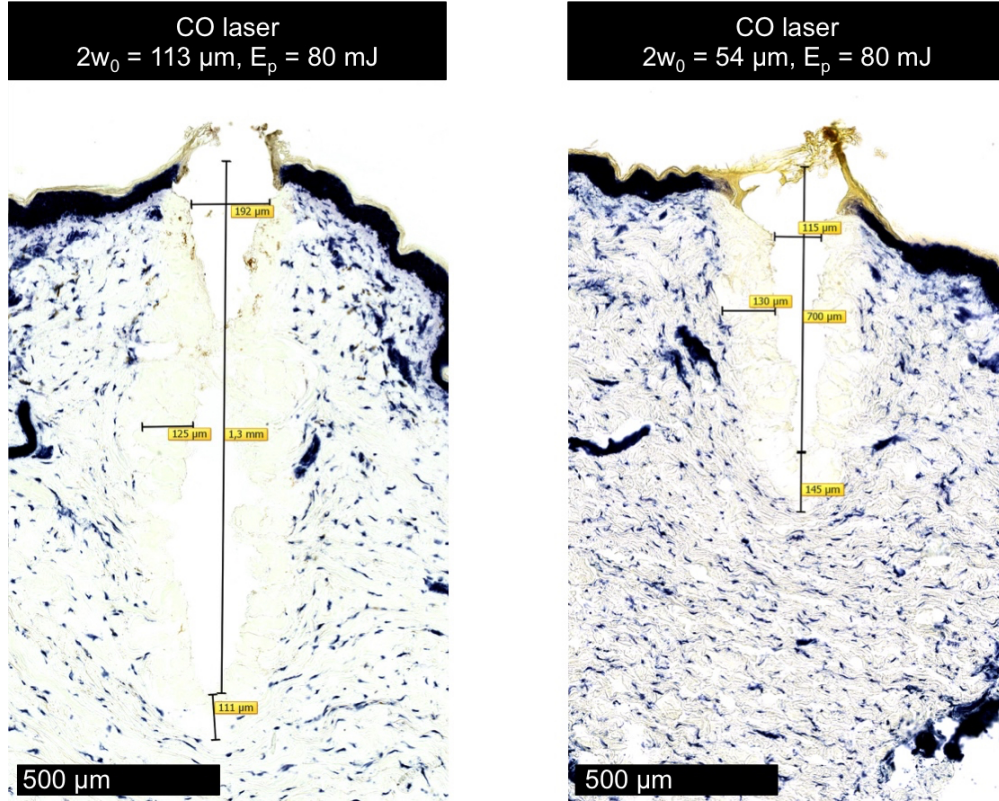


Figure 27. CO laser ablation using a pulse energy of 80 mJ and a pulse length of 2 ms with different spot sizes. The etch depth δ_{abl} , the thermal damage zones of the ablation crater bottom \bar{x}_b and edges \bar{x}_e , and the crater width D were measured. A 113 μm spot size CO laser beam at a radiant exposure of 798 J/cm^2 ($D = 192 \mu\text{m}$, $\delta_{abl} = 1.3 \text{ mm}$, $\bar{x}_e = 125 \mu\text{m}$, $\bar{x}_b = 111 \mu\text{m}$) was compared to a 54 μm spot size CO laser beam at 3495 J/cm^2 ($D = 115 \mu\text{m}$, $\delta_{abl} = 700 \mu\text{m}$, $\bar{x}_e = 130 \mu\text{m}$, $\bar{x}_b = 145 \mu\text{m}$).

Additionally, we observed that switching off the nitrogen gas purge results in a 10% decrease of pulse energy delivered to the tissue. However, alterations in morphology of the ablation crater were not observed, as a distortion of the beam spatial profile was anticipated based on thermal camera imaging (**Figure 13**).

4.6 Numerical Study of Heat Transfer and Phase Change in Skin

4.6.1 Laser-Tissue Ablation Model

The laser-induced temperature distribution in a skin model was studied using the finite element method (FEM) solver in COMSOL. Parts of the mesh cannot be removed so that the ablation of tissue was simulated by the change of phase, where material properties altered depending on temperature as described in **Section 3.6.5**. The input parameters of the simulation were adjusted to the exposure parameters used in the experiments. The heat transfer and phase change in tissue were simulated for 2 ms laser irradiation in 0.01 ms time steps. **Figure 28** illustrates the temperature distribution of the three-dimensional model at the end of the laser pulse. The results of the laser-tissue ablation simulation were compared with the histology.

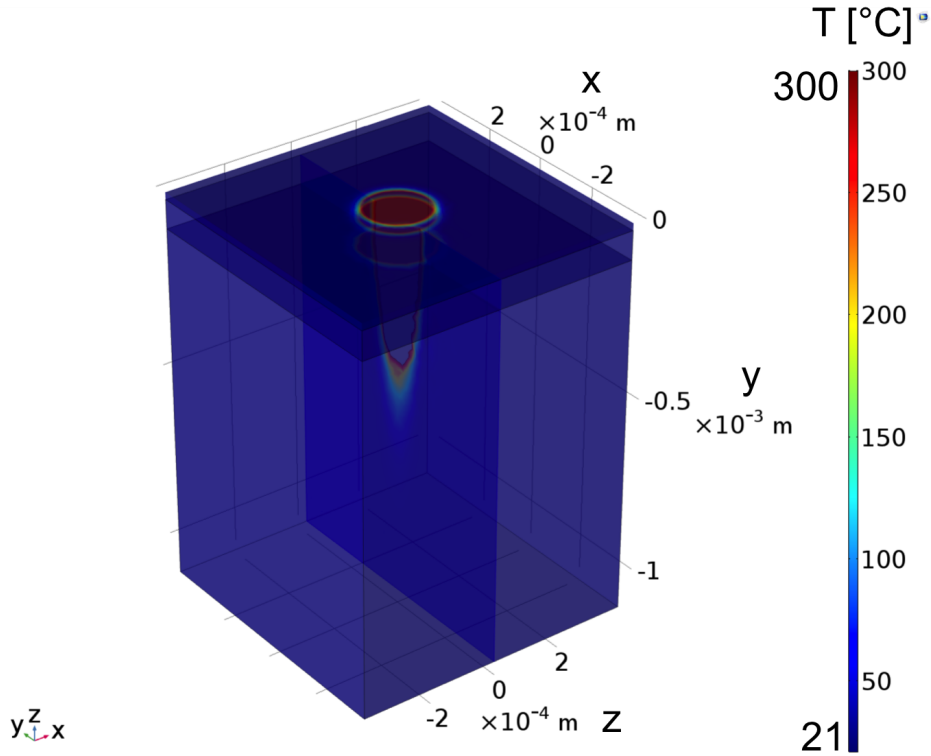


Figure 28. The temperature distribution resulting from a 2 ms laser pulse was simulated at 5500 nm wavelength using COMSOL (COMSOL Multiphysics, Stockholm, Sweden). The laser irradiance was 40 times the ablation threshold.

4.6.2 Temperature and Phase Change

The removal of tissue was assumed for $T \geq 300^{\circ}\text{C}$ and the zones of thermal denaturation was predicted for $65^{\circ}\text{C} \leq T < 300^{\circ}\text{C}$ as a result of laser heating. In this model, the Arrhenius formulation was neglected because coagulation is both temperature- and time-dependent.

Thermal denaturation can occur at temperatures below 65°C for longer exposure times as described by the Arrhenius equation. The tissue ablation is controlled by the phase θ , which is initialized to 1 before $T < 300^{\circ}\text{C}$ and to 0 after $T > 300^{\circ}\text{C}$ as shown in **Figure 29.A-B**. Consequently, material properties that depend on the phase will change simultaneously. This phase change was computed using **Equation 19-22**.

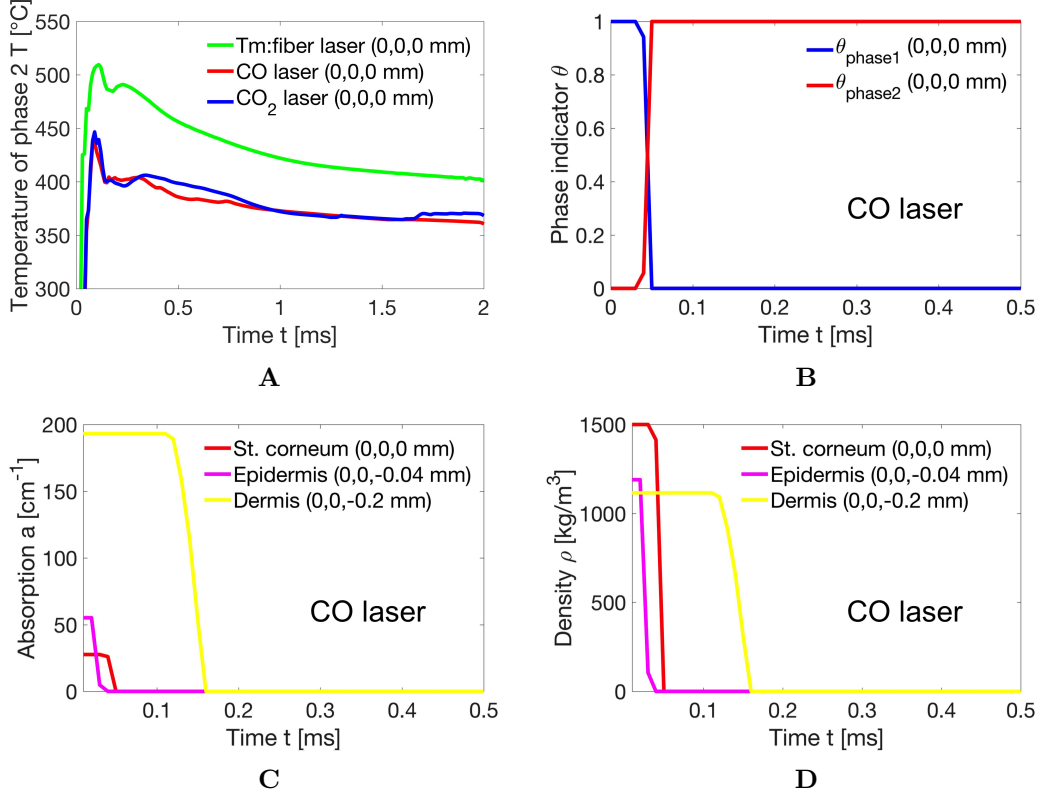


Figure 29. The temperature increase leads to a phase change, which is indicated by the parameter θ . The material properties of the skin layers will change according to the phase indicator in COMSOL (COMSOL Multiphysics, Stockholm, Sweden). The wavelength was modeled using different absorption coefficients a . The laser intensity I_0 was about 40 times the ablation threshold and the pulse length was 2 ms. 3D cut points (x, y, z) were chosen for the time-dependent evaluation. **A:** Temperature change in the center (0, 0, 0 mm). **B:** The phase transition in (0, 0, 0 mm) was achieved at 300°C . The phase indicates the transition. For the simulated CO laser ablation, the transition of **C:** the absorption coefficient and **D:** the density of the domains are shown.

In **Figure 29.C-D**, the material properties of the different skin layers are shown. Once the phase transition is achieved, the local absorption coefficient will be transformed to 0 cm^{-1} to simulate material removal. Also, the density of the skin layers will be set to 10^{-9} kg/m^3 . Ideally, the thermal conductivity k of phase 2 defined in **Table 3** should be smaller than 0.1 W/(mK) , however, we experienced computation problems for smaller values.

We defined 3D cut points (x, y, z) to evaluate the local temperature change and to check the material properties after phase transition. Although the specific heat capacity of phase 2 was set to 10^9 J/(kgK) and the absorption of phase 2 was set to 0 cm^{-1} to avoid a further

temperature increase after phase change, we unexpectedly evaluated a surface temperature increase of up to 450-500°C in the center of irradiation of phase 2 that decreases to 350-400°C (**Figure 29.A**). As material still exists in this model after phase transition, phase 2 undergoes a further temperature rise. The heat cannot be entirely removed from the tissue. This reveals the limitation of this ablation simulation.

4.6.3 Simulation of Ablation and Coagulation Zones

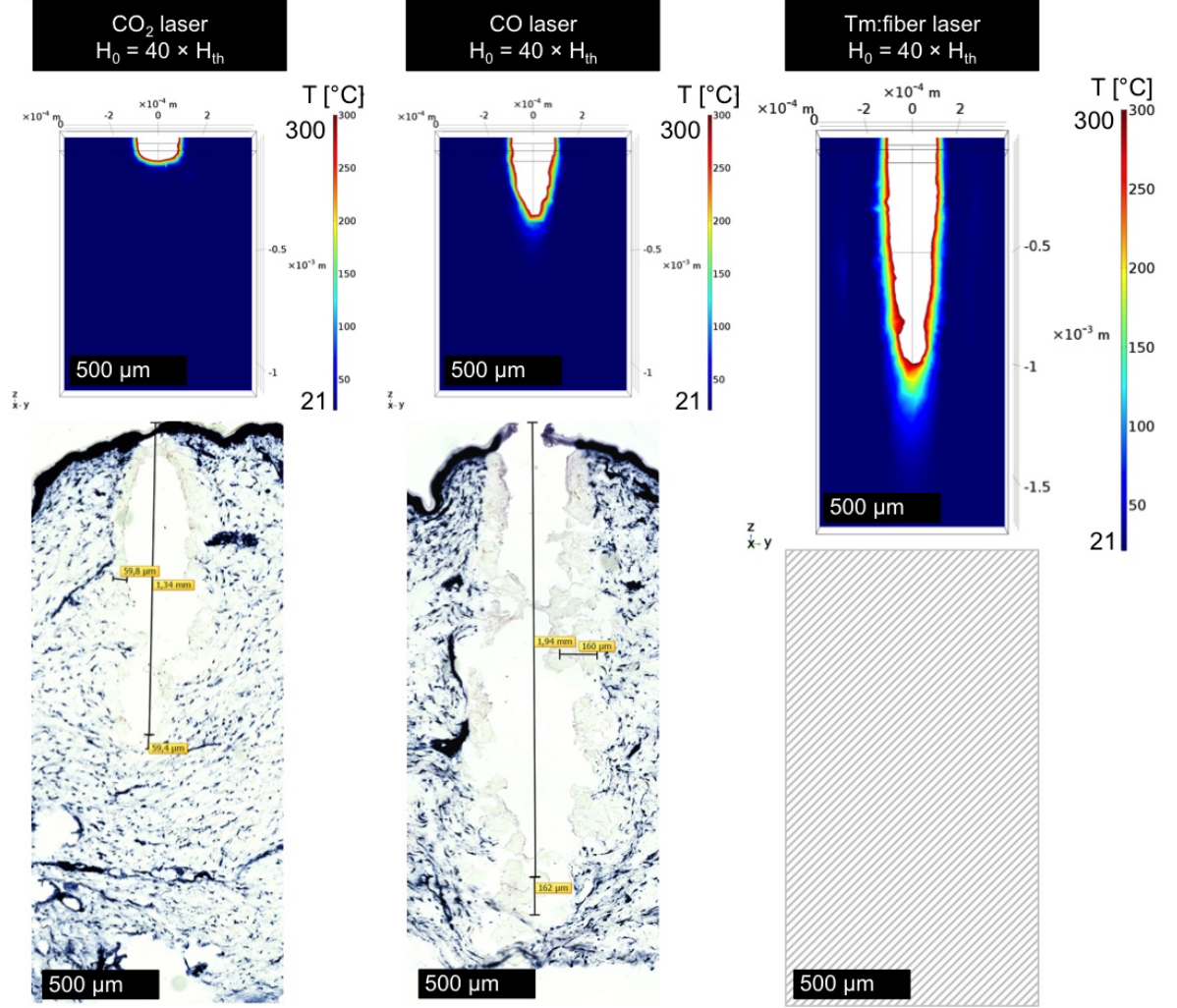


Figure 30. The laser-induced skin ablation was simulated using COMSOL (COMSOL Multiphysics, Stockholm, Sweden) for temperatures above 300°C and coagulation for temperatures between 65°C and 300°C neglecting the Arrhenius formulation. The numerical results are compared to the histology. No histology could be obtained at 40-times the ablation threshold of the Tm:fiber laser due to higher ablation threshold and limitation in output power

We used y, z -slices in **Figure 30** to illustrate the ablation depth and the coagulation zones. The thermal damage zone was calculated for temperatures between 65°C and 300°C. The ablation depth Z_{abl} predicted in the simulation was compared to the histological findings. The predicted thermal damage zones at the walls X_e and at the bottom of the ablation

crater X_b were compared to the histology results. In the simulation the thermal damage zone at the bottom of the ablation crater was larger than at the crater edges, whereas in the histology an isotropic formation of the thermal damage was observed. The simulation results are summarized in **Table 8**.

The predicted ablation depth and thermal damage zones in the simulation were in better agreement with the histological findings when using only 5% of the water absorption coefficients. This states that the numerical simulation cannot realistically predict the ablation depth and thermal damage zones.

Table 8. Ablation Depth and Thermal Damage in Numerical Study and Histology.

Input Parameters			Numerical Results		
λ [nm]	τ_p [ms]	$H_0 = 40 \times H_{th}$ [J/cm ²]	Z_{abl} [mm]	X_e [mm]	X_b [mm]
10600	2	619	0.102	0.027	0.027
5500	2	1.945×10^3	0.330	0.046	0.077
1940	2	18.7×10^3	0.993	0.064	0.281
Exposure Parameters			Histology Results		
λ [nm]	τ_p [ms]	$H_0 = 40 \times H_{th}$ [J/cm ²]	δ_{abl} [mm]	\bar{x}_e [mm]	\bar{x}_b [mm]
10600	2	619	1.35	0.06	0.06
5500	2	1.945×10^3	1.98	0.16	0.16
1940	—	—	—	—	—

Exposure parameters: λ : wavelength, τ_p : pulse length, H_0 : radiant exposure, H_{th} : ablation threshold

Numerical results: Z_{abl} : etch depth, X_e : thermal damage at the wall and X_b : at the bottom

Histology results: δ_{abl} : etch depth, \bar{x}_e : mean thermal damage at the wall and \bar{x}_b : at the bottom

5 Discussion

5.1 Laser-Tissue Ablation Experiments

The ratio of ablation to coagulation is typically related to the wavelength-dependent water absorption coefficient in skin tissue [10]. It has been postulated that clinical skin rejuvenation results and but also adverse effects will increase with depth and extent of thermal damage [42, 40]. There has been many approaches to customize the amount of thermal damage while maintaining a deep dermal ablation. For example, the operation of a dual-wavelength laser system that combines an ablative laser and a non-ablative laser [17] or a single-wavelength laser system that generates a high-energy short pulse for pure ablation that is immediately followed by a low-energy long pulse [52]. Both methods aim to deliver additional thermal damage to the skin. However, beam alignment of two different laser wavelengths is technically demanding. Also, plume shielding and misalignment due to tissue shrinkage must be taken into account in the delivery of multiple pulses. Laser pulse stacking could also significantly increase the risk of thermal necrosis [13]. Thus, it is of interest to achieve the desired amount of ablation and thermal damage by the use of one single pulse and one single wavelength.

5.1.1 Exposure Parameters

In these initial experiments, we compared the ablation and coagulation capabilities of different laser systems using similar exposure parameters. The ablation outcome is not only dictated by the absorption coefficient that is defined by the wavelength, but also other beam parameters, such as radiant exposure, pulse length, pulse shape, and focal spot size, need to be considered. The temporal pulse shape of the different lasers were not identical in this study. In contrast to the flat pulse structure of the Tm:fiber laser, the CO₂ lasers, and the CO laser exhibited microoscillation structures, which will be discussed in the following.

External pulse width modulation of the clinical CO₂ laser system have made the modified CO₂ laser system and the CO laser more similar in their temporal pulse structures (**Figure 12**). The oscillation frequency was still 2 MHz with 220 ns FWHM-micropulses for the CO₂ laser systems and 6.5 MHz with 90 ns FWHM-micropulses for the CO laser. Based on the high repetition rates of the micropulses, we anticipated single CO₂ laser and CO laser macropulses of 2 ms formed by the micropulses allowing a comparison of the different laser systems. Thus, no pulse stacking of the micropulses and no blow-off ablation effects were assumed.

In principle, micropulses in the range of nanoseconds can lead to the generation and propagation of thermoelastic stresses that facilitate the tissue ablation. Stress confinement is defined for pulse durations smaller than the stress confinement time $\tau_s = \delta/c_a$ [54], where $c_a = 1540$ m/s [46] is the longitudinal speed of sound in tissue and δ is the optical penetration depth. The FWHM-micropulses of the CO₂ laser and the CO laser were longer than the calculated

stress confinement times, which are 10.3 ns for the CO₂ laser and 33.6 ns for the CO laser, respectively. Therefore, spallation effects were neglected.

In clinical practice, the CO₂ laser treatment of photodamaged facial skin has a typical pulse energy of 15-22.5 mJ and an exposure time of 110-150 μ s [41]. In our ex vivo experiments, the long exposure time of 2 ms was chosen to ensure tissue ablation at all wavelengths as the Tm:fiber laser has the highest ablation threshold due to its low absorbing wavelength. At 1940 nm wavelength, the absorption coefficient of the Tm:fiber laser is 2.4-times lower than the 5500 nm CO laser and 7.9-times lower than the 10600 nm CO₂ laser, respectively (**Table 5**). However, a pulse duration of 2 ms is longer than the thermal relaxation time of 1.8 ms calculated for the CO₂ laser. Thus, a better approach would have been the comparison of the different lasers with the use of a pulse duration n -times shorter than the thermal relaxation time.

The modified CO₂ laser system was compared to the clinical CO₂ laser system using pulse energies ranging from i.a. 43 mJ to 109 mJ. The clinical CO₂ laser system was operated with 290-960 μ s pulse duration, which was shorter than the thermal relaxation time (**Table 6**). The pulse width modulation achieved a more constant power level over the pulse duration of 2 ms while maintaining the same microoscillations as the clinical laser system. The ablation generated by the modified CO₂ laser system were 25-33% smaller in depth but no extension of the thermal damage zones was observed. Interestingly, the thermal damage zone was not effected by the pulse width modulation, which generates lower average and peak powers by a factor of 2-6.9 and longer pulse durations of 2 ms.

Grad and Mozina have shown that the laser pulse shape has a significant effect on material removal [19]. The micropulses of the CO₂ lasers and the CO laser can contribute to higher peak powers that produce superior ablation results for laser drilling than the flat-shaped pulse of the Tm:fiber laser at lower power level. In **Figure 22**, we compared the different lasers using 2 ms pulses at 109-126 mJ and 184-195 mJ pulse energy, respectively. At a pulse energy of 109-125 mJ, the modified CO₂ laser system exhibits a 137.5 W peak power that is 2.5-times higher than its 55 W average power, while the CO laser has a 86 W peak power that is 1.4-times higher than its 60 W average power. At a pulse energy of 184-195 mJ, the clinical CO₂ laser system exhibits a 237.5 W peak power that is 2.5-times higher than its 95 W average power, while the CO laser has a 133 W peak power that is 1.3-times higher than its 100 W average power. In contrast, the Tm:fiber laser produces a rectangle-shaped pulse structure with a constant power level at 60 W and 100 W, respectively, with no microoscillations. Deeper ablation depths could be yielded by modulating the temporal and spatial pulse structures of the CO laser and Tm:fiber laser in terms of higher peak powers, longer pulse durations, and smaller focal spot sizes.

5.1.2 Ablation Depth

With the use of the same radiant exposures, the ablation depth increases with higher absorption coefficient because the threshold of ablation decreases [14, 29]. The optical absorption coefficients and the experimentally determined ablation thresholds of CO₂ laser, CO laser, and Tm:fiber laser are summarized in **Table 7**. Thus, the CO₂ lasers with the highest absorption coefficient in dermal tissue (630 cm^{-1}) demonstrated the deepest ablation craters in comparison to the CO laser (193.2 cm^{-1}) and the Tm:fiber laser (79.8 cm^{-1}) in our experimental settings. The superior ablation of the CO₂ lasers was achieved by high-energy pulses at low ablation threshold (15.3 J/cm^2). In contrast, the superficial ablation of the Tm:fiber laser was a result of high ablation threshold (467.5 J/cm^2) and pulse energies that were not sufficiently high enough for efficient ablation. In general, by using the same radiant exposure one compares "high ablation effects" at large absorption coefficients with "low ablation effects" at small absorption coefficients, which is a sort of misleading comparison. Therefore, taking a better approach the generated ablation depths were compared at the same multiple of the ablation threshold of each laser. If the radiant exposure is normalized to the ablation threshold, the CO laser with 3.3-times lower absorbing wavelength and 3.2-times higher ablation threshold (49.2 J/cm^2) has as expected demonstrated higher ablation depths than the CO₂ laser (**Figure 23.B**). For example, the CO laser produced an etch depth that was $630\text{ }\mu\text{m}$ (46.7%) deeper than the modified CO₂ laser system when increasing the radiant exposure by a factor 40 of the ablation threshold. As soon as the threshold of ablation is sufficiently overcome at very high radiant exposures, a higher optical penetration depth is correlated with higher ablation depth. However, a higher extent of thermal damage zone is also caused by non-absorbed energy that converts into heat due to lower absorption. The generation of thermal damage can be considered as "good" or "bad" depending on the indication of the treatment. Obviously, in vivo studies are required to state which amount of thermal damage is beneficial or harmful in consideration of wound healing and clinical goals.

The relationship between ablation depth and increasing radiant exposure is not linear. The ablation curve of the Tm:fiber laser shows a logarithmic dependence of etch depth on radiant exposure that can be described by the blow-off model (**Section 2.3.5**). The increase of radiant exposure leads to a saturation of the ablation curve for the CO₂ laser and the CO laser, which cannot be linearly fitted according to the steady-state model. Similar findings were observed by Evers et al. [10]. The Rayleigh range could be one of the limiting factors, as the beam diverges with higher penetration meaning that the energy density will decrease with depth. The Rayleigh range of the focused laser beams are 0.82 mm for the CO₂ laser, 1.34 mm for the CO laser, and 3.37 mm for the Tm:fiber laser. Also, other non-linear and shielding effects by the ejected material are shown to attenuate the incident laser light as implemented by the Hibst model. The ablation models are discussed in **Section 5.1.4**.

5.1.3 Residual Thermal Damage

The application of 2 ms pulses with a pulse energy of 184-195 mJ produced a thermal damage zone at the bottom of the ablation channel that has a thickness larger than the optical penetration depth by a factor of 7.5 for the CO₂ laser, 4.1 for the CO laser, and 1.8 for the Tm:fiber laser. This increasingly larger thermal damage zone for higher absorption coefficients can be explained by the thermal confinement condition [55], as Tm:fiber laser pulses were much shorter than the thermal relaxation time in contrast to CO₂ laser and CO laser pulses. The pulse duration of the modified CO₂ laser system was longer than the thermal diffusion time causing additional heating of the surrounding tissue. The least amount of thermal injury was observed for the CO₂ lasers and the most pronounced thermal damage was generated by the Tm:fiber laser. This can be explained by the strong water absorption at 10600 nm wavelength and the low water absorption at 1940 nm wavelength. The thermal damage zone generally increases with higher optical penetration depth for the same radiant exposures and for radiant exposures normalized to the ablation threshold (**Figure 26.A-B**). At radiant exposures higher than the ablation threshold by a factor 10 and 40, respectively, the CO laser exhibited 2.4-times and 2.7-times, respectively, larger coagulation zones at the bottom than the modified CO₂ laser system (**Figure 25**). The greater thermal damage zone of the CO laser is a result of the 3.3-times lower absorption at this wavelength.

It is interesting that the external pulse width modulation (involved the increase of pulse duration and the decrease of average and peak power) has not effected the thermal damage zone of the clinical CO₂ laser system but merely reduced the ablation depth, as mentioned in **Section 5.1.1**. The thermal relaxation time calculated for the Tm:fiber laser is 109.4 ms, which would allow a lengthening of the 2 ms laser pulse without significantly extending the thermal damage zones. Thus, the temporal pulse shape of the Tm:fiber laser could be modified with respect to longer exposure times or higher peak powers in combination with smaller focal spot sizes to obtain higher ablation depths.

Surprisingly, we observed that the thermal damage zone at the bottom and at the walls of the ablation channel were quite similar in thickness based on histology (**Figure 26.A-B**). The numerical simulation of the laser-tissue interaction predicted 67% larger residual thermal damage zones at the bottom in comparison to the edges of the ablation crater for the CO laser (**Figure 30**). We neglected the Arrhenius formulation in the simulation, but actually the walls of the ablation crater are longer exposed to the incident laser light than the bottom-layer. This can explain the additional thermal damage at the walls observed in the histology. Further, the formation of thermal damage zone at the walls was explained by the leaving hot steam that transmitted heat into the crater walls [57, 10].

5.1.4 Basic Ablation Models

The pulse duration of 2 ms is longer than the thermal relaxation time of the CO₂ laser (1.8 ms) and shorter than the thermal relaxation time of the CO laser (18.7 ms) and the Tm:fiber laser (109.4 ms). Thus, it was assumed that the fit parameter γ of the Hibst modification could provide a rough estimate of the ablation behavior with regard to the steady-state model and the blow-off model. The blow-off model assumes that tissue ablation occurs after the end of the laser pulse [55]. Indicated by the parameter $\gamma = 0.756$, the blow-off model was used to describe the ablation curve of the Tm:fiber laser (**Figure 24.A**). The steady-state model assumes that tissue ablation starts at the beginning of the laser pulse and continues during the entire exposure time [55]. However, the steady-state model cannot be applied to describe the ablation of the modified CO₂ laser ($\gamma = 0.03$) and the CO laser ($\gamma = 0.129$). The increase of etch depth with radiant exposure was not linear and might be limited by Rayleigh range, plume shielding, tissue shrinkage, and other non-linear effects (**Figure 24.B**). The fit results have shown that the parameter γ of the Hibst fit is not reliable in the prediction of the ablation behavior for $\gamma \neq 1 \neq 0$. Also, the fitted absorption coefficients determined from the Hibst fit were unrealistically smaller than the optical absorption coefficients of 70% water. The fitted absorption coefficient was 3.3-times smaller for CO₂ laser, 2.7-times smaller for CO laser, and 1.6-times smaller for Tm:fiber laser ablation stating that the Hibst model is inapplicable for our experimental data.

The experimental ablation threshold in skin was 3.8-times higher for CO₂ laser and CO laser and 15-times higher for Tm:fiber laser in comparison to the ablation of 70% water. The higher ultimate tensile strength of skin is one of the main reasons for higher ablation thresholds as the rigid collagen network requires higher radiant exposures. The skin is not a homogeneous material like water but rather consists of different skin layers such as stratum corneum (1998 MPa), epidermis (102 MPa), and dermis (10.2 MPa) with higher material stiffness [63].

5.1.5 ACR

The ablation-to-coagulation-ratio (ACR) could be a relevant parameter to adjust the amount of thermal damage zone in some clinical applications, where more thermal damage is advantageous. A large ACR would describe deep ablation with bleeding (less coagulation) as observed with the CO₂ laser. A small ACR could describe superficial ablation with no signs of bleeding (more coagulation) as anticipated for the Tm:fiber laser. However, the ACR is only useful in combination with the absolute values of etch depth and coagulation zone thickness.

In contrast to the deep ablations provided by the CO₂ lasers and the CO laser, the Tm:fiber exhibited ablation and coagulation in almost the same extent as indicated by a maximum ACR of 1.5. In this experimental setup, the Tm:fiber laser cannot be applied for deep dermal ablation, as the maximum etch depth was 380 μm at full power and at 2 ms pulse duration. Higher radiant exposures are required for higher ablation depths due to the high

ablation threshold of the Tm:fiber laser. Consequently, pulse duration or laser power need to be increased. Further, the focal spot size can be reduced to limit severe thermal damage formation.

Although the CO laser has demonstrated 46.7% deeper ablation craters at radiant exposures of 40-times the ablation threshold, the ACR of 12.4 was smaller due to the 2.7-times larger coagulation zones when compared to the modified CO₂ laser system with the ACR of 22.5. The ACR decreases with high radiant exposures of about 40-times above the ablation threshold, as the ablation depth will reach a maximum while the thermal damage will further increase with radiant exposure (**Figure 26.C**).

5.1.6 The Effect of Spot Size

We adjusted spot sizes comparable to the 120 μm scanning handpiece of the clinical CO₂ laser system. But a tighter focusing of the CO laser beam is easily possible and would achieve higher energy densities as halving the spot size would increase the radiant exposure by a factor of 4. Brandi et al. demonstrated the effect of spot size in laser drilling, where the ablation efficiency can be increased up to 10 fold when the spot size is decreased from 220 μm to 9 μm [8]. Spot sizes smaller than 120 μm could also be beneficial for the wound healing because the wound area is smaller. In the last experiment, we used a 54 μm spot size for CO laser ablation. However, we experienced that halving the spot size has reduced the Rayleigh range from 1.34 mm to 190 μm and has increased the M^2 from 1.35 to 2.2 [47]. Most likely the laser beam was spherically aberrated by the use of two lenses with a smaller diameter of 12.7 mm each in order to achieve a shorter total focal length of about 10 mm. But comparable spot sizes produced by the CO₂ laser would even result in a shorter Rayleigh range (**Equation 4**). The spot size is inversely proportional to the divergence of the laser beam. This means that a small focused laser beam will diverge rapidly as it propagates away from the focal plane into the tissue. Regardless of the higher energy density, the shorter Rayleigh range of the CO laser beam limited the penetration to 54% of the ablation depth (**Figure 27**). In order to maintain the high beam quality we have to improve the lens design. For example, microscope objective lenses would offer lower degrees of aberrations. Here, it is important to find the appropriate optical material that provides high transmission at 5500 nm wavelength.

5.2 Numerical Simulation of Laser-Tissue Ablation

A simple laser-tissue ablation model was developed using COMSOL Multiphysics to predict the ablation depth and the thermal damage formation following CO₂ laser, CO laser, and Tm:fiber laser irradiation. The simulation results were compared to the histological findings.

5.2.1 Two-Phase Model

Thermal effects were simulated dependent on the local temperature change of the tissue model as described in **Section 2.3.3** [59, 53]. Neglecting the Arrhenius effect, protein denaturation was expected for $300^{\circ}\text{C} \geq T \geq 65^{\circ}\text{C}$. In a simplification, tissue ablation was predicted for $T \geq 300^{\circ}\text{C}$. Radice et al. have used a variable specific heat capacity, which becomes significantly larger with temperature to account for the effect of energy removal by exhausted gas [39]. We simulated the laser-tissue ablation based on heat transfer and phase change meaning that changes of material properties explicitly depend on the phase. A two-phase model was applied to represent tissue in phase 1 and ablated tissue in phase 2. The absorption was set to 0 cm^{-1} and the heat capacity was set to $10^9\text{ J}/(\text{kgK})$ to simulate removed tissue in phase 2, which is clearly a mathematical approach. Surprisingly, there was an unexpected increase of the temperature of phase 2 up to $450\text{-}500^{\circ}\text{C}$ after phase transition (**Figure 29.A**), which cannot be explained by heat emission caused from underlying skin layers of phase 1. The heat removal caused by material ejection could not be realistically simulated as no material was physically removed or deformed in this model. Also, many theoretical assumptions on material properties and conditions for ablation have been made (**Section 3.6**) so that a realistic laser-tissue ablation model could not be developed with this simple approach.

5.2.2 Ablation Depth and Thermal Damage

Our simulation of the laser ablation of tissue based on heat transfer with phase change is a very simplified approach of the true ablation process. This ablation model has several weaknesses in terms of predicting the ablation depth and the thermal damage zones that will be discussed in the following:

1. We used a static tissue geometry and a two-phase concept as discussed in **Section 5.2.1**. The location of the tissue surface exposed to the laser irradiation does not change during the laser pulse. The predicted ablation depths were smaller by a factor of 6-13 in comparison with the histological findings. Hence, the results of the numerical simulation failed to reproduce the experimental results. A better approach could be the use of the moving mesh module or the deformed geometry module of COMSOL to achieve more realistic ablation depths [26].
2. The rapid volume expansion of emerging gas with subsequent tissue disruption was not simulated. This can be a further reason of the significant underestimation of the ablation depth, as ablation occurs when the increase of vapor pressure finally exceeds the ultimate tensile strength of the tissue [51].
3. We used a rectangle-shaped temporal pulse structure. In comparison to the other physical simplifications, this is certainly a tolerable assumption. Non-linear effects were intentionally neglected to get the idea of ablation as a thermally driven process. The effect of micropulsing

was discussed in **Section 5.1.1** stating that the microoscillations of the CO₂ lasers and the CO laser would allow more efficient ablation enhancing the ablation depth.

4. The Arrhenius formulation was neglected in the prediction of the thermal damage zones. The predicted thermal damage zone at the edges was smaller than at the bottom of the ablation crater. In contrast, the histology shows a homogeneous distribution of the thermal damage surrounding the ablation crater, which can be caused by the longer exposure of the walls to laser irradiation during the pulse. Evers et al. has suggested that hot gas formation could contribute to additional thermal damage at the walls [10]. The predicted thermal damage zones at the walls and at the bottom, respectively, were smaller by a factor of 2-3 and 2, respectively, in comparison with the histological findings.

This numerical simulation of the ablation process requires unrealistic low absorption (about 5% of the optical absorption coefficients) as input parameters to generate ablation depths more comparable to the histological results. Thus, this simplified model is not yet applicable in the prediction of ablation depths and thermal damage zones.

6 Conclusion

A variety of laser systems for skin rejuvenation and other dermatological indications is already available on the market. With the objective of extending the current treatment options, we intended to evaluate the feasibility of a novel CO laser and a Tm:fiber laser for fractional ablation of skin concluded from its profile of ablation to thermal damage. The results were compared to an ablative fractional CO₂ laser system considered as the gold standard.

6.1 Tm:Fiber Laser Ablation

The Tm:fiber laser is typically known as a non-ablative laser [30] due to the high ablation threshold at this low absorbing wavelength of 1940 nm. We observed very superficial ablation of the dermis by the Tm:fiber laser, which corresponded to about 12-14% of the etch depth generated by the CO₂ lasers using similar exposure parameters. More experiments using longer pulses, smaller spot sizes, and modulated temporal pulse structures are required to achieve higher ablation depths.

6.2 CO Laser Ablation

In this experimental setup, we have shown that the novel CO laser can generate ablation craters comparable to the CO₂ laser with extended thermal damage zones. The CO laser exhibited 46.7% higher etch depths with 2.7-times larger coagulation zones at radiant exposures 40-times the ablation threshold in comparison to the modified CO₂ laser system. The CO laser used in these experiments was an engineering prototype so that the gas purge tube system and the external liquid cooling made the handling more inconvenient when compared to the clinical CO₂ laser system. We also observed that switching off the nitrogen gas purge would result in a 10% decrease of the pulse energy but did not result in a distortion of the ablation crater as initially anticipated.

We experienced that halving the spot size of the CO laser beam resulted in a limitation of optical penetration due to shorter Rayleigh range. Therefore, the focusing lens system needs to be improved with special regard to long working distance and high beam quality. Further experiments should also involve shortening of the pulse duration, modification of the temporal pulse profile, and development of a laser scanning device. In a further step, in vivo studies using the CO laser are required to show whether additional thermal damage can lead to enhanced skin tightening without increasing adverse effects. In contrast to the rigid articulated mirror arms of the CO₂ laser, the delivery of CO laser light in flexible optical waveguides has been anticipated [1], which is not yet technically attainable.

6.3 Simulation Study

We developed a simple laser-tissue ablation model to analyze the effects of absorption coefficient on the tissue removal and thermal damage formation. The predicted ablation depths were underestimated by a factor 6-13 and the predicted thermal damage zones were underestimated by a factor 2-3. More realistic results were achieved for simulations using about 5% of the water absorption coefficients stating that this model is not applicable to predict the ablation outcome. The laser-tissue ablation was simulated as a thermally driven process using heat transfer and phase change. In order to develop a reliable model, further phenomena such as material ejection, expansion of emerging gas, tissue disruption, tissue shrinkage, shielding effects, etc. need to be implemented. Following studies could also incorporate irregular geometries of the skin such as epidermal ridges and dermal papillae. This simulation study has shown that the laser-tissue interaction is a complex process that cannot be easily simplified.

7 Appendix



Title: **Explant human tissue in-vitro study**

Sponsor Name: **SUNDRY**

PI Name: **Manstein, Dieter** Protocol #: **2017P000027**

Type: **Current View**

Date Received: **January 05, 2017**

Study Staff

Name	Role	Degree	Organization	Citi Certified
Evers, Michael	Co-Investigator		MGH > Dermatology > Dermatology - CBRC	February 28, 2017
Kositratna, Garuna	Co-Investigator	MD	MGH > Dermatology	April 15, 2016
Manstein, Dieter	Principal Investigator	MD, Ph.D	MGH > Dermatology > Dermatology - CBRC	October 14, 2018

Non Study Staff

Name	Degree	Organization
Heesakker, Tammy	MBA	MGH > Dermatology > Dermatology - CBRC

Funding source

Record #	Fund	Project Period	PI Name	Sponsor	Record Type	Process	Link Date	Link Status
2005A006863	218997	07/01/05-12/31/20	Manstein, Dieter	SUNDRY	RM – Research IR Sundry		03/14/17	Approved

Signatures

PI Name: Manstein, Dieter, MD, Ph.D

Authenticated: January 05, 2017

Initial Review

Title:
Explant human tissue in-vitro study

The Partners Human Research Committee has created several forms for review of human subjects research. This questionnaire includes a series of questions to identify the form (s) you need to complete for your research project.

1. Intervention/Interaction
2. Health / Medical Information

Version: V1.0 created on 03/14/17 - 11:50 AM
Downloaded date: 02/25/19 - 03:40 PM

Electronic IRB Submission Generated On February 25, 2019
Page 1 Of 12



- 3. Excess Human Material and Related Health / Medical Information
 - 4. Secondary Use of Research Samples and/or Data (samples/data from another research study)
 - 5. Research Data Repository (collecting and storing health/medical information for future research)
 - 6. Tissue or Sample Repository
 - 7. Coordinating Center / Core Labs
 - 8. Emergency / Single Patient Use of Investigational Products
-

1. Intervention and/or Interaction

Does your research involve an **intervention** and/or **interaction** with subjects for the collection of specimens or biological material or data (including health or clinical data, surveys, focus groups or observation or behavior)?

NOTE: Do not answer YES if this protocol is to establish a Research Data Repository or Sample/Tissue Repository. There are separate forms for Data and Tissue Repositories.

☐ Yes ☒ No

2. Health / Medical Information

Is your research limited to the use of health / medical information?

☐ Yes ☒ No

3. Excess Human Material and Related Health / Medical Information

Is your research limited to the use of excess (leftover) specimens/samples (and related health information) collected for clinical care?

☐ Yes ☐ No

Sponsor Funding: SUNDRY

Select the source of funding that will be used to support the proposed research:

☐ Government / Foundation / Other Non-Profit



- ☐ Corporate
- ☐ Institutional Award
- ☒ Department Funds
- ☐ None

Enter department name:
Dermatology - CBRC 16CA-MGH

Enter Peoplesoft fund # (if known):
218997

Is there a research fund, gift or sundry account supporting this study?

- ☒ Yes
- ☐ No

Insight Agreement proposal number (read-only field):
2005A006863

Enter Principal Investigator name (if different):
Manstein, Dieter MD,Ph.D

Medicare Coverage Analysis Requirement

Does the protocol for this study involve any items or services that will be billed to Medicare/private insurance, including study-specific procedures or those considered usual and customary care ("standard of care") outside the trial context?

- ☐ Yes
- ☒ No

NOTE: If you are unsure how to answer this question, please contact [Sarah Bednar](#) at Partners Clinical Trials Office at 617-954-9364, or for NWH investigators, please contact [Javita Sen](#) at 617-243-6517 for more information.

Is this the primary source of funding?

- ☒ Yes ☐ No ☐ Not applicable

Will the funding cover all subject study-related drugs, devices, procedures, tests, and visits?

- ☐ Yes ☐ No ☒ Not applicable (no subject study-related costs)

Sponsor Funding: None

Select the source of funding that will be used to support the proposed research:

- ☐ Government / Foundation / Other Non-Profit
☐ Corporate
☐ Institutional Award
☐ Department Funds
☒ None

Is this the primary source of funding?

- ☐ Yes ☐ No ☒ Not applicable

Excess Human Material

1. Purpose

Briefly describe the purpose of the research:

-Test the effects of thermal manipulation (.e.g. laser exposures, heating, cooling etc.) for various human tissues

-Test novel imaging techniques to assess specific physical, chemical and morphological properties of tissue

-Use tissue to harvest cells for cell and/or tissue culturing for the purposes as mentioned before

Data resulting from this research will be used for the following.

Check all that apply.

- ☒ Publication
- ☒ Oral Presentation
- ☒ Other

Explain:
potentially data generated from protocol will be used for filing of patents

Will data resulting from this research ever be submitted to the FDA?

- ☐ Yes ☒ No
-

2. Study Population

Describe the study population, e.g., age, gender, diagnosis.
the tissue does not require any specific study population

3. Description of Human Material / Planned Use

Describe the human material requested and it's planned use.
in-vitro testing of human tissue and cells as described in purpose section

4. Fetal Tissue

Will **fetal tissue** be collected for this study?

- ☐ Yes ☒ No
-

5. Source of Human Material

From where will you obtain the human material?

Check all that apply.

- ☐ BWH
- ☐ Faulkner
- ☒ MGH
 - ☐ Blood Bank
 - ☐ Clinical Laboratories
 - ☐ Labor / Delivery
 - ☒ Operating Room
 - ☒ Pathology
- ☐ McLean
- ☐ NWH
- ☐ NSMC
- ☐ PCHI
- ☐ SRH
- ☐ Broad Institute
- ☐ Network Sites

NOTE: Approval to obtain materials from the areas listed above must be obtained from the relevant Department. Investigators are responsible for contacting them prior to

initiating the research.

☒ Commercial Supplier of Biological Materials

Specify:

NDRI

Matrix Biologics

☐ Collaborators at outside institutions who provide excess clinical samples

☐ Other

Was the material or will the material be obtained from patients as part of their clinical care, e.g., a clinically indicated blood test, biopsy, or surgical procedure?

☐ Yes ☒ No

Will any of the investigators / research staff perform the procedure that provides the excess tissue?

☐ Yes ☒ No

7. Data to be Requested From the Following Time Period

Indicate the time period over which the materials / tissue were / will be obtained as part of clinical care.

From (mm/yyyy):

1/2017

To (mm/yyyy):

For future material / tissue, use anticipated project end date.

12/2020



NOTE: This information is needed for the PHRC to determine whether the research use of the human material / tissue meets the criteria for an exemption from the requirements for IRB review. For more information about HUMAN SUBJECTS RESEARCH or EXEMPT RESEARCH, see the following [OHRP website](#).

Will you record information about the samples without identifiers or codes?

☐ Yes ☒ No

8. Recording of Related Health / Medical Information

Do you plan to record health / medical information in order to correlate tissue analysis findings with clinical findings?

☐ Yes ☒ No

Have you defined data variables to be collected / obtained?

☐ Yes ☒ No

Enter data variables and move to the box on the right.

tissue imaging

Enter data variables and move to the box on the right.

tissue metabolism

Enter data variables and move to the box on the right.

tissue viability

12. Informed Consent / Authorization / Waivers

Will informed consent and authorization be obtained from individuals for use of their human materials / tissue and/or health / medical information for the research?

☐ Yes ☒ No

Explain why the risk to subjects, specifically the risk to privacy, is no more than minimal risk.
discarded tissue without medical records

Explain why the research could not practicably be carried out without the waiver of consent / authorization.
discarded tissue without medical records

NOTE: "Only in a few research studies would it be impossible to obtain informed consent; however in many studies the financial cost would be prohibitive and a potentially poor use of limited research resources." *Ensuring Voluntary Informed Consent and Protecting Privacy and Confidentiality, National Bioethics Advisory Commission.*

Explain why the rights and welfare of the subjects will not be adversely affected by the waiver of consent / authorization.
discarded tissue without medical records, course of medical care in no way affected by research

NOTE: If the research uncovers information about the subjects that has important health / medical implications for them, contact the PHRC to discuss the appropriate process for providing subjects with additional pertinent information.

13. Sending Human Material / Tissue and Related Health / Medical Information to Collaborators Outside Partners

Will human material / tissue samples be sent to collaborators outside Partners?

☐ Yes ☒ No

Will any related health / medical information be sent to collaborators outside Partners?

☐ Yes ☒ No



Materials Transfer Agreements (Transferring Material To Research Collaborators)

1. Transfer of samples/data to academic or non-profit entities or collaborators, refer to [Partners Materials Transfer Checklist](#).

For Template Agreements between academic or non-profit entities or collaborators, see below:

[Template Agreement for Coded Samples](#)

[Template Agreement for Non-Identifiable Samples](#)

<http://csrl.bwh.harvard.edu>

2. Transfer of samples/data to for-profit or commercial entities or collaborators, contact contact [Partners Research Ventures & Licensing](#).

HIPAA and Tracking Disclosures Of Identifiable Health Information (PHI)

1. Disclosures of PHI to persons or entities outside Partners without the written authorization of the subject must be tracked in accordance with Partners policy:

[“Accounting of Disclosures”](#) (PHS Intranet link).

http://intranet.partners.org/finance/hipaa/privacy/1/1_PH130.doc

2. Tracking is NOT required for disclosure of LIMITED DATA SETS under a DATA USE AGREEMENT. For more information about LIMITED DATA SETS and DATA USE AGREEMENTS, refer to Partners policy [“Limited Data Sets Policy/Data Use Agreements.”](#)

NOTE: Partners (PHS) is the HIPAA covered entity. PHS includes BWH, Faulkner, MGH, McLean, PCHL, SRH, NSMC, and NWH, among others. PHS does not include other Harvard affiliated hospitals, such as BIDMC, DFCL, HSPH, CHB, or MEEL.

Clinical Trials Registration

Investigator-initiated clinical trials of drugs, biologics, or devices conducted by a Partners investigator must be registered on ClinicalTrials.gov to comply with the FDA Amendments Act (FDAAA). The following information is being collected to identify studies that require clinical trials registration and to inform Principal Investigators (PI) of their responsibilities for registration, and if applicable, results reporting. Information posted on ClinicalTrials.gov (CT.gov) must be updated and verified at least every 6 months to meet ClinicalTrials.gov requirements.



IMPORTANT NOTE: Even if your investigator-initiated clinical trial does not meet the FDAAA clinical trials registration requirements, you are strongly advised to read the [International Committee of Medical Journal Editors \(ICMJE\)](#) clinical trials registration requirements and consider registering your trial to comply with the ICMJE requirements for publication.

For additional information, please see:

- [Partners Clinical Trials Registration Information web page](#)

I. FDAAA Applicable Trial and Responsible Party

1. Is this a Partners investigator – initiated research study?

- ☒ Yes ☐ No

2. Does this research involve a **drug, biological product or device** that is:

- Being studied at one or more sites in the U.S.; or
- Manufactured in the U.S. (or its territories); or
- Being studied under an investigational new drug application (IND) or investigational device exemption (IDE)?

NOTE: FDA approved and investigational drugs, biologics and devices should be included.

- ☐ Yes ☒ No

This research does not meet FDAAA clinical trials registration requirements.

Attachments

Name	Mode
Commercial Vendor Certification (Other)	Electronic

MATRIX BIOLOGICAL, LLC

11654 Plaza America Drive #111 Reston, Virginia 20190-4700



March 09, 2017

Dear Ms Heesakker:

Matrix Biological, Inc. will be happy to provide your team with the requested material for your study upon approval of your project by the clinical site ethical committee. Our primary samples are collected under ethical committee reviewed and approved protocols by detailed oriented staff. Matrix Biological does not retain any intellectual rights pertaining to the samples we provide and used in your studies.

We look forward to helping you develop your innovative platform. Please keep us in mind for your project and let us know when you want to move forward.

SAMPLE CONSENT PROVISION

I understand and agree that:

- a. Tissue/specimens removed from me during surgery and not needed for my diagnosis (leftover tissue) may be provided to researchers and scientists for medical research and education, including the development of commercial products.
- b. I will not receive any compensation or share in any financial benefits for donating my specimens, even if any new commercial products, tests or discoveries are developed from the research done with my specimens.

REPRESENTATIONS OF HUMAN BIOLOGICAL MATERIALS PROVIDED BY MATRIX BIOLOGICAL, INC.

1.1. Matrix Biological, Inc. represents that the human biological materials ("Biospecimens") provided to Researcher shall have been obtained with the consent of the donor, or the donor's next-of-kin, for use in biomedical research and education and development of commercial products as may be required pursuant to all applicable local, state, and federal laws and regulations governing human tissue and human tissue services.

1.2. Matrix Biological, Inc. shall not provide to Researcher any identifiable private information or protected health information with respect to a donor of Biospecimens provided pursuant to this Agreement, unless such donor has provided authorization for the release of such information in compliance with all applicable local, state and federal laws and regulations, including the Health Insurance Portability and Accountability Act ("HIPAA")

Best Regards,

Grace Cuelez Droblas
Managing Director & Co Founder

8 References

- [1] AO Abakumov, VS Aleinikov, VG Artjushenko, VP Belyaev, LN Butvina, LK Bogush, VV Vojtsekhovsky, ND Devyatkov, EM Dianov, VG Dobkin, VI Masyshev, AM Prokhorov, and VK Sysoev. “Coagulation and destruction of biological tissue by CO laser irradiation using fibre-optic cable”. In: *Optics and Laser Technology* 18.4 (Aug. 1986), pp. 190–192.
- [2] VS Aleinikov, VP Belyaev, ND Devyatkov, VI Klimenko, LD Mamedli, VI Masyshev, and VK Sysoev. “Applications of a carbon monoxide laser in surgery”. In: *Soviet Journal of Quantum Electronics* 13.10 (1983).
- [3] IB Allemann and J Kaufman. “Basics in Dermatological Laser Applications”. In: ed. by IB Allemann and DJ Goldberg. Karger, 2011. Chap. Fractional Photothermolysis, p. 62.
- [4] RR Anderson and JA Parrish. “Selective photothermolysis: precise microsurgery by selective absorption of pulsed radiation”. In: *Science* 220.4596 (1983), pp. 524–527.
- [5] AO Barel, M Paye, and HI Maibach. “Handbook of Cosmetic Science and Technology”. In: 4th ed. CRC Press, 2014. Chap. Confocal Raman spectroscopy for in vivo skin hydration measurement, p. 120.
- [6] PR Bergstresser and MI Costner. “Dermatology”. In: ed. by JL Bolognia, JL Jorizzo, and P Ronald. Vol. 1st. Mosby, 2003. Chap. Anatomy and Physiology, pp. 25–26.
- [7] R Birngruber, F Hillenkamp, and VP Gabel. “Theoretical investigations of laser thermal retinal injury”. In: *Health Phys* 48.6 (June 1985), pp. 781–96.
- [8] F Brandi, N Burdet, R Carzino, and A Diaspro. “Very large spot size effect in nanosecond laser drilling efficiency of silicon”. In: *Opt Express* 18.22 (2010), pp. 23488–94.
- [9] AM Erlendsson, AG Doukas, WA Farinelli, B Bhayana, RR Anderson, and M Haedersdal. “Fractional laser-assisted drug delivery: Active filling of laser channels with pressure and vacuum alteration”. In: *Lasers Surg Med* 48.2 (Feb. 2016), pp. 116–24.
- [10] M Evers, L Ha, M Casper, D Welford, G Kositratna, R Birngruber, and D Manstein. “Assessment of skin lesions produced by focused, tunable, mid-infrared chalcogenide laser radiation.” In: *Lasers in Surgery and Medicine* (May 2018).
- [11] MA Farage, KW Miller, and HI Maibach. “Textbook of Aging Skin”. In: Springer, 2010. Chap. The Structural and Functional Development of Skin During the First Year of Life Using Non-invasive Methods, p. 716.
- [12] GJ Fisher, S Kang, J Varani, Z Bata-Csorgo, Y Wan, S Datta, and JJ Voorhees. “Mechanisms of photoaging and chronological skin aging”. In: *Arch Dermatol* 138.11 (2002), pp. 1462–1470.
- [13] RE Fitzpatrick, SR Smith, and S Sriprachya-Anunt. “Depth of vaporization and the effect of pulse stacking with a high-energy, pulsed carbon dioxide laser”. In: *J Am Acad Dermatol* 40.4 (1999), pp. 615–22.

- [14] M Frenz, H Pratisto, F Konz, ED Jansen, AJ Welch, and HP Weber. “Comparison of the effects of absorption coefficient and pulse duration of 2.12-/spl mu/m and 2.79-/spl mu/m radiation on laser ablation of tissue”. In: *IEEE Journal of Quantum Electronics* 32.12 (1996), pp. 2025–2036.
- [15] NM Fried and KE Murray. “High-Power Thulium Fiber Laser Ablation of Urinary Tissues at 1.94 mu m”. In: *Journal of Endourology* 19.1 (Feb. 2005), pp. 25–31.
- [16] M Ganguly, R O’Flaherty, A Sajjadi, and K Mitra. “Heat Transfer and Fluid Flow in Biological Processes”. In: ed. by S Becker and A Kuznetsov. 1st. Academic Press, 2015. Chap. Tissue Response to Short Pulse Laser Irradiation, pp. 43–58.
- [17] MP Goldman, N Marchell, and RE Fitzpatrick. “Laser skin resurfacing of the face with a combined CO₂/Er:YAG laser”. In: *Dermatol Surg* 26.2 (2000), pp. 102–104.
- [18] GJ Goodman. “Facial Rejuvenation: A Total Approach”. In: ed. by D Goldberg. Springer Science and Business Media, 2007. Chap. Lasers and Lights, pp. 1–48.
- [19] L Grad and J Mozina. “Laser Pulse Shape influence on Optically Induced Dynamic Processes”. In: *Appl Surf Sci* 127-129 (1998), pp. 999–1004.
- [20] A Haake, GA Scott, and KA Holbrook. “The Biology of the Skin”. In: ed. by RK Freinkel and DT Woodley. The Parthenon Publishing Group, 2001. Chap. Structure and function of the skin: overview of the epidermis and dermis, pp. 19–45.
- [21] *Heat Transfer Module User’s Guide*. Version 4.3b. COMSOL Multiphysics. May 2013.
- [22] A Held. “New CO laser technology offers processing benefits”. In: *Photonics Spectra* (2015), pp. 34–36.
- [23] J Ion. *Laser Processing of Engineering Materials: Principles, Procedure and Industrial Application*. Butterworth-Heinemann, 2005, pp. 64–66.
- [24] WM Irvine and JB Pollack. “Infrared optical properties of water and ice spheres”. In: *Icarus* 8.1-3 (1968), pp. 324–360.
- [25] ED Jansen, TG van Leeuwen, M Motamedi, C Borst, and AJ Welch. “Partial vaporization model for pulsed mid-infrared laser ablation of water”. In: *J Appl Phys* 78.564 (1995), pp. 564–571.
- [26] Y Kim, ES Choi, W Kwak, and Y Shin. “Analysis of the Thermal Distribution by Using Laser-Beam Irradiation”. In: *Journal of the Korean Physical Society* 51.2 (2007), pp. 503–508.
- [27] S Kondo. “The roles of cytokines in photoaging”. In: *Journal of Dermatological Science* 23.Suppl. 1 (2000), pp. 30–36.
- [28] IH Kwon, Y Bae, UC Yeo, YH Choi, and GH Park. “Histologic analyses on the response of the skin to 1,927-nm fractional thulium fiber laser treatment”. In: *Journal of Cosmetic and Laser Therapy* 20.1 (Feb. 2018), pp. 12–16.
- [29] GL LeCarpentier, M Motamedi, LP McMath, and AJ Welch. “The effect of wavelength on ablation mechanisms during CW laser irradiation: argon versus Nd:YAG (1.32 mu m)”. In: *IEEE Engineering in Medicine and Biology Society* 11th Annual International Conference (1989).

- [30] HM Lee, S Haw, JK Kim, SE Chang, and MW Lee. “Split-face study using a 1,927-nm thulium fiber fractional laser to treat photoaging and melasma in Asian skin”. In: *Dermatol Surg* 39.6 (June 2013), pp. 879–88.
- [31] TH Maiman. “Stimulated Optical Radiation in Ruby”. In: *Nature* 187.4736 (1960), pp. 493–494.
- [32] D Manstein, GS Herron, RK Sink, H Tanner, and RR Anderson. “Fractional photothermolysis: a new concept for cutaneous remodeling using microscopic patterns of thermal injury”. In: *Lasers in Surgery and Medicine* 34.5 (2004), pp. 426–438.
- [33] K Nouri. “Laser/Light Applications in Urology”. In: *Lasers in Dermatology and Medicine*. 2011, p. 567.
- [34] T Omi and K Numano. “The Role of the CO₂ Laser and Fractional CO₂ Laser in Dermatology”. In: *Laser Ther.* 23.1 (2014), pp. 49–60.
- [35] AE Ortiz, MP Goldman, and RE Fitzpatrick. “Ablative CO₂ lasers for skin tightening: traditional versus fractional”. In: *Dermatol Surg* 12 (2014), pp. 147–151.
- [36] CKN Patel and RJ Kerl. “Laser oscillation on X¹Σ⁺ vibrational-rotational transitions of CO”. In: *Applied Physics Letters* 5.81 (1964), pp. 81–83.
- [37] M Petrus and DC Dumitras. “Numerical Simulation and in Vitro Experimental Temperature Distribution Analysis in Irradiated Tissue”. In: *UPB Sci Bull, Series A* 74.4 (2012), pp. 167–176.
- [38] J Preissig, K Hamilton, and R Markus. “Current Laser Resurfacing Technologies: A Review that Delves Beneath the Surface”. In: *Semin Plast Surg* 26.3 (2012), pp. 109–116.
- [39] JJ Radice, PJ Joyce, AC Tresansky, and RJ Watkins. “A COMSOL Model of Damage Evolution Due to High Energy Laser Irradiation of Partially Absorptive Materials”. In: *Proceedings of the 2012 COMSOL Conference in Boston* (2012).
- [40] Z Rahman, H MacFalls, K Jiang, KF Chan, K Kelly, J Tournas, OF Stumpp, V Bedi, and C Zachary. “Fractional Deep Dermal Ablation Induces Tissue Tightening”. In: *Lasers in Surgery and Medicine* 41 (2009), pp. 78–86.
- [41] WM Ramsdell. “Fractional Carbon Dioxide Laser Resurfacing”. In: *Seminars in Plastic Surgery* 26.3 (2012), pp. 125–130.
- [42] R Saluja, J Khoury, SP Detwiler, and MP Goldman. “Histologic and clinical response to varying density settings with a fractionally scanned carbon dioxide laser”. In: *J Drugs Dermatol* 8.1 (2009), pp. 17–20.
- [43] K Sarbana, VK Garg, and S Bansal. “Lasers in Dermatological Practice”. In: ed. by K Sarbana and VK Garg. Jaypee Brothers Medical Publishers, 2014. Chap. Basics of Laser-Tissue Interactions, pp. 3–24.
- [44] AL Schawlow and CH Townes. “Infrared and Optical Masers”. In: *Physical Reviews* 122.6 (1958).
- [45] M Schulze. “CO laser introduction”. EPIC Conference. Nov. 2015.

- [46] HC Shin, R Prager, H Gomersall, N Kingsbury, G Treece, and A Gee. “Estimation of average speed of sound using deconvolution of medical ultrasound data”. In: *Ultrasound Med Biol* 36.4 (Apr. 2010), pp. 623–36.
- [47] AE Siegman. “High-power laser beams: defining, measuring and optimizing transverse beam quality”. In: *Proc SPIE 1810, 9th International Symposium on Gas Flow and Chemical Lasers* (1993).
- [48] AM Smith, MC Mancini, and N Shuming. “Bioimaging: Second window for in vivo imaging”. In: *Nature Nanotechnology* 4.11 (2009), pp. 710–711.
- [49] Y Suzuki and A Tachibana. “Measurement of the μm sized radius of Gaussian laser beam using the scanning knife-edge”. In: *Applied Optics* 14.12 (1975), pp. 2809–2810.
- [50] EH Taudorf, CS Haak, AM Erlendsson, PA Philipsen, RR Anderson, U Paasch, and M Haedersdal. “Fractional ablative erbium YAG laser: histological characterization of relationships between laser settings and micropore dimensions”. In: *Lasers Surg Med* 46.4 (Apr. 2014), pp. 281–9.
- [51] S Thomsen and JA Pearce. “Optical-Thermal Response of Laser-Irradiated Tissue”. In: ed. by AJ Welch and MJC van Gemert. 2nd. Springer Netherlands, 2011. Chap. Thermal Damage and Rate Processes in Biologic Tissues, pp. 487–549.
- [52] MA Trelles, S Mordon, V Benitez, and JL Levy. “Er:YAG laser resurfacing using combined ablation and coagulation modes.” In: *Dermatol Surg* 27.8 (Aug. 2001), pp. 727–34.
- [53] JW Valvano. “Optical-Thermal Response of Laser-Irradiated Tissue”. In: ed. by AJ Welch and MJC Gemert. 2nd. Springer Netherlands, 2011. Chap. Tissue Thermal Properties and Perfusion, pp. 455–485.
- [54] A Vogel and V Venugopalan. “Mechanisms of Pulsed Laser Ablation of Biological Tissues”. In: *Chem Rev* 103 (2003), pp. 577–644.
- [55] A Vogel and V Venugopalan. “Optical-Thermal Response of Laser-Irradiated Tissue”. In: ed. by AJ Welch and MJC van Gemert. 2nd. Springer Netherlands, 2011. Chap. Pulsed Laser Ablation of Soft Biological Tissues, pp. 551–615.
- [56] JT Walsh. “Optical-Thermal Response of Laser-Irradiated Tissue”. In: ed. by AJ Welch and MJC Gemert. 2nd. Springer Netherlands, 2011. Chap. Basic Interactions of Light with Tissue, pp. 13–26.
- [57] JT Walsh, TJ Flotte, and TF Deutsch. “Er:YAG Laser Ablation of Tissue: Effect of Pulse Duration and Tissue Type on Thermal Damage”. In: *Lasers in Surgery and Medicine* 9.4 (1989), pp. 314–326.
- [58] JT Walsh, TG van Leeuwen, ED Jansen, M Motamedi, and AJ Welch. “Optical-Thermal Response of Laser-Irradiated Tissue”. In: ed. by AJ Welch and MJC Gemert. 2nd. Springer Netherlands, 2011. Chap. Pulsed Laser Tissue Interaction, pp. 617–649.
- [59] AJ Welch and MJC van Gemert. “Optical-Thermal Response of Laser-Irradiated Tissue”. In: ed. by AJ Welch and MJC van Gemert. 2nd. Springer Netherlands, 2011. Chap. Overview of Optical and Thermal Laser-Tissue Interaction and Nomenclature, pp. 3–11.

- [60] AJ Welch, MJC van Gemert, and WM Star. “Optical-Thermal Response of Laser-Irradiated Tissue”. In: ed. by AJ Welch and MJC van Gemert. 2nd. Springer Netherlands, 2011. Chap. Definitions and Overview of Tissue Optics, pp. 27–64.
- [61] D Welford. “Ultrapulse modifications”. Feb. 2013.
- [62] DT Woodley and M Chen. “The Biology of the Skin”. In: ed. by RK Freinkel and DT Woodley. The Parthenon Publishing Group, 2001. Chap. The basement membrane zone, pp. 133–152.
- [63] F Xu and TJ Lu. *Introduction to Skin Biothermomechanics and Thermal Pain*. 2011, p. 223.
- [64] HD Young. *University Physics*. 7th. Addison Wesley, 1992.

9 Acknowledgements

I would like to express my gratitude to my advisor Prof. Reginald Birngruber for his untiring guidance and his continuous support from the beginning. I would like to thank for his enthusiasm, his patience, and his immense knowledge that helped me in developing this research work. Moreover, I value the long conversations about art and culture that were not related to science but were just as fascinating.

My sincere thanks goes to my advisor Prof. Dieter Manstein who inspired me and who encouraged me to become a physician after finishing my master's degree in science. I greatly admire his expertise in dermatology and in laser physics. His innovative power helped me to think outside the box. Without him this research project would not have been possible.

Besides my advisors, I would like to thank Dr. Martin Jaspan and Dr. David Welford from Endeavour Laser Technologies Inc. for their expertise, their feedback and their support in developing the experimental setup.

I credit Dr. Garuna Kositratna for her full commitment and for teaching me the tissue processing techniques.

I would like to thank Michael Evers, Malte Casper, and Dr. Reza Monazami for the continuous support in the lab and the great time in Boston besides work.

Many thanks go to Dr. Andrew Held and Dr. Matthias Schulze from Coherent Inc. for the collaboration work.

Furthermore, many thanks also go to Dr. Walfre Franco and Dr. Amir Sajjadi, they have been an inexhaustible source of information and expertise.

10 Curriculum Vitae

Man Linh Ha

Born: June 9, 1988 in Braunschweig, Germany



Education

- | | |
|---------------|--|
| 11/18 | Medical License (Approbation)
Schleswig-Holstein, Germany |
| 10/12 - 11/18 | School of Medicine (overall grade 1.8)
University of Luebeck |
| 10/10 - 09/12 | Master of Science in Medical Engineering (overall grade 1.3)
University of Luebeck |
| 10/07 - 08/10 | Bachelor of Science in Medical Engineering (overall grade 1.9)
University of Luebeck |

Research Experience

- | | |
|---------------|---|
| 08/15 - 04/17 | Doctoral Candidate , Cutaneous Biology Research Center, Department of Dermatology, MGH, Harvard Medical School, Charlestown, MA, USA. Advisors: Prof. Dr. R. Birngruber, Prof. Dr. D. Manstein |
| 11/11 - 09/12 | Research Scholar , Wellman Center for Photomedicine, Department of Dermatology, MGH, Harvard Medical School, Boston, MA, USA. Advisors: Prof. Dr. R. Birngruber, Prof. Dr. D. Manstein <ul style="list-style-type: none">• M.Sc. thesis: "Fractional Laser Ablation of Cutaneous Tissue Using a Tunable CW and Gain-Switched $\text{Cr}^{2+}:\text{ZnS}/\text{Se}$ IR Laser" (overall grade 1.0) |
| 11/09 - 08/10 | Clinical trial , Institute of Biomedical Optics, Medical Laser Center, Luebeck. Advisors: Prof. Dr. R. Birngruber, PD Dr. G. Huettmann <ul style="list-style-type: none">• B.Sc. thesis: "Multiphoton Tomography of Connective Tissue Remodeling After Fractional Laser Treatment" (overall grade 1.0) |

Clinical Training

since 03/19	Resident in Dermatology, Venereology, and Allergology UKSH Luebeck, Germany
07/18 - 09/18	Intern in Dermatology, Venereology, and Allergology (PJ) UKSH Luebeck, Germany
03/18 - 07/18	Intern in General and Trauma Surgery (PJ) DRK-Krankenhaus Moelln-Ratzeburg, Germany
11/17 - 03/18	Intern in Internal Medicine (PJ) Sana Kliniken Luebeck, Germany
09/16 - 10/16	Intern in Accident and Emergency (Famulatur) UKSH Luebeck, Germany
07/16 - 08/16	Intern in Dermatology, Venereology, and Allergology (Famulatur) UKSH Luebeck, Germany
03/16 - 03/16	Intern in Internal Medicine and Cardiology (Famulatur) Schoen Klinik, Neustadt, Germany
02/16 - 03/16	Intern in Geriatrics (Famulatur) Krankenhaus Rotes Kreuz, Luebeck, Germany
03/15 - 04/15	Intern in General, Thoracic, and Vascular Surgery (Famulatur) Zollernalb Klinikum, Albstadt, Germany
02/15 - 03/15	Intern in Oral and Maxillofacial Surgery (Famulatur) Staedtisches Klinikum, Braunschweig, Germany

Stipends and Awards

since 03/19	Clinician Scientist, Cluster of Excellence EXC2167 "Precision Medicine in Chronic Inflammation" (PMI) <ul style="list-style-type: none">• CD-4 "Advanced Optical in vivo Imaging in Patients"
08/15 - 10/15	Research stipend, Massachusetts General Hospital, Boston, MA, USA
03/12	Best speaker award, 1 st Annual Conference BioMedTec Wissenschafts-campus Luebeck, March, 2012
11/11 - 09/12	Research stipend, Massachusetts General Hospital, Boston, MA, USA
05/06 - 06/06	1 st prize, 13 th state competition of Jugend zeichnet und gestaltet e.V. Niedersachsen, Germany

11 Published Work

Parts of this dissertation cover research previously reported in:

1. Journal Articles

Ha L, Jaspan M, Welford D, Evers M, Kositratna G, Casper MJ, Manstein D, Birngruber R: "First assessment of a carbon monoxide laser and a thulium fiber laser for fractional ablation of skin." In: **Lasers in Surgery and Medicine**, January, 2020. doi: 10.1002/lsm.23215. [Epub ahead of print]

Evers M, **Ha L**, Casper M, Welford D, Kositratna G, Birngruber R, and Manstein C: "Assessment of skin lesions produced by focused, tunable, mid-infrared chalcogenide laser radiation". In: **Lasers in Surgery and Medicine**, September, 2018;50(9):961-972. doi: 10.1002/lsm.22935.

2. Abstracts and Proceedings

Ha L, Birngruber R, and Manstein D: "Fractional ablation of ex vivo human skin using a novel CO laser". In: **American Society for Laser Medicine and Surgery Abstracts**, no. 56, p. 20, 2017. Oral presentation at: **37th ASLMS Annual Conference on Energy-Based Medicine and Science**, San Diego Convention Center, San Diego, CA, USA, April, 2017.

Evers M, **Ha L**, Welford D, Birngruber R, and Manstein D: "Wavelength-dependence of fractional ablations in biological materials using a tunable Cr²⁺:ZnSe/S infrared laser". **American Society for Laser Medicine and Surgery Abstracts**, no. 46, pp. 38-39, 2014.

Ha L and Manstein D: "Development of a novel fractional laser device utilizing a tunable Cr²⁺:ZnSe infrared laser". In: **Annual Conference BioMedTec Wissenschaftscampus Luebeck Proceedings**, pp. 97-100, 2012. Poster and oral presentation at: **1st Annual Conference BioMedTec Wissenschaftscampus Luebeck**, Luebeck, Germany, March, 2012.

3. Oral Presentations

"Ablation of skin using a novel CO laser". Cutaneous Biology Research Center, Massachusetts General Hospital, Charlestown, MA, USA, October 13, 2015.

"Fractional ablation of skin using a tunable Cr²⁺:ZnSe/S laser". Wellman Center for Photomedicine, Massachusetts General Hospital, Boston, MA, USA, September, 2012.

Erklärung

Ich erkläre hiermit, dass ich die vorliegende Arbeit selbstständig ohne fremde Hilfe angefertigt und keine anderen als die in der Arbeit genannten personellen, technischen und sachlichen Hilfen oder Hilfsmittel benutzt habe. Die aus anderen Quellen direkt oder indirekt übernommenen Daten und Konzepte sind unter Angabe der Quelle gekennzeichnet.

Diese Arbeit wurde bisher weder im In- noch im Ausland in gleicher oder ähnlicher Form einer anderen Prüfungsbehörde vorgelegt.

Lübeck, den 06.03.2020

A handwritten signature in black ink, appearing to read 'Linha'.